

**DEVELOPMENT OF A BIOELECTRONIC NEURAL INTERFACE  
FOR ELECTROPHYSIOLOGICAL SENSING OF HUMAN CEREBRAL ORGANOID**

**THANDA DUANGRAT  
THANAPAT CHATMEEBOON  
SAHARAT CHAWARUECHAI  
APHIWISH APHISAKSIRI**

**A THESIS SUBMITTED IN PARTIAL FULFILLMENT  
OF THE REQUIREMENTS FOR  
THE DEGREE OF BACHELOR OF ENGINEERING  
(BIOMEDICAL ENGINEERING)  
DEPARTMENT OF BIOMEDICAL ENGINEERING  
FACULTY OF ENGINEERING  
MAHIDOL UNIVERSITY  
2024**

**COPYRIGHT OF MAHIDOL UNIVERSITY**

Biomedical Engineering Project  
Entitled  
**DEVELOPMENT OF A BIOELECTRONIC NEURAL INTERFACE  
FOR ELECTROPHYSIOLOGICAL SENSING OF HUMAN CEREBRAL ORGANOID**

.....

Miss Thanda Duangrat

.....  
Mr. Thanapat Chatmeeboon

.....  
Mr. Saharat Chawaruechai

.....  
Mr. Aphiwish Aphisaksiri

.....  
Assoc. Prof. Dr. Yodchanan Wongsawat  
Advisor

.....  
Assoc. Prof. Dr. Soonthorn Oraintara  
Advisor

Biomedical Engineering Project  
Entitled  
**DEVELOPMENT OF A BIOELECTRONIC NEURAL INTERFACE**  
**FOR ELECTROPHYSIOLOGICAL SENSING OF HUMAN CEREBRAL ORGANOID**  
was submitted to Faculty of Engineering, Mahidol University  
For the Degree of Bachelor of Engineering (Biomedical Engineering)  
On April 25, 2025

.....  
Miss Thanda Duangrat

.....  
Mr. Thanapat Chatmeeboon

.....  
Mr. Saharat Chawaruechai

.....  
Mr. Aphiwish Aphisaksiri

.....  
Assoc. Prof. Dr. Yodchanan Wongsawat  
Advisor

.....  
Assoc. Prof. Dr. Soonthorn Oraintara  
Advisor

## **ACKNOWLEDGEMENT**

We would like to express our sincere gratitude to the Faculty of Engineering, Mahidol University, and the Mahidol University Frontier Research Facility for providing the infrastructure and laboratory support essential to this study. We are especially thankful to Ramathibodi Hospital for supplying the stem cell line, and to Prof. Suradej Hongeng, M.D., Dip. ABP, Dr. Nithi Asavapanumas, M.D., and Dr. Nareerat Sutjarit for their invaluable support in stem cell and organoid culturing techniques. We also greatly appreciate the technical guidance and equipment access provided by the Brain-Computer Interface Laboratory. Lastly, we are grateful to our advisors and collaborators for their continued insights and encouragement, which were vital to the successful completion of this work.

Thanda Duangrat

Thanapat Chatmeeboon

Saharat Chawaruechai

Aphiwish Aphisaksiri

DEVELOPMENT OF A BIOELECTRONIC NEURAL INTERFACE  
FOR ELECTROPHYSIOLOGICAL SENSING OF HUMAN CEREBRAL ORGANOID

THANDA	DUANGRAT	6413376	EGEG/B
THANAPAT	CHATMEEBOON	6413381	EGEG/B
SAHARAT	CHAWARUECHAI	6413433	EGEG/B
APHIWISH	APHISAKSIRI	6413445	EGEG/B

B.ENG.(BIOMEDICAL ENGINEERING)

THESIS ADVISORY: YODCHANAN WONGSAWAT, Ph. D.  
SOONTORN ORAINTARA, Ph. D.

**ABSTRACT**

This report presents the development of a bioelectronic neural interface for electrophysiological monitoring of cerebral organoids derived from human induced pluripotent stem cells. To achieve this, a custom-designed microelectrode array was integrated with three-dimensional brain organoid cultures to enable non-invasive and real-time acquisition of spontaneous neural activity. The recorded signals were processed using the Microelectrode Array Network Analysis Pipeline for evaluation of microscale network dynamics, including spike timing, burst behavior, and functional connectivity. We found an emergence of organized microcircuits through network-level analysis, indicating functional maturation of the neuronal networks. In parallel, immunohistochemical analysis confirmed progressive stages of neurogenesis and synaptogenesis through increased expression of PAX6, MAP2, synaptophysin, and PSD95, validating the structural maturation of the organoids over time. Together, these findings demonstrate the potential of cerebral organoids as a biologically inspired platform for investigating brain-like computation and for informing the design of future neuromorphic computing systems.

KEY WORDS: Brain Organoid, Bioelectronics, Microelectrode Arrays System, Neural Circuits, Neuromorphic Computation, Brain Organoid-Computer Interface

110 pages

# Table of Contents

ACKNOWLEDGEMENT .....	i
ABSTRACT.....	ii
LIST OF FIGURES .....	vii
LIST OF TABLES .....	xi
ABBREVIATIONS AND ACRONYMS .....	xii
INTRODUCTION .....	1
1.1 Project Overview.....	1
1.2 Task Breakdown.....	2
PROBLEM STATEMENT .....	3
2.1 Problem Statement .....	3
2.2 Objectives and Expectations .....	4
DESIGN APPROACH.....	5
3.1 Design Specification .....	5
3.1.1 Ethical Consideration.....	5
3.1.2 Cerebral Organoid.....	5
3.1.3 Microelectrode Array System .....	5
3.1.4 Spiking Neural Networks Modeling Feasibility .....	5
3.2 Initial Design.....	6
CONCEPT SYNTHESIS .....	7
4.1 Prior Art.....	7
4.1.2 Electrophysiology as a Platform for Brain Mimicry .....	8
4.1.3 Brain Organoid as a Biological Processors .....	14
4.1.4 Neuromorphic Designs Inspired by Brain Organoid .....	15
4.2 Concept Generation.....	22
4.2.1 Brain Organoid Generation .....	22
4.2.1.1 hiPSCs Culturing Materials and Reagents .....	22

4.2.1.2 Cerebral Organoid Culturing Materials and Reagents .....	26
4.2.2 Microelectrode Arrays System.....	30
4.2.2.1 Microelectrode Arrays Printed Circuit Board .....	30
4.2.2.2 Interconnect board.....	31
4.2.2.3 BCI Lab's System in Package .....	32
4.2.2.4 RHS Stim/Recording System.....	34
4.2.3 Organoid Intelligence Platform.....	34
4.2.4.1 Training Process and Adaptive Learning Mechanisms .....	35
4.2.4.2 Integration into a Virtual Gameplay Environment.....	35
4.2.4 Neuromorphic Computation .....	36
4.2.4.1 Spike Sorting.....	36
4.2.4.2 Spatiotemporal Mapping.....	37
4.2.4.3 Spike Time Latency Distribution .....	37
4.2.4.4 Pairwise Spike Time Correlation Mapping.....	38
4.3 Concept Reduction .....	40
<b>ANALYSIS AND EVALUATION OF DESIGN PROCESS.....</b>	<b>41</b>
5.1 Brain Organoid Generation and Characterization.....	41
5.1.1 Human Induced Pluripotent Stem Cells Culture.....	41
5.1.2 Brain Organoid Culture.....	41
5.1.2.1     Organoid Formation (Day 0–5).....	42
5.1.2.2     Induction (Day 5–7).....	43
5.1.2.3     Expansion (Day 7–10) .....	43
5.1.2.4     Maturation (Day 10–40+) .....	44
5.1.3     Immunohistochemical Staining.....	45
5.2 Microelectrode Array System .....	52
5.2.1 Microelectrode Array PCB.....	53
5.2.2 BCI Lab's System in Package .....	56

5.2.2.1 Firmware of System in Package.....	57
5.2.2.2 System in Package Printed Circuit Board .....	62
5.2.3 Data Processing Application .....	65
5.2.3.1 Base Modules .....	65
5.2.3.2 Raw Data Receiver Module .....	66
5.2.3.3 Data Filtering Module.....	67
5.2.3.4 Recording Module.....	68
5.2.3.5 User Interface .....	68
5.2.3.6 Additional files.....	70
5.2.4 Experimental Setup for Electrophysiology Recording .....	74
5.2.5 Electrophysiological signal from brain organoid.....	75
5.2.6 Electrophysiological signal of brain organoid analysis .....	76
5.2.7 Improvement on Microelectrode Arrays system.....	78
5.3 MEA-NAP : Functional Connectivity Analysis Pipeline.....	80
5.3.1 Signal Preprocessing .....	80
5.3.2 Multi-Unit Spike Detection.....	83
5.3.3 Spike Feature Extraction .....	86
5.3.3.1 Basic Spike Features .....	86
5.3.3.2 Higher-Order Features: Network Burst Properties .....	86
5.3.4 Functional Connectivity Inference.....	87
5.3.5 Network Structure and Node Role Characterization.....	90
5.3.5.1 Graph-Theoretical Analysis of Functional Connectivity .....	90
5.3.5.2 Node Role Classification Using Node Cartography .....	94
5.3.6 Validation of the Pipeline with Real Experimental Data .....	97
5.3.7 Analysis of Functional Maturation and Network Reorganization in Brain Organoids Across Development and Neurostimulation .....	97

5.3.7.1 Developmental Differences in Neuronal Activity and Connectivity Between Day 35 and Day 42 Brain Organoids .....	97
5.3.7.2. Changes in Neuronal Activity and Network Connectivity in Day 42 Brain Organoids Following NMDA Stimulation.....	99
5.3.7.3 NMDA Stimulation Induces Distributed Functional Connectivity Across Brain Organoid Networks .....	100
5.3.7.4 Impact of Neurostimulation on Directional Connectivity and Node Cartography of in Brain Organoids .....	101
CONCLUSION .....	103
REFERENCES.....	104

## LIST OF FIGURES

Figure 1 Task Breakdown .....	2
Figure 2 Schematic Diagram of the Initial Design .....	6
Figure 3 Schematic diagram based on the Hodgkin-Huxley model, illustrating the biological representation of a neuronal cell membrane (left) and its equivalent electrical circuit (right) [12]. .....	8
Figure 4 A comparison of spiking neuron models based on computation resource and degree of biomimicry [13]. .....	10
Figure 5 The shape of LFP and spikes from brain organoid [19]. .....	11
Figure 6 SCTi004-A Donor Information (Left) and SCTi004-A (Right).....	22
Figure 7 mTeSRTM Plus.....	23
Figure 8 Y-27632.....	24
Figure 9 D-PBS .....	24
Figure 10 ReLeSRTM.....	25
Figure 11 DMEM/F-12 with 15 mM HEPES .....	25
Figure 12 CryoStor® CS10.....	26
Figure 13 STEMd'iffTM Cerebral Organoid Kit .....	26
Figure 14 Anti-Adherence Rinsing Solution.....	27
Figure 15 Organoid Embedding Sheet.....	27
Figure 16 6-Well Ultra-Low Adherent Plates .....	28
Figure 17 Gentle Cell Dissociation Reagent.....	28
Figure 18 Corning® Matrigel® hESC-Qualified Matrix.....	29
Figure 19 Flexible Micro electrode array PCB .....	31
Figure 20 Gold finger connecting pins .....	31
Figure 21 MEA grid pattern .....	31
Figure 22 Interconnect board top view .....	32
Figure 23 Hirose Connector .....	32
Figure 24 Omnetics connector .....	32
Figure 25 BCI Lab's System in Package .....	33
Figure 26 RHS stim/recording system .....	34
Figure 27 hiPSCs for Brain Organoid Culture .....	41
Figure 28 Dissociated hiPSCs under a hemocytometer .....	42
Figure 29 Embryoid Body.....	43

Figure 30 Brain Organoid Post-Induction.....	43
Figure 31 Organoids Embedded using Matrigel .....	44
Figure 32 Brain Organoid Post-Expansion .....	44
Figure 33 Day 18, 20, 25, 30, 35, 40, 42 Brain Organoid Respectively .....	45
Figure 34 Hydrophobic barrier surrounds tissue sections.....	46
Figure 35 Mounted IHC samples .....	47
Figure 36 DAPI (Top Left), PAX6 (Top right), MAP2 (Bottom left), and Merged (Bottom right) Immunostaining of Day 35 Brain Organoid.....	48
Figure 37 DAPI (Top Left), PSD95 (Top right), SYN (Bottom left), and Merged (Bottom right) Immunostaining of Day 35 Brain Organoid.....	49
Figure 38 DAPI (Top Left), PAX6 (Top right), MAP2 (Bottom left), and Merged (Bottom right) Immunostaining of Day 42 Brain Organoid.....	50
Figure 39 DAPI (Top Left), PSD95 (Top right), SYN (Bottom left), and 20x Merged (Bottom right) Immunostaining of Day 42 Brain Organoid.....	51
Figure 40 Hardware overview of Microelectrode Array System .....	52
Figure 41 Software overview of Microelectrode Array System .....	52
Figure 42 Microelectrode Arrays .....	54
Figure 43 Verification of MEA by microscope .....	55
Figure 44 External signal test by Netech MiniSim. The sin wave is generated at 50 $\mu$ V at 5 Hz .....	56
Figure 45 brain organoid SiP platform.....	56
Figure 46 Data package architecture.....	57
Figure 47 The initial prototype of brain organoid SiP platform.....	58
Figure 48 Verification of SPI communication protocol where line 1 is CS, line 2 is SPI clock, line 3 is MOSI, line 4 is MISO and line 5 is DRDY.....	58
Figure 49 Verification of ADS1298 configuration where line 1 is CS, line 2 is SPI clock, line 3 is MOSI, line 4 is MISO and line 5 is DRDY.....	59
Figure 50 Verification of data packaging process .....	59
Figure 51 preliminary verification of UART communication protocol .....	60
Figure 52 Sawtooth wave test (1-101) .....	60
Figure 53 Internal signal test by ADS 1298 .....	61
Figure 54 External signal test by Netech MiniSim. The sin wave is generated at 10 $\mu$ V at 5 Hz .....	62
Figure 55 External signal test by Netech MiniSim. The sin wave is generated at 100 $\mu$ V at 5 Hz .....	62
Figure 56 Schematic diagram of SiP PCB .....	63

Figure 57 Top view of SiP PCB layout.....	64
Figure 58 Verification of SiP PCB by microscope.....	64
Figure 59 Application User Interface .....	69
Figure 60 Verification flow of Threading .....	72
Figure 61 Verification flow of Buffer .....	72
Figure 62 Sawtooth Recorded signal .....	73
Figure 63 Experimental setup sideview (left), top view (right).....	74
Figure 64 Filtered electrophysiological signal from brain organoid day 35 (left) and day 42 (right). ...	75
Figure 65 Data of brain organoid pre-neurostimulation and post-neurostimulation .....	76
Figure 66 Data of brain organoid and noise.....	78
Figure 67 FFT and PSD Plot of the Raw Signal of Day 35 Brain Organoid .....	80
Figure 68 FFT and PSD Plot of the Raw Signal of Day 42 Brain Organoid Before Neurostimulation .	81
Figure 69 FFT and PSD Plot of the Raw Signal of Day 42 Brain Organoid After Neurostimulation ....	81
Figure 70 FFT and PSD Plot of the Filtered Signal of Day 35 Brain Organoid .....	82
Figure 71 FFT and PSD Plot of the Filtered Signal of Day 42 Brain Organoid Before Neurostimulation .....	82
Figure 72 FFT and PSD Plot of the Filtered Signal of Day 42 Brain Organoid After Neurostimulation	83
Figure 73 A Raster Plot of Day 35 Brain Organoid .....	87
Figure 74 Raster Plots of Day 42 Brain Organoid Before Neurostimulation.....	87
Figure 75 Raster Plots of Day 42 Brain Organoid After Neurostimulation.....	87
Figure 76 A Weighted Adjacency Matrix of Day 35 Brain Organoid.....	88
Figure 77 A Weighted Adjacency Matrix of Day 42 Brain Organoid Before Neurostimulation.....	89
Figure 78 A Weighted Adjacency Matrix of Day 42 Brain Organoid After Neurostimulation.....	89
Figure 79 Network Metrics of Day 42 Brain Organoid Networks Before Neurostimulation.....	93
Figure 80 Network Metrics of Day 42 Brain Organoid Networks After Neurostimulation. ....	94
Figure 81 Schematic Representation of Node Role Classifications in Functional Connectivity Network [45].....	95
Figure 82 A Density Landscape of Day 42 Brain Organoid Networks Before Neurostimulation .....	96

Figure 83 A Density Landscape of Day 42 Brain Organoid Networks After Neurostimulation.....	96
Figure 84 Raster plots of Day 35 and Day 42 Brain Organoid.....	97
Figure 85 Weighted Adjacency Matrices of Day 35 (Left) and Day 42 (Right) Brain Organoid .....	97
Figure 86 Raster plots of Day 42 Brain Organoid Before (Left) and After (Right) Neurostimulation... <td>99</td>	99
Figure 87 Weighted Adjacency Matrices of Day 42 Brain Organoid Before (Left) and After (Right) Neurostimulation.....	99
Figure 88 Changes in Functional Connectivity of Day 42 Brain Organoid Networks Before (Left) and After (Right) Neurostimulation.....	100
Figure 89 Node Cartography of Day 42 Brain Organoid Networks Before (Left) and After (Right) Neurostimulation.....	101

## LIST OF TABLES

Table 1 Additional materials and reagents required for brain organoid generation .....	29
Table 2 Equipment required for brain organoid generation .....	30
Table 3 Comparison of matrices on brain organoid signals and noise.....	77
Table 4 Frequency Range of Each Decomposition Level.....	84
Table 5 Network Metric Definitions [45].....	90
Table 6 Functional Role Definitions Based on Node Classifications [45].....	95

## **ABBREVIATIONS AND ACRONYMS**

AI	Artificial Intelligence
BCI	Brain Computer Interface
BCT	Brain Connectivity Toolbox
BLE	Bluetooth Low Energy
CAR	Common Average Referencing
CNNs	Convolutional Neural Networks
CPU	Central Processing Unit
CS	Chip Select
CWT	Continuous Wavelet Transform
EEG	Electroencephalogram
ENIG	Electroless Nickel Immersion Gold
FDA	Food and Drug Administration
FFT	Fast Fourier Transform
FPC	Flexible Printed Circuit Board Connector
fPCB	Flexible Printed Circuit Board
FPGA	Field Programmable Gate Array
GFAP	Glial Fibrillary Acidic Protein
HDF5	Hierarchical Data Format, version 5
hiPSCs	Human Induced Pluripotent Stem Cells
hPSCs	Human Pluripotent Stem Cells
Hz	Hertz
ICA	Independent Component Analysis
IIR	Infinite Impulse Response
ISI	Interspike Intervals
JSON	JavaScript Object Notation
LFP	Local Field Potential
LIF	Leaky Integrate-And-Fire
MAD	Median Absolute Deviation
MAP2	Microtubule-Associated Protein 2
MD	Mean Deviation
MEAs	Microelectrode Arrays

NaCl	Sodium Chloride
NMDA	N-methyl-D-aspartate
OI	Organoid Intelligence
ONNs	Organoid Neural Networks
PCA	Principal Component Analysis
PCB	Printed Circuit Board
PGA	Programmable Gain Amplifier
PSD	Power Spectral Density
RMS	Root Mean Square
SEM	Standard Error of the Mean
SiP	System in Package
SNR	Signal-To-Noise Ratio
SOC	System On Chip
SPI	Serial Peripheral Interface
STDP	Spiking Timing Dependent Plasticity
STTC	Spike Time Tiling Coefficient
SVRT	Synthetic Visual Reasoning Test
SYP	Synaptophysin
UI	User Interface

# CHAPTER I

## INTRODUCTION

### 1.1 Project Overview

Artificial Intelligence (AI) has profoundly transformed nearly every aspect of modern life, revolutionizing advancements across industries. Its versatile applications continue to reshape traditional processes, enabling innovative solutions and pushing the boundaries of what is possible in technology and human interaction. Despite its rapid advancement, AI still encountered limitations rooted in its architectural structure, particularly the von Neumann bottleneck. This constrains AI's ability to efficiently process large-scale complex data. Unlike traditional AI, biological neural networks, such as the human brain, excel in seamlessly integrating memory and computation, allowing rapid and energy-efficient processing of complex information. The brain's adaptability and ability to learn and make decisions in real time far surpass current AI capabilities. This emphasizes the urgent need for alternative computing paradigms capable of mirroring such performance of the human brain.

Neuromorphic computation emerges as a promising solution, offering a computational architecture modeled after the structure and functionality of the biological brain, with interconnected neurons and synapses driving its design. By integrating memory and processing in the way neurons connect, neuromorphic systems can reduce energy consumption while enhancing computational ability. Central to these systems are Spiking Neural Networks (SNNs), which mimic the spike-based communication of biological neurons, enabling asynchronous, event-driven processing. These features allow neuromorphic systems to leverage highly parallel operations, where processing and memory are not separated but occur simultaneously, enabling mitigation of von Neumann bottleneck and efficient data handling with significantly lower energy demands and greater capacity to process complex structures. This innovative approach aligns closely with brain organoids, which serve as a model to replicate the neural architecture and dynamic processes of the human brain, offering valuable insights for advancing neuromorphic computation.

Our study focuses on leveraging cerebral organoids, derived from human-induced pluripotent stem cells (hiPSCs), to emulate the biological processes of the human brain. These organoids, as a simplified model of brain tissue, serve as a platform for investigating neural activity for SNNs modeling. By integrating cerebral organoids with advanced Microelectrode Arrays (MEAs) system, we aim to develop a novel Brain Organoid-Computer Interface for continuous electrophysiological monitoring. This system will provide insights into the spiking activity of the organoids, allowing us to evaluate their feasibility for SNNs modeling.

By demonstrating the potential of cerebral organoids as living models for AI development, this research seeks to advance the frontiers of both neuroscience and artificial intelligence. In merging the biological with the computational, we hope to unlock new possibilities that will not only enhance our technological capabilities but also deepen our understanding of the human brain itself. As we navigate this innovative intersection of disciplines, the future of intelligent systems will increasingly rely on lessons drawn from the biological world, paving the way for a more sophisticated and adaptive approach to AI.

## 1.2 Task Breakdown

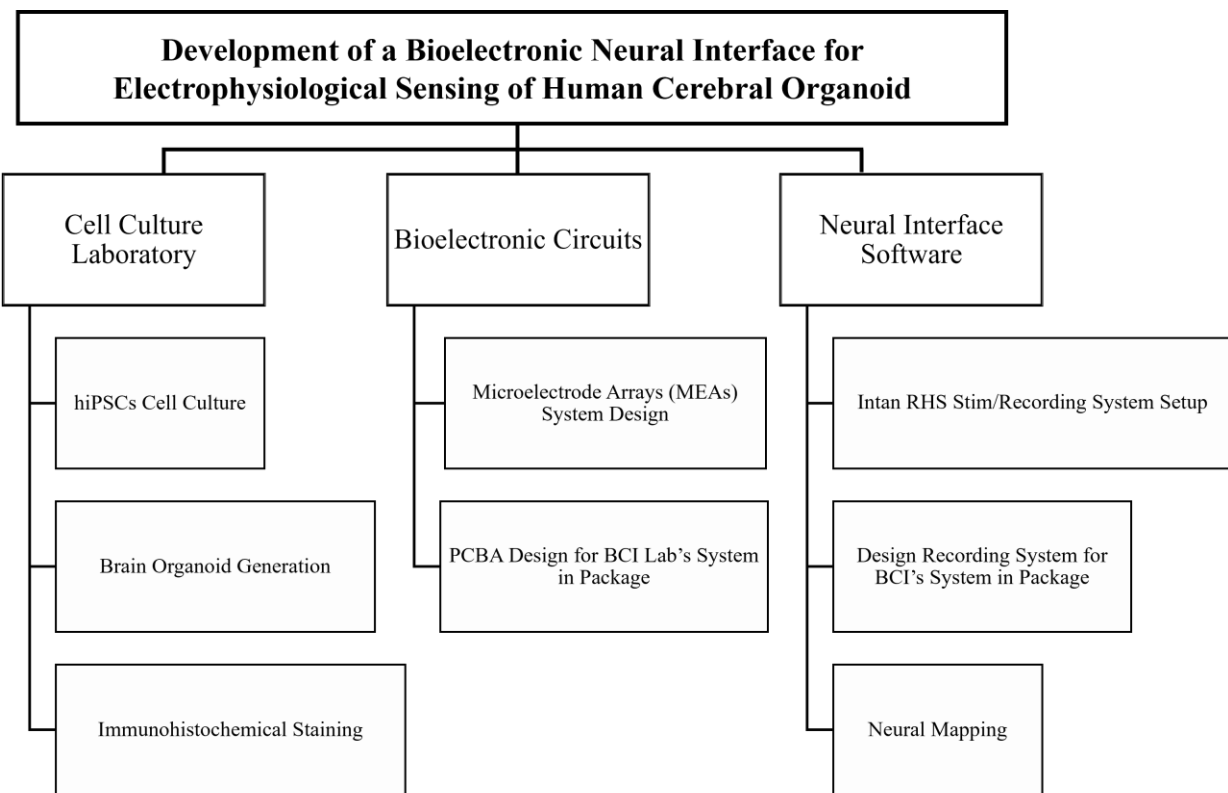


*Figure 1 Task Breakdown*

## CHAPTER II

### PROBLEM STATEMENT

#### **2.1 Problem Statement**

AI has rapidly become an integral part of our daily life, from voice assistants and recommendation algorithms to self-driving cars and even frontier medical research use AI for analytic, diagnosis, and therapeutic applications. Study guided by PRISMA protocol investigate 3,767 research articles with 63,577 citations using thematic clustering and BERTopic modeling categorizes dominance of AI studies into 4 clusters; AI in healthcare and life sciences informatics; AI in engineering systems and sustainable technologies; AI-enhance business intelligence and strategic management; AI in computational technologies and human-centric system [1]. Despite these advancements, current AI are limited by von Neumann bottleneck which only allows sequential processing of information through the computers processing unit [2].

Human brains are slower in processing simple tasks, arithmetic for example, but they surpass von Neumann computers in terms of processing complex and uncertain data using parallel processing. Research conducted using Synthetic Visual Reasoning Test (SVRT) and Parametric SVRT has demonstrated that Convolutional Neural Networks (CNNs), despite their success as deep learning image classification models, they struggle with learning abstract visual relationships that humans and even non-primates like rodents, birds, and insects recognize effortlessly [3]. Parallel processing abilities allow human brain to outperform those computers in both aforementioned learning abilities and power efficiency. For instance, an adult human consumes approximately 2,000 calories per day, as the brain accounts for 20% of metabolic load indicating that the human brain operates efficiently at 100 watts power [4, 5]. On the other hand, a supercomputer running at the same speed of human brain requires 21 megawatts power to keep running, this makes computers  $10^6$  times less energy efficient [6, 7]. These limitations of von Neumann architectures faced by current AI systems highlight the needs for an alternative computational architecture to advance AI beyond its current capabilities.

## **2.2 Objectives and Expectations**

Considering the critical limitations of current AI systems, it has become essential to explore other alternative approaches that mimic the human brain's biological processing. This study seeks to advance the understanding of brain-inspired computational architecture using cerebral organoid, paving the way for novel applications in neuromorphic computation and brain-computer interface. To achieve this, our research focuses on the following key objectives:

- To generate hiPSCs-derived cerebral organoids then evaluates its functionality observing their immunohistochemical markers
- To develop a novel Microelectrode Array-based Brain Organoid-Computer Interface system for electrophysiological monitoring of cerebral organoids
- To investigate the feasibility of cerebral organoid as a model for Spiking Neural Networks computational architecture used in neuromorphic computation

## **CHAPTER III**

### **DESIGN APPROACH**

#### **3.1 Design Specification**

##### **3.1.1 Ethical Consideration**

The hiPSCs, reprogrammed from patient samples, have obtained ethical approval from Ramathibodi Hospital. Detailed information regarding the specific strain will be provided once the samples are chosen and received.

##### **3.1.2 Cerebral Organoid**

The cerebral organoid must be morphologically accurate, exhibiting a bubbling surface with dense necrotic core and a display of optically translucent edges. It should expand sufficiently reaching approximately 2 mm in diameter. Key structures, including neuronal and non-neuronal markers, must be observable through immunohistochemical staining to ensure that the organoids are accurate and could serve as a reliable model for electrophysiological studies.

##### **3.1.3 Microelectrode Array System**

The MEAs system must allow precise, stable, and non-invasive electrophysiological monitoring of the reproduced organoids. It should be able to capture both local field potentials and spiking activities across multiple channels. These activities must be parallelly handled through signal acquisition system simultaneously to support real-time monitoring and analysis.

##### **3.1.4 Spiking Neural Networks Modeling Feasibility**

Detailed neural mapping of the brain organoid activities is essential to access the feasibility of SNNs modeling. Therefore, the spike sorting algorithm must be able to extract single-unit activity from the raw extracellular recordings, forming a basis for a mathematical model that can assess the functional connectivity. SNNs modeling will be feasible if the network structure of the organoid is determined to be non-random, as this would indicate organized and interpretable neural interactions.

### 3.2 Initial Design

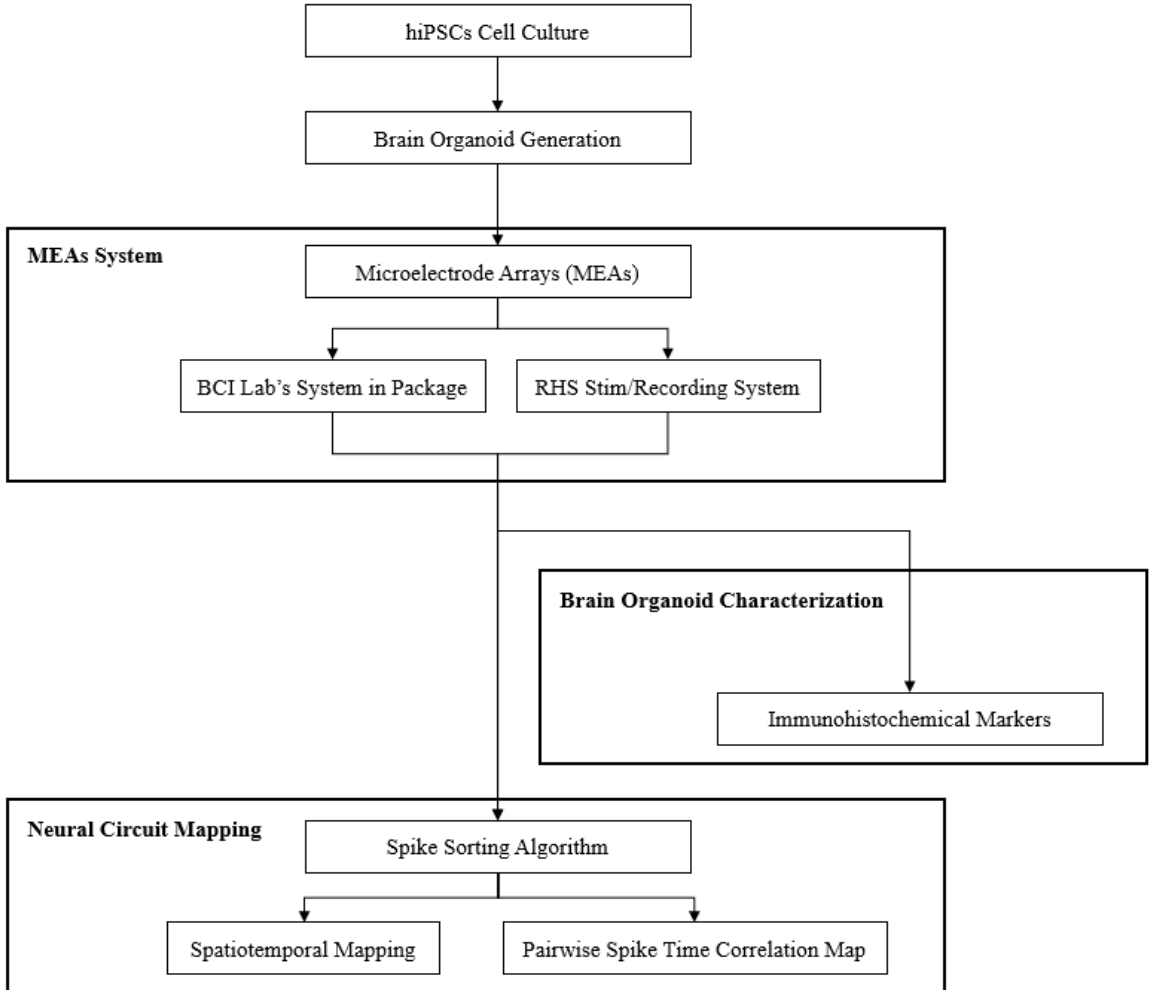


*Figure 2 Schematic Diagram of the Initial Design*

To evaluate the feasibility of brain organoid for SNNs modeling, our design focuses on 3 main aspects: Brain Organoid Characterization, MEAs System, and Neural Mapping. Our workflow begins with culture of hiPSCs and the subsequent generation of cerebral organoids. The electrophysiology of the generated organoid shall be recorded by using MEAs system, which integrates two primary components: the MEAs and the data acquisition systems. We employed 2 data acquisition systems, the Brain Computer interface (BCI) Lab's System in Package (SiP) is our own novel platform for electrophysiological monitoring, and the RHS Stim/Recording System is Intan Technologies gold standard for miniaturized electrophysiology work. After the signals are collected, the organoids will be sliced into thin layers then stained for immunohistochemical markers observation, this is to validate their viability for electrophysiological studies. Lastly, the data will be sorted and mapped to assess the functional connectivity, thereby determining the feasibility of brain organoids for SNNs modeling.

## CHAPTER IV

### CONCEPT SYNTHESIS

#### 4.1 Prior Art

##### 4.1.1 Brain Organoid: A Pathway to AI Applications

Brain organoids, or cerebral organoids are three-dimensional multi-cellular brain culture generally derived from human pluripotent stem cells (hPSCs) or hiPSCs. Although, two-dimensional neural culture presents with higher level of homogeneity, they lack the intricate organization and complexity that organoid could provide. These 3D cultures recapitulate the key features exhibited in developing fetal human brain in terms of the maturation process, cytoarchitectures, and notably cell diversities [8]. A study that conducted a single-cell transcriptome analysis on 166,242 cells extracted from 21 individual dorsal forebrain organoids demonstrated wide-variety of both neural and non-neural cell types. The 3-month PGP1 organoids exhibited a composition of 86.5% neurons and 13.5% glial cells containing projection neurons, callosal projection neurons; intermediate progenitor cells; corticofugal projection neurons, radial glia, astroglia, outer radial glia, cycling progenitors, and their immature cell types. Alongside this, 6-month PGP1 organoids exhibited 43.7% neurons, 53.5% glial cells, and the unknown rest with an additional of immature inhibitory interneurons and cycling inhibitory interneuron precursors. Immunohistochemical markers show the presence of pan-neuronal marker, Microtubule-Associated Protein 2 (MAP2) within 1-month, whereas astrocytic markers S100B and Glial Fibrillary Acidic Protein (GFAP) only appear at 6-month-old organoid [9].

The complexity and cellular diversity exhibited by the brain organoid provides opportunities in numerous scientific domains. In developmental neuroscience, brain organoids are employed for disease modeling. For instance, studies have demonstrated an increase in amyloid- $\beta$  peptides ( $A\beta$ ) and phosphorylated tau accumulation in brain organoid derived from Alzheimer's patients carrying APOE4 genes. RNA-sequencing of organoid was performed revealing the altered transcriptomes and therapeutic intervention is suggested by genome editing from APOE4 to APOE3 gene to alleviate the disease [10]. Similarly, in toxicology, organoids are revolutionizing drug screening and precision medicine by training network model using Alzheimer's cerebral organoid treated with Food and Drug Administration-approved drugs [11]. Beyond these applications, brain organoids are paving the way for applications in AI. Their capabilities to replicate *in vitro* and *in vivo* features of human brain can be harnessed through

electrophysiological analysis to create more sophisticated AI system that mimic neural processing [2]. This integration holds the promise of cognitive computing, allowing algorithms to analyze complex data patterns in a manner that mirrors human thought processes.

#### 4.1.2 Electrophysiology as a Platform for Brain Mimicry

Electrophysiology is one of the cores of the neuron operation process, making it a natural basis for creating brain-mimetic systems. In 1952, the Hodgkin-Huxley or H-H model, a highly robust model for analog neuron behaviors, was invented by Alan Hodgkin and Andrew Huxley when they studied the transmission mechanism of neural signals by using a squid. They discovered the change of neural membrane potential, called the action potential. In the experiment, they found three different types of ion current including sodium current, potassium current, and leaky current [12]. The potassium channel and sodium channel were found to be involved with the spiking activity [13]. The H-H model describes the organelle of neurons as an electronic component. A semi-permeable cell membrane of the neurons is represented by a capacitor. Resistors and batteries represent the properties of each channel. Last, the electrical current represents the storage of electric charge on a cell membrane as seen in Figure 3.

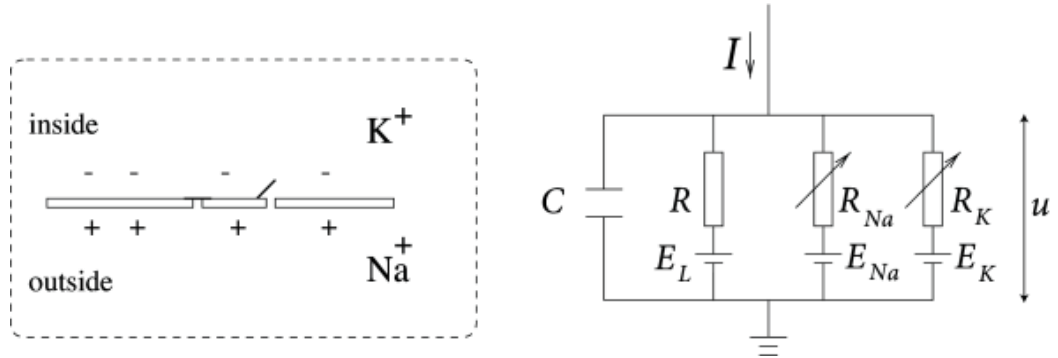


Figure 3 Schematic diagram based on the Hodgkin-Huxley model, illustrating the biological representation of a neuronal cell membrane (left) and its equivalent electrical circuit (right) [12].

According to Figure 3, the electrical circuit of the H-H model can be written in an ordinary differential equation which mimics the opening and closing mechanism of each ion channel.

$$C_m \frac{dv_m(t)}{dt} = G_K n^4 (v_m - E_K) + G_{Na} m^3 h (v_m - E_{Na}) + G_L (v_m - E_L) + I_{syn}(t) \quad (1)$$

where  $C_m$  is capacitance of semi-permeable cell membrane,  $v_m$  is the potential voltage potential across semipermeable cell membrane,  $I_{syn}$  is synaptic input current,  $G_k$  represents conductance of potassium ion,  $E_k$  represents reversal potential of potassium ion,  $G_{Na}$  represents conductance of sodium ion,  $E_{Na}$  represents reversal potential of sodium ion,  $G_L$  represents conductance of leak ion, and  $E_L$  represents leak reversal potential. n, m, and h are the activation and inactivation probability of each channel ion types which are potassium channel activation, sodium channel activation, and sodium channel inactivation, respectively. These three-gate probability can be calculated from differential equation (2) to equation (8) where g represents the gating variables n, m, and h,  $\alpha_g(v)$  is the transition rate from non-permissive to permissive states, whereas  $\beta_g(v)$  is the transition rate from permissive to non-permissive states.

$$\frac{dg}{dt} = \alpha_g(v_m)(1 - g) - \beta_g(v_m)g \quad (2)$$

$$\alpha_m(v_m) = \frac{0.1(25-v_m)}{\exp(\frac{25-v_m}{10})-1} \quad (3)$$

$$\beta_m(v_m) = 4\exp(-\frac{v_m}{18}) \quad (4)$$

$$\alpha_h(v_m) = 0.07\exp(-\frac{v_m}{20}) \quad (5)$$

$$\beta_h(v_m) = \frac{1}{\exp(\frac{30-v_m}{10})+1} \quad (6)$$

$$\alpha_n(v_m) = \frac{0.01(10-v_m)}{\exp(\frac{(10-v_m)}{10})-1} \quad (7)$$

$$\beta_n(v_m) = 0.125\exp(-\frac{v_m}{80}) \quad (8)$$

After all these equations are computed, the H-H model can generate the spike which is analogous to the neurons. The result of this model provides high accuracy in the biological aspect, but it requires enormous computational resources which are unsuitable for large-scale simulation [13]. The H-H model has become the remarkable foundation of neuroscience research [14].

Over the decades, numerous novel models have been developed based on the H-H model, creating a balance between degrees of biomimicry and computational resources.

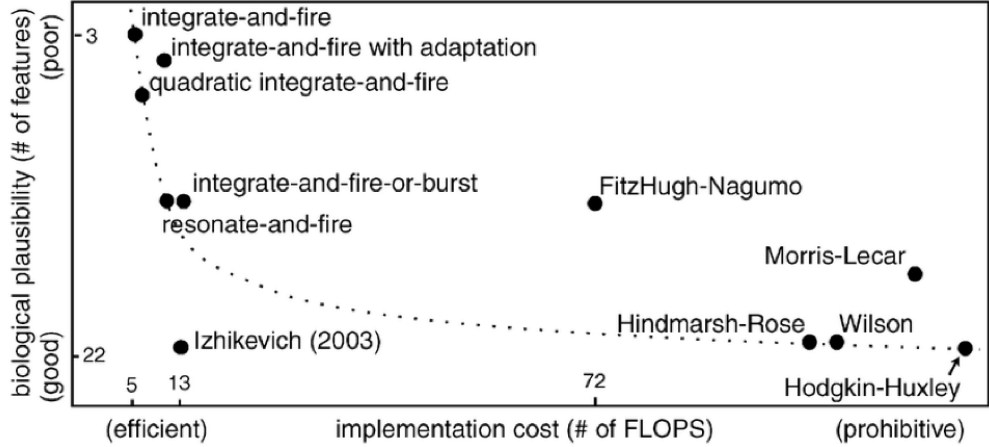


Figure 4 A comparison of spiking neuron models based on computation resource and degree of biomimicry [13].

For example, the integrate-and-fire (IF) model has the same physical principle as the H-H model, but this model will generate the spike only if the input current must reach the threshold voltage. The IF model ignores the actual behavior of semi-permeable cell membrane and the influence of leakage current, leading to the mathematical equation (9) and (10).

$$C_m \frac{dv(t)}{dt} = \frac{c_m}{\tau_m} [v(t) - V_0] \quad (9)$$

$$v(t) = v_0 + \mu_\omega t + \sigma_\omega W(t), t > 0 \quad (10)$$

As the simplicity of the IF model, the degree of biomimicry is not as high as in the H-H model. Still, the computational resource is improved which is capable of dealing with larger-scale simulation [14].

The leaky integrate-and-fire (LIF) model, improved from the IF model, is another model that improved computational resources. Several intensive values such as membrane capacitance, etc. are simplified and the leak current effect is also considered, leading to the enhancement of the degrees of biomimicry without increasing the computational complexity [14]. Therefore, the LIF model has become one of the choices that are widely used to mimic the behaviors of neurons. The mathematical equation of LIF model is illustrated in equation (11) and (12).

$$C_m \frac{d\bar{v}_m}{dt} = -G_L(\bar{v}_m - E_L) + I_{syn}(t) \quad (11)$$

$$\text{if } \bar{v}_m \geq v_\theta, \bar{v}_m \leftarrow v_{peak} \text{ then } \bar{v}_m \leftarrow v_{reset} \quad (12)$$

The spikes, produced from those models, will be continuously processed on learning algorithms which establish the functional connectivity of neurons. The learning algorithm can be divided into two types, including unsupervised and supervised learning algorithms. Each algorithm such as spiking timing dependent plasticity (STDP) and SpikeProp utilizes spikes to enhance deep learning with high accuracy. Therefore, the spike becomes the foundation to develop SNNs [15].

In brain organoids, electrophysiology can be used to evaluate their key functions, cellular diversities, and even anatomical organization [16, 17]. The action potentials in brain organoids are initiated from glutamatergic neurons, which are mostly pyramidal cells, and it is inhibited by GABAergic neurons [8]. These working mechanisms establish network activities that drive the connectivity of the cerebral organoid, which can be observed through the extracellular recording. There are 2 main frequency bands used for the analysis, 1 Hz to 1,000 Hz called the Local Field Potential (LFP), and 300 to 3,000 Hz which is the neuronal bursts [18]. LFP refers to the summation of synaptic and transmembrane current in the local network at the microscale level, it is typically around 50  $\mu$ V peak to trough [19]. One study found that the LFP neural oscillation in cortical organoid networks is similar to the preterm human electroencephalography, this provides an opportunity to manipulate network activity in the developing human cortex through genetic engineering to treat neurological diseases [20]. The 300 to 3,000 Hz frequency band is generally used for spiking activity detection of single neurons, it is used for analysis of neuronal burst and network activity applications [16]

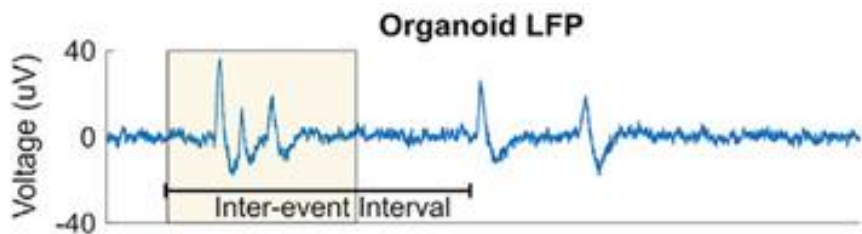


*Figure 5 The shape of LFP and spikes from brain organoid [19].*

The research on functional neuronal circuitry in human brain organoids report that LFP can be generated which have synchronized activities in the delta oscillations (1-4 Hz), theta oscillations (4-8 Hz) and gamma frequency oscillations (100-400 Hz). Moreover, the spike characteristic is found in the pattern of non-random firing [16]. Similarly, another research on complex oscillatory waves also found the LFP with the spike characteristic can be detected from cortical organoid by low pass filtering at 3,000 Hz. In addition, the spikes can be extracted by applying a band pass

filtering at 300 Hz to 3,000 Hz, while LFP without spike can be seen when using a low pass filtering at 1,000 Hz [20]. As these neural activities which appear from brain organoids play a crucial role in spiking models, an electrophysiology which is measurement of electrical activities of cells arise from action potential or member potential change must be conducted to investigate properties and characteristics. Therefore, electrophysiology is considered as the hallmark of functional and connectivity analysis for brain organoid, which is the bridge to spiking neural network, leading to ultimately apply in AI [21].

To achieve an extracellular recording, an instrument for extracellular electrophysiological measurement is needed. MEAs are considered as a high potential method compared to patch clamping and calcium imaging technique. Patch clamping technique is conducted to record electrical activity of individual neurons in millisecond scale, whilst technique is calcium imaging which utilizes the change of calcium concentration upon occurrence of action potential instead of voltage change. Both techniques have a tradeoff between temporal resolution and spatial resolution. In contrast to both techniques, MEAs is a non-invasive tool which utilizes multiple microscopic electrodes on rigid or flexible substrate to record potential change in the extracellular space around neurons from a few days up to several months. Therefore, MEAs allow a real-time network-scale and wide temporal resolution monitoring and stimulation of neural activity which can provide an efficient interface to examine the computational characteristics of the brain organoid [21, 18]. To construct MEAs, all designs aim to optimize their MEAs to have high signal-to-noise ratios (SNR) and low electrode impedance, resulting in a high quality of input signal [22]. A study on MEAs development successfully construct flexible four-channel 2D MEAs and three-channel 3D MEAs by silicon wafer-integrated self-folding polymer through the process of photolithography. With the optimization of electrode patterns via simulation and experiment, the surface can fully contact with a brain organoid for 2 weeks to 10 weeks. In validation process which simulate organoid by glutamate, the spike is acquired 2,025 firing spikes from 2D MEAs and 7,785 firing spikes from 3D MEAs. The results illustrate that 3D MEAs are significantly higher SNR and more sensitive than 2D MEAs due to the higher number of planes [23]. Similarly, the research article of bioelectronics for electrophysiology in brain organoid reports the advantage of 3D MEAs over 2D MEAs which provide electrophysiology in 3D structures, accessing the 3D complexity of neural network of brain organoid. However, 2D MEAs are more stable in long-term recording than 3D MEAs due to the simplicity of design [24].

In electrophysiology recording, an analog front-end and recording system plays a curial role as the major component in data acquisition system, aiming to provide low latency with higher degree of parallel process [24, 25]. Multiple studies associated with electrophysiology recording by MEAs use the commercial product from Intan technology which are RHD Recording System and RHS Stim/Recording System to record data, considered as the gold standard of miniature electrophysiological equipment. First, there is a study that develops multifunctional data acquisition system for electrophysiology with MEAs. They propose the integration between 64-electrode MEAs from Multi Channel GmbH with 32-channel RHD2132 chips from Intan Technology product, connected to INTAN RHD2000-EVAL board. The RHD2132 amplifier plays role as recorder and impedance measurement tool. In this study, the specification of RHD2132 is utilized the with 30,000 sample per second at fixed gain of 200x and has vertical resolution of input signal at  $0.195 \mu\text{V}$ . These specifications are already beyond electrophysiology study from neuron [26]. In another research, they focus on the development of MEAs system for brain organoids. The stretchable 3D MEAs have been proposed and conducted with 16-channel Stim/Recording headstage and Intan RHS data acquisition software, which is another version product of Intan, allowing to perform stimulation which perform on flexible 3D MEAs. The result of this research shows more consistent in simulation purpose than traditional bipolar stereotrode [27]. With the promising ability of Intan Technology product to perform in electrophysiology study, the cost is still too high for accessibility. The SiP from BCI Lab can be an alternative potential and cost-effective solution in electrophysiology recording, consisting of ADS1298 and BlueNRG-LP. ADS1298 is an analog front end composed of 8-channel low-noise programmable gain amplifiers (PGAs) and high-resolution analog-to-digital converters (ADCs). ADS1298 has provided the sufficient minimum resolution at  $0.14 \mu\text{V}$ , being compatible choice for electrophysiology recording [28]. On the other hand, BlueNRG-LP is microcontroller unit (MCU) which has ultra-low power Arm® Cortex®-M0, resulting in high energy efficient system on chip (SOC) [29]. Meanwhile, the recording controller from Intan technology implements a Field Programmable Gate Array (FPGA) for data processing. Research on MEAs acquisition systems using FPGA computing has demonstrated its high efficiency in real-time extracellular potential recording from neurons [25]. Similarly, another study on enhancing MEA systems with FPGA for neuronal signal recording reported that FPGA, when combined with planar high-density MEAs, can efficiently perform parallel spike detection across 4,096 electrodes with digital filtering at an 8 kHz sampling rate [30]. While FPGA offers superior parallel processing performance, MCU present an alternative such as low power consumption

and ease of use. There is an investigation on MCU-based multichannel system for electrophysiology recordings in mammalian brains using ESP-32 board. This system enables wireless transmission of neural data recorded from a 16-channel MEA at a 25 kHz sampling rate per channel [31]. Similarly, a low-power Bluetooth Low Energy (BLE)-enabled MCU, nRF52840, was employed for real-time neural data acquisition in rodent brain studies. This system efficiently connects to a custom-designed 12-channel MEA, enabling simultaneous multi-channel recordings, signal digitization, and wireless data transmission while maintaining a low-power architecture suitable for long-term recordings in freely moving subjects [32]. These findings confirm that the BlueNRG-LP MCU, with BLE 5.0 and low-power operation, could serve as a cost-effective and efficient platform for Electroencephalogram EEG recordings in brain organoid as well.

#### **4.1.3 Brain Organoid as a Biological Processors**

Organoid Intelligence (OI) has emerged as a promising technology that goes beyond traditional artificial neural networks by incorporating biological components into computational systems. This advancement is driven by breakthroughs in stem cell research and neuroscience, enabling the development of biohybrid computing models. OI is the concept of utilizing a brain organoid, a self-organized 3D structure that mimics developmental and functional aspects of the human brain, as a biological processor in an Organoid-On-a-Chip technology. The integration of this biological neural network with artificial intelligence has opened new possibilities in advanced biocomputing, leveraging the adaptive and learning capabilities of neurons for computational and cognitive tasks. Shultz et al. [33] have demonstrated this potential by cultivating murine cortical neurons on multi-electrode arrays, enabling them to function as a simplified central nervous system. These neuronal networks processed sensory inputs, such as video signals, and generated motor responses in robotic systems. Their findings underscored the potential applications of ex vivo neuronal networks in fields like neuroprosthetics and research on neurodegenerative diseases. Similarly, Smirnova et al. [34], the DishBrain model, studied the ability of brain organoids to interface with computers and sensors, allowing them to engage in both supervised and unsupervised learning through biofeedback mechanisms, where organoids receive and respond to increasingly complex sensory inputs. This approach allows neural culture to successfully learn to play computer games, demonstrating their ability to process information dynamically and solve problems accordingly.

Further advancing the concept of biocomputing, human-derived neural cells are increasingly being explored as computational units due to their intrinsic ability to process and transmit information. Neurons are capable of processing various inputs, including electrical and chemical signals, synthetic data from machine sensors, and natural signals from sensory organoids [35]. Communication between neurons occurs through synapses, where electrical signals are converted into chemical signals and others [36]. When stimulated, Organoid Neural Networks (ONNs) exhibit neuroplasticity, forming adaptive connections that evolve in response to external stimuli [37]. This neuroplasticity property serves as the foundation of Brainoware, a biocomputing platform that employs ONNs for real-time computational tasks. According to Cai et al. [38], Brainoware operates through stimulus-response training and uses adaptive reservoir computing to process spatiotemporal information through unsupervised learning. Its architecture consists of an input layer that converts time-dependent input data into spatiotemporal sequences of electrical pulses, a reservoir layer of organoid map inputs to a high-dimensional computational space of ONNs, and an output layer that decodes neural activity for real-time tasks like classification, time-series analysis, and prediction. Through unsupervised learning, Brainoware dynamically restructures its neural connections, enhancing computational performance over time. Unlike conventional digital systems that rely on binary processing, organoid-based computing operates through continuous, analog-like signaling, making it particularly effective for pattern recognition and complex problem-solving [20].

#### **4.1.4 Neuromorphic Designs Inspired by Brain Organoid**

With von Neumann architecture approaching their performance limits, many in the computing industry are exploring alternatives to improve computing capabilities. One such promising technology is the neuromorphic computer which has structure and functions similar to the brain. In contrast to von Neumann architecture and organoid intelligent platforms, neuromorphic computers use neurons and synapses as their storage and processing units simultaneously instead of the Central Processing Unit and Random-Access Memory of von Neumann, and biological tissue of the organoid intelligent platforms. These components provide an abstraction level that is meant to be simplified as well as time and temporal considerations to efficiently handle both processor and memory activities. Brain-like efficiency requires specialized software to be co-designed with corresponding hardware capable of event-driven dynamic workloads. These computers use a biologically inspired algorithm called Spiking Neural Network that imitates the functioning of biological neurons. Instead of binary values,

numerical information is encoded using timings, amplitudes, and shapes of neural spikes. Unlike conventional artificial neural networks, where input is treated synchronously, the use of SNNs enables an asynchronous operation of the network since synapses and neurons have varying delays, making a more accurate simulation of the temporal dynamics that characterize biological neuronal systems. Because of this event-driven nature, only the essential components are activated for specific activities, resulting in high efficiency and low-power operation that outperforms the energy demands of traditional computing systems [2, 39, 40].

The study of neural circuit mapping has grown in importance as a means of understanding how neurons connect, organize into networks, and execute tasks. This mapping can be categorized into network-wide and single-cell activity mapping. Network-wide mapping focuses on large-scale neural dynamics, capturing population-level activity metrics such as firing rates, LFP, and synchronized bursts. Techniques like spike detection, cross-correlation, and coherence analysis help characterize functional connectivity at this broader scale. In contrast, single-cell mapping offers fine-scale insights by tracking the activity of individual neurons. This process often involves spike sorting techniques to distinguish signals from different neurons recorded on the same electrode, facilitating a detailed understanding of cellular-level interactions and computations. An accurate spike detection is a critical step in analyzing neural activity and understanding the functional architecture of brain organoids. This process typically begins with identifying action potential from multi-unit recordings using various spike detection methods. The threshold-based method is one of the most used approaches, where neural spikes are detected by comparing signal amplitudes to a predefined voltage threshold. One of the main challenges in this approach is determining an appropriate threshold level to distinguish true spikes from background noise. To optimize threshold selection, the SNR is used as a metric and calculated using the equation (13).

$$SNR = \frac{\text{Mean Peak Amplitude of Spikes}}{\text{Standard Deviation of Background Noise}} \quad (13)$$

where background noise is typically estimated using the Root Mean Square (RMS) voltage when no spikes are present, with higher RMS values indicating greater noise levels. If the SNR is too low, noise contamination increases, while excessively high SNR may lead to the omission of real spikes. Setting the spike detection threshold as a multiple of the noise level is a widely adopted practice in neural signal processing due to its computational efficiency. Rizk and Wolf evaluated various methods for estimating noise levels to optimize threshold selection [41]. Their study

examined four different operators: Mean Deviation (MD), RMS, 84th percentile (P84), and 68th percentile of absolute values (PA68). Given the non-Gaussian nature of neural signals due to high-amplitude spikes, these estimators yielded different results. RMS, P84, and PA68 effectively approximated the standard deviation in normally distributed data, while MD used an alternative formula. Their findings indicate that despite its widespread use, the RMS-based method was the least effective for setting thresholds, even though it is often implemented by setting the threshold around 5.5 times the RMS voltage on each electrode. To enhance robustness, alternative methods have been explored, such as using the median absolute deviation (MAD) instead of standard deviation estimates. Unlike RMS, MAD is less sensitive to outliers, making it a more reliable approach for threshold determination in neural signal detection. This method estimates the noise standard deviation using the equation (14).

$$\sigma_n = \text{median} \left\{ \frac{|x|}{0.6745} \right\} \quad (14)$$

where  $x$  represents the filtered signal. The threshold is then typically set as a multiple between two and four times  $\sigma_n$ . This range is guided by statistical principles and practical considerations in electrophysiological data analysis. Since background noise often follows a Gaussian distribution, setting a threshold between  $2\sigma_n$  and  $4\sigma_n$  effectively excludes 95-99.7% of noise fluctuations while preserving genuine neural spikes. However, an excessively high threshold (above  $4\sigma_n$ ) risks omitting valid low-amplitude spikes, while a lower threshold (below  $2\sigma_n$ ) may introduce false positives. This adaptive thresholding method is advantageous because it normalizes spike detection relative to noise levels, accommodating variations in neural signals caused by electrode placement, neuron type, and tissue properties. Empirical studies suggest that  $3\sigma_n$  often optimally distinguishes true spikes while minimizing false detections. To ensure reliable spike sorting, an initial threshold is typically set and later refined based on the SNR [42]. Another effective spike detection method is template-based detection, which utilizes multi-resolution wavelet decomposition, statistical analysis, and Bayesian hypothesis testing to accurately identify neural spikes. Wavelet transformations provide a time-scale representation of the signal, allowing transient events such as neural spikes to be efficiently isolated. By projecting neural signals onto predefined wavelet functions, this method identifies spike-related regions based on wavelet coefficients. A threshold-based denoising approach, inspired by Donoho and Johnstone's wavelet shrinkage technique, is applied to detect statistically significant coefficients that correspond to neural spike events. This hypothesis-testing framework eliminates the need

for inverse wavelet transformation and dynamically adjusts threshold values to accommodate variations in background noise. Wavelets and wavelet transforms are mathematically defined using equations (15) and (16).

$$\varphi_{a,b}(t) = \frac{1}{\sqrt{a}} \varphi\left(\frac{t-b}{a}\right) \quad a, b \in R \quad (15)$$

$$Tx(a, b) = \int_R x(t) \varphi_{a,b}(t) dt \quad (16)$$

where the function M represents the wavelet, which is a time-scale waveform generated through translation and scaling operations. The parameters a and b correspond to the scale and translation factors respectively, which control the stretching and shifting of the wavelet function [43]. The effectiveness of this method is largely influenced by the selection of an appropriate wavelet function. Extracellularly recorded action potentials typically exhibit biphasic waveforms, characterized by an initial negative deflection due to inward sodium ( $\text{Na}^+$ ) current, followed by a positive deflection caused by outward potassium ( $\text{K}^+$ ) current. However, spike morphology can vary depending on factors such as electrode placement, neuronal activity, and recording conditions, sometimes appearing as purely negative, purely positive, or even triphasic waveforms. Wavelets that closely resemble these natural spike shapes provide a sparse signal representation, which enhances noise separation and improves detection accuracy. Biorthogonal wavelets, such as bior1.3 and bior1.5, have demonstrated superior alignment with recorded spike templates compared to other wavelets like db2 [44]. The main advantage of template-based detection over threshold-based methods is its ability to improve both sensitivity and specificity. By identifying spikes based on their morphology rather than just amplitude thresholds, this approach is less susceptible to large artifacts and variations in spike frequency across different recordings. Additionally, the continuous scaling capabilities of wavelet transforms offer finer control over spike detection thresholds compared to traditional dyadic scaling methods [45]. Beyond these traditional methods, emerging algorithmic approaches such as non-linear energy operators [46], entropy-based detection [47], and fractal analysis [48] offer additional improvements in spike detection. These methods enhance noise resilience and computational efficiency while maintaining high detection accuracy. More recently, machine learning techniques, including shallow neural networks, have shown promise in automating spike detection and event classification, further advancing the field.

Once spikes are detected, spike sorting is performed to classify spikes into distinct groups, potentially corresponding to different neurons for cellular level study. This process

involves three main steps: feature extraction, dimensionality reduction, and clustering. Feature extraction analyzes spike waveforms based on parameters such as peak amplitude, width, and shape. To facilitate clustering, dimensionality reduction techniques like Principal Component Analysis (PCA), Independent Component Analysis (ICA), and t-SNE reduce the number of variables while preserving key distinctions in spike morphology. The final clustering step categorizes detected spikes based on their extracted features, aiming to identify their neuronal origins. Clustering approaches in spike sorting can be classified into model-based and non-model-based methods. Model-based techniques rely on probabilistic frameworks to estimate spike distributions, providing precise classification but requiring predefined assumptions about data distribution. In contrast, non-model-based approaches, such as density-based clustering, offer greater flexibility and scalability without relying on predefined probability distributions. Hybrid methods integrate both approaches, dynamically refining clustering results to improve classification accuracy [49]. Advanced algorithms such as Kilosort and MountainSort employ sophisticated techniques like template matching and density-based clustering to enhance spike sorting efficiency. Kilosort, for example, iteratively refines neuron assignments using a probabilistic model, while MountainSort groups spikes based on local density variations. Once spike sorting is complete, the channel assignment helps determine neuron locations within the MEAs, allowing for spatial mapping of neural activity in brain organoids. If a spike cluster appears on a single channel, the neuron is likely positioned near that electrode, whereas spikes detected on multiple electrodes may indicate a spatially extended neuron or signal spread. During long-term recordings, researchers can track critical neural activity metrics, such as spike rate and interspike interval (ISI), providing insights into how neural dynamics evolve over time across different spatial regions of the MEAs [50]. To further analyze neural signals, the Power Spectral Density (PSD) is estimated using SciPy's Welch method, revealing the frequency characteristics of LFP [51]. These analytical steps ensure a detailed examination of spatiotemporal neural activity, which is essential for understanding functional neural circuits in brain organoids.

Neuronal activity recorded from MEAs exhibits both temporal and spatial correlations, which are fundamental for functional connectivity mapping and studying brain-like network behavior [52]. However, quantifying these correlations is difficult due to the asynchronous nature of neuronal firing and the inherently sparse nature of spikes compared to high sampling rates. Traditional approaches, such as Pearson's correlation coefficient, are deficient because they ignore idle periods and fail to capture the short-timescale correlations required for the accurate analyses. While the correlation index is commonly used, it is also highly influenced by firing

rates, resulting in inaccurate comparisons. In contrast, the Spike Time Tiling Coefficient (STTC) provides a more reliable measurement by considering both spike timing and firing patterns [53]. STTC assesses correlations between a pair of spike trains by determining whether spikes in one train occur within a time range ( $\pm\Delta t$ ) of spikes in the other train. It calculates the proportion of spikes from a single train that meets this circumstance and compares it to the expected proportion based on random chance. A higher-than-expected number of spikes within this interval implies a positive correlation, whereas fewer reflect a negative correlation. This approach prevents double-counting overlapping time windows, which improves its sensitivity to spike train patterns [54].

To visualize functional connectivity, researchers construct pairwise correlation maps using STTC, mapping each neuron's spatial position to its corresponding recording electrodes. Some connections are excluded based on the distribution of spike time delays (multi-peaked or broad distribution). To visualize functional connectivity, each neuron (single unit) is represented as a node, while the strength of correlation between neuron pairs is represented as an edge. The thickness of the edge is determined by the STTC scores. In addition, the direction of information flow can be determined based on the average spike time latency. A negative mean spike time latency relative to a reference unit shows that the direction is toward the reference unit, whereas a positive latency indicates the reverse. Nodes are then classed as receivers, senders, or brokers depending on their incoming and outgoing connections (in-out degrees). To determine the importance of the detected "sender" and "receiver" nodes, the network is compared to randomized networks [55].

Several computational tools have been developed to streamline the process of neural circuit mapping and functional connectivity analysis in neuromorphic studies. SpikeInterface is an open-source Python framework that standardizes spike sorting workflows, integrating multiple spike sorting algorithms while supporting diverse data formats. It simplifies preprocessing, sorting, and post-processing, enhancing reproducibility and scalability in neural data analysis [55]. Another tool, NeuroRighter, is an open-source, real-time electrophysiology platform that supports up to 64 channels for simultaneous recording and electrical stimulation. Designed for both *in vitro* and *in vivo* experiments, NeuroRighter features a structured spike detection pipeline, including threshold-based detection, waveform validation, and online spike sorting via Gaussian mixture models. It also facilitates functional connectivity visualization using heat maps, node-link diagrams, and hierarchical clustering methods to construct correlation matrices and analyze neural interactions. The platform complemented by a flexible stimulation subsystem, low-latency data servers, and an API for custom plugin development facilitates a

wide range of customized experimental paradigms by allowing users to easily configure multichannel recordings and implement closed-loop control based on neural activity. This flexibility makes NeuroRighter an efficient platform for real-time closed-loop neuromorphic experiments [56].

Another powerful tool, MEA-NAP, is a comprehensive network analysis pipeline tailored for functional connectivity studies in neuronal 2D and 3D organoids using MEAs. The platform automates pre-processing, spike detection, and connectivity analysis, employing multi-unit threshold-based and template-based detection methods. Functional connectivity is quantified using cross-correlation and transfer entropy, which assesses temporal dependencies and information flow between neurons. MEA-NAP further employs graph-based techniques to construct network representations, offering visualization tools such as adjacency matrices, node-link diagrams, and heat maps, where node size and edge thickness represent connectivity strength. Additionally, the platform provides network topology analysis, incorporating metrics like degree centrality and clustering coefficients to identify key hubs and modular structures within neural networks. This comprehensive pipeline enables researchers to investigate network-level effects of pharmacological interventions and disease-causing mutations, making it a valuable translational tool for mechanistic studies and drug screening applications [45]. By integrating real-time spike sorting, functional connectivity mapping, and neural activity visualization, the platform will enable a deeper understanding of brain-like network dynamics, paving the way for innovations in neuromorphic engineering and neuroinformatics.

## 4.2 Concept Generation

### 4.2.1 Brain Organoid Generation

#### 4.2.1.1 hiPSCs Culturing Materials and Reagents

- Healthy Control Human iPSC Line, Male, SCTi004-A

SCTi004-A hiPSCs are reprogrammed from Peripheral Blood Mononuclear Cells (PBMCs) of a 23-year-old male African American donor using ReproRNA™-OKSGM, a non-integrating reprogramming technology. The cell line had undergone extensive quality control procedures to ensure quality and reproducibility including assessment of genomic integrity and stability, cell line identity, microbiological sterility, and importantly pluripotency. STEMdiff™ Trilineage Differentiation Kit and flow cytometry were used to demonstrate trilineage differentiation capacity of the cells into ectoderm, mesoderm, and endoderm. ScTi004-A complies with the guidelines of The International Society for Stem Cell Research (ISSCR) and also meets the regulatory requirements for academic use of hiPSCs collected using Institutional Review Board (IRB) protocols. Therefore, the SCTi004-A cell line is suitable for a multitude of stem cell research applications, including 2D multiple cells differentiations, and organoid models [57].

Donor Information		SCTi004-A
Age <sup>1</sup>	23	
Sex <sup>2</sup>	Male	
Ethnicity and/or Race <sup>1</sup>	African American	
Ancestry <sup>2</sup>	100% African 0% European	0% East Asian 0% South Asian
Diagnosis <sup>1</sup>	Clinically unaffected at donation	
Height <sup>2</sup>	165 cm	
Weight <sup>2</sup>	64.0 kg	
BMI <sup>2</sup>	23.5 kg/m <sup>2</sup>	
Blood Type <sup>2</sup>	B+	
Tobacco Use <sup>1</sup>	Non-smoker	
HLA Haplotype <sup>2</sup>	HLA Class I: A*34:02:01G, - B*44:03:02G, 52:01:02G C*07:01:01G, 16:01:01G	HLA Class II: DRB1*13:01:01G, 13:03:01G DRB3*01:01:02G, 02:02:01G DRB4*, - DRB5*, - DQB1*02:01:01G, 05:01:01G DPB1*01:01:01G, 04:02:01G



Figure 6 SCTi004-A Donor Information (Left) and SCTi004-A (Right)

- mTeSR<sup>TM</sup> Plus

mTeSR<sup>TM</sup> Plus is a stabilized, serum-free cell culture medium based on Dr. James Thomson laboratory [58]. for feeder-free maintenance and expansion of embryonic and induced pluripotent stem cells. It comprises of mTeSR<sup>TM</sup> Plus Basal Medium and mTeSR<sup>TM</sup> Plus 5X Supplement. The media is the pH buffering enhanced and Fibroblast Growth Factor 2 (FPF2) stabilized version of mTeSR<sup>TM</sup> 1, this allows alternate feeding schedules, superior culture morphology, and cell growth characteristics of hiPSCs [59].



Figure 7 mTeSR™ Plus

- Y-27632 (Dihydrochloride)

Y-27632 or RHO/ROCK pathway inhibitor is a highly potent, selective, and cell-permeable inhibitor of Rho-associated coiled-coil containing kinase (ROCK). It targets both ROCK1 and ROCK2 by competing with ATP for binding at the catalytic site. Primarily, ROCK inhibitor is used to enhance cell adhesion through cell migration and prevention of cell blebbing. This happens by suppressing actin filament contraction and microtubule bundling resulting in an increase in survival rate and preventing dissociation-induced apoptosis or anoikis of hiPSCs [60]. Additionally, Y-27632 also plays crucial roles in improving cryopreserved cell recovery and promoting embryoid body formation which is essential for organoid formation [61].



Figure 8 Y-27632

- Dulbecco's phosphate-buffered saline (D-PBS)

D-PBS are used for diluting, irrigating, washing, and transporting solutions for cell and tissue culture. It maintains physiological pH and osmotic balance of the culturing medium while providing cells with sources of water and essential inorganic ions [62].



Figure 9 D-PBS

- ReLeSR™

ReLeSR™ is an enzyme-free reagent designed for dissociation and passaging of hiPSCs as aggregates. It simplifies passaging protocols by eliminating the need for scraping differentiated cells. Unlike Ethylenediaminetetraacetic acid (EDTA) which dissociates all cells, ReLeSR™ selectively detaches undifferentiated cells from cultureware, leaving differentiated cell behinds, resulting in higher quality hiPSCs [63].



Figure 10 ReLeSRTM

- DMEM/F-12 with 15 mM HEPES

DMEM/F-12 with 15 mM HEPES is an incomplete medium used for cell culture applications. It is pre-screened for use with other reagents for the maintenance of undifferentiated cells. In hiPSCs culturing, it is used as a cost-effective alternative serving as a basal medium for centrifugation steps [64].



Figure 11 DMEM/F-12 with 15 mM HEPES

- CryoStor® CS10

CryoStor® CS10 is a ready-to-use cryopreservation medium containing 10% dimethyl sulfoxide (DMSO), it is designed for preserving cells during freezing at -70°C to -196°C. The medium provides a safe environment for cells during thawing process, maximizing cell recovery and viability after cryopreservation [65].



Figure 12 CryoStor® CS10

#### 4.2.1.2 Cerebral Organoid Culturing Materials and Reagents

- STEMdiff™ Cerebral Organoid Kit and Maturation Kit

STEMdiff™ Cerebral Organoid Kit comprises of 5 components which are STEMdiff™ Cerebral Organoid Basal Medium 1, Basal Medium 2, Supplement A\*, Supplement B\*, Supplement C\*, Supplement D\*, and Supplement E\*. These components function together as a serum-free culture medium based on Lancaster & Knoblich protocol [66, 67, 68]. that allows generation of hiPSCs-derived unguided cerebral organoids. Following a four-stage protocol, the kit induces the organoid to exhibit cortical-like features including the ventricular zone, outer subventricular zone, intermediate zone, and cortical plate. The layers are oriented in accurate cytoarchitecture manner resemble to that of developing human brain. In SNNs modeling, an advanced non-random neuronal circuitry is preferred, therefore sufficient maturation time is required for the organoid to exhibits more complex structure that allows firing and inhibitory functions. STEMdiff™ Cerebral Organoid Maturation Kit consists of STEMdiff™ Cerebral Organoid Basal Medium 2 and Supplement E allows culturing of the generated organoid for an extended period of more than 40 days to ensure more intricate structure of cerebral organoid [69].



Figure 13 STEMdiff™ Cerebral Organoid Kit

- Anti-Adherence Rinsing Solution

Anti-Adherence Rinsing Solution is a surfactant solution that plays crucial roles for suspension culture like cerebral organoids. It is designed for pre-treatment of cultureware, such as plates, flasks, and pipettes to reduce surface tension. This prevents cell adhesion which could cause damage to the structure of cerebral organoid [70].



*Figure 14 Anti-Adherence Rinsing Solution*

- Organoid Embedding Sheet

The Organoid Embedding Sheet is a specialized tool for embedding 3D cell aggregates, in this case, organoids, into Matrigel for the expansion process. The wells are designed to fit organoids with a diameter size up to 5 mm. It is easier to handle during procedures when compared to Parafilm® embedding method [71].



*Figure 15 Organoid Embedding Sheet*

- 6-Well Ultra-Low Adherent Plates for Suspension Culture

Ultra-Low Adherent Plates are specialized cultureware designed for suspension culture, it is suited for growing non-adherent cell aggregates like organoids. These plates are made from sterile polystyrene with a flat bottom coated with a covalent hydrogel layer to prevent cellular attachment. The biologically inert, non-toxic, and non-degradable

surface property of the plate minimizes protein adsorption, enzyme activation, and cellular activation in a multiwell plate format [72].



Figure 16 6-Well Ultra-Low Adherent Plates

- Gentle Cell Dissociation Reagent

Gentle Cell Dissociation Reagent is an enzyme-free used for dissociation and passaging hiPSCs as aggregates. In this case, it is used for organoid formation passage to avoid genetic abnormalities during embryoid body generation [73, 74].



Figure 17 Gentle Cell Dissociation Reagent

- Corning® Matrigel® hESC-Qualified Matrix, LDEV-free

Corning® Matrigel® hESC-Qualified Matrix is a soluble basement membrane extract derived from the Engelbreth-Holm-Swarm tumor. The gel polymerizes at room temperature, constituting basement membrane. Its major components include laminin, collagen IV, entactin, heparin sulfate proteoglycan, collagenases, plasminogen activators, and others. When cultured with a compatible culturing medium such as mTeSR<sup>TM</sup>, Matrigel acts as a substrate for hiPSCs and organoids, supporting feeder-free expansion

of the cells. Cells maintained in mTeSR™ with Matrigel express high pluripotency while eliminating the need for additional growth factors [75].



*Figure 18 Corning® MatriGel® hESC-Qualified Matrix*

*Table 1 Additional materials and reagents required for brain organoid generation*

Materials and Reagents Required	
Catalog Number	Description
351029	Falcon® 100 mm Dish, Non-Treated
TF-205-WB-R-S	Axygen™ 200 µL Wide-Bore Universal Pipette Tips
7007	Corning® 96-well Round Bottom Ultra-Low Attachment Microplate
353226	Falcon® 24-well Flat Bottom, Tissue Culture-Treated
3473	Costar® 24-well Ultra-Low Attachment Plate
352098	Falcon® Conical Tubes, 50 ml
357543	Falcon® Serological Pipettes, 5 ml
357551	Falcon® Serological Pipettes, 10 ml
100-1181	Hausser Scientific™ Bright-Line Hemocytometer
07050	Tryphan Blue

*Table 2 Equipment required for brain organoid generation*

Equipment Required
Biohazard safety cabinet certified for Level II handling of biological materials
Incubator with humidity and gas control to maintain 37°C and 95% humidity in an atmosphere
Low-speed centrifuge with a swinging bucket rotor
Pipette-Aid with appropriate serological pipettes
Pipettor with appropriate tips
Inverted microscope with a total magnification of 20X to 100X
Isopropanol freezing container
-150°C freezer or liquid nitrogen (LN <sub>2</sub> ) vapor tank
-80°C freezer
-20°C freezer
Refrigerator (2-8°C)
Sterile forceps
Orbital shaker with sticky mat

#### **4.2.2 Microelectrode Arrays System**

##### **4.2.2.1 Microelectrode Arrays Printed Circuit Board**

MEAs is a non-invasive and high-speed technique for extracellular potential recording or stimulating the brain organoid offering a balance between temporal resolution and spatial resolution. Microelectrode arrays utilize a polyimide-based flexible PCB (fPCB) as base material, ensuring biocompatibility while preserving high signal integrity and reducing electrical noises. The exposed electrodes are coated with Electroless Nickel Immersion Gold (ENIG) facilitating electrical conductivity and protection against corrosion and oxidation. Electrode arrays contain 8 electrodes arranged in square grid-like pattern with 1.5 mm center to center spacing in between each electrode with empty center. Due to the size of the organoid varying between 3 to 5 mm, the square pattern with 3 mm would cover the organoid surface allowing a systematic recording with wide spatial resolution while preventing crosstalk between the conductive elements. Additionally, reference electrode is placed further from the electrode array grid ensuring the reference electrode does not touch the organoid. On top of MEAs, 7 mm diameter Borosilicate ring serves as a well for Ringer's solution and as an organoid placement on

the MEA due to its biocompatibility. The Ringer's solution will connect the organoid to ground and reference of the system by the reference electrode. As the MEA is printed on the fPCB, the connection to the recording system must use the flexible printed circuit connector or FPC connector, a 10 pins gold finger with 0.5 mm pitch along with stiffener is used to create a connection to other components via Hirose FH12A-10S-0.5SH(55) FPC connector on the interconnect board, acting as an adaptor between the MEAs and the recording system.

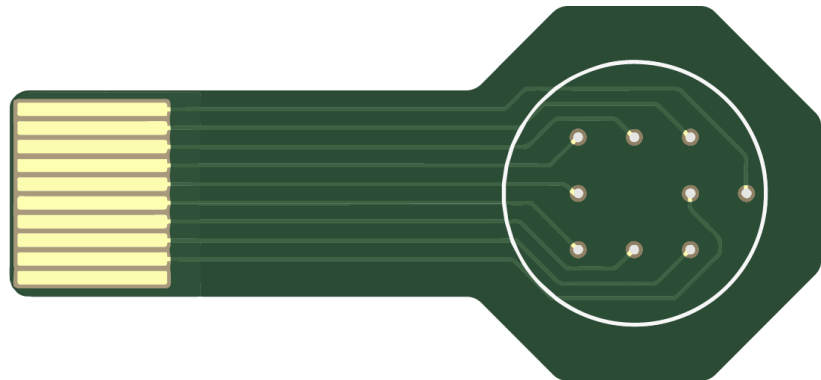


*Figure 19 Flexible Micro electrode array PCB*

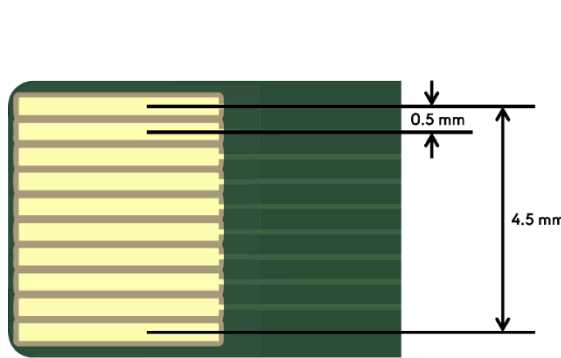


*Figure 20 Gold finger connecting pins*

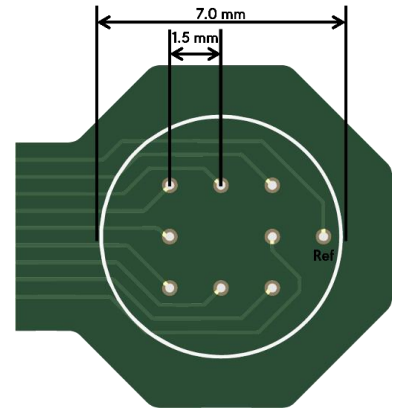


*Figure 21 MEA grid pattern*

#### 4.2.2.2 Interconnect board

The standard connection of Intan recording system uses 18-pin Omnetics connector as an input, Interconnect board is used an adaptor for connecting a flexible microelectrode array to a recording system where it maps the electrode channels to the target system using two connectors. Connecting to the MEAs, Hirose FH12A-10S-0.5SH(55), a top contact, 10 pins, single alignment 0.5 mm pitch, horizontal mounting,

plated with gold is used for its sufficient pins, top connection and small pitch. By inserting gold finger to the connector, it can securely transmit the electrical signal from the electrode to the interconnect board. After that, the interconnect board route each connection pin to the Omnetics connector A79017-001, an 18-position receptacle connector resulting in a connection mapped from the electrode to the Omnetics connector which connects to the recording system for further processing.

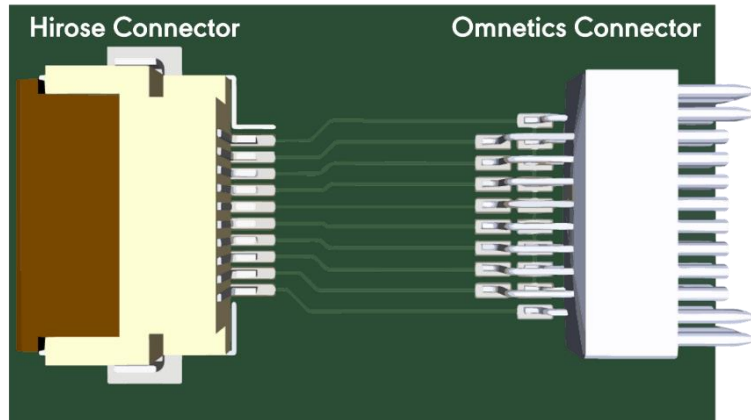


*Figure 22 Interconnect board top view*

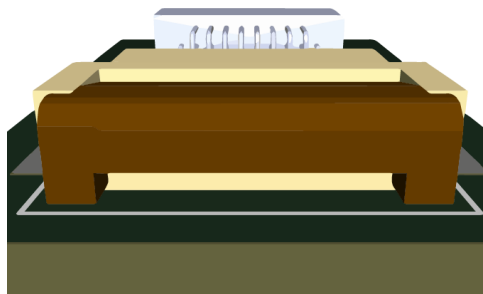


*Figure 23 Hirose Connector*

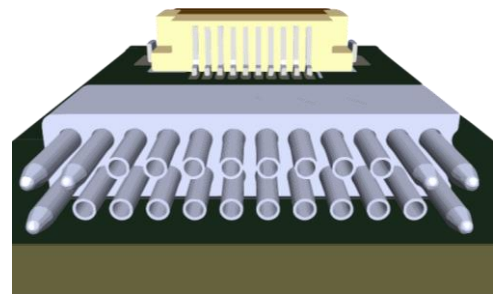


*Figure 24 Omnetics connector*

#### 4.2.2.3 BCI Lab's System in Package

Since the electrophysiology data from brain organoids has a wide range of frequency bands in microvolt scale, a high-resolution data acquisition system is crucial to acquire high quality electrophysiology data. Thus, our project aims to develop a novel interface system for electrophysiology data acquisition and processing. The BCI Lab's SiP has been selected to be the core controller of our data acquisition system. BCI Lab's SiP mainly consists of 8-Channel Analog Front-End (ADS 1298) and BlueNRG-LP. ADS1298 provides eight channels to measure data with right leg driven amplifiers and 24-bit ADC for biosignal digitization. Moreover, its specification offers a high input

impedance and high dynamic range to capture biosignals in microvolt scale with sampling rate up to 32,000 samples/second. With extensive specifications, ADS1298 becomes a highly potential component to measure brain organoid's electrophysiology data. After acquiring data from brain organoids, BlueNRG-LP in BCI Lab's SiP is accountable for electrophysiological data receive and transmission. While having the highest efficiency of power consumption, the component is programmed to serve as a management unit that offers varieties of communication protocols and General-Purpose Input/Outputs (GPIOs) pins to manage the input and output. The transmitted biosignals will be further processed on the recording system on the computer.

The recorder system in the computer consists of multiple parts including data acquisition, signal filter, interface, and data saving module. The data acquisition module serves as an initial point of contact for raw data stream, received from BlueNRG-LP via Universal Asynchronous Receiver-Transmitter (UART) protocol. Once raw data is acquired, the signal filter module will refine raw data by filtering to isolate frequency range of 0.25 Hz to 3000 Hz and suppress 50 Hz noise, ensuring clean and accurate signal. After the data has been cleaned, it will be shown on interface module where it is responsible for visual representation of raw data to provide real-time insight of the data stream for identifying system's performance and potential anomalies. Lastly, the data saving module will save filtered data for future analysis and processing. HDF5 file format is used as a medium as it offers efficient storage, easy data access, and compatibility by various data analysis tools.

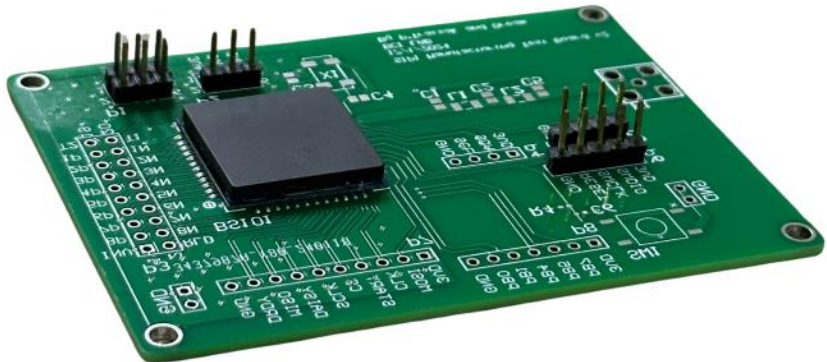


Figure 25 BCI Lab's System in Package

#### 4.2.2.4 RHS Stim/Recording System

Since our project aims to develop a novel acquisition system, implementing a robust validation system is essential for ensuring its accuracy and precision. Therefore, a 16-channel RHS stim/recording system from *Intan Technologies*, considered as the gold standard of miniature electrophysiological equipment, is opted for biosignals acquisition and processing. The system is constructed by three main components which are 16-Channel RHS Stim/Recording Headstage, RHS Stim/Recording Controller, and are coupled by Stim SPI interface cable. The 16-Channel RHS Stim/Recording Headstage functions as a high performance analog front end for electrophysiology acquisition, providing amplification with adjustable filtering of biosignal from 0.1 Hz up to 20 kHz, along with biosignal digitization with an ADC of 16-bit resolution. With this headstage, the acquired biosignals are amplified, filtered, and digitized. The biosignals are then recorded and transmitted to the computer by the RHS Stim/Recording Controller. Subsequently, the recorded biosignal will be presented in real time, graphically illustrated, with spike detection on a user-friendly interface by RHX Data Acquisition Software on the computer.



Figure 26 RHS stim/recording system

#### 4.2.3 Organoid Intelligence Platform

One of the approaches to overcome the von Neumann bottleneck is the OI platform, which utilizes the biological tissue of the cerebral organoid as a computational and storage center. In the experiment, the MEAs serve as a primary interface between an organoid and an external computational system, allowing both stimulation and recording of neural activity.

#### **4.2.4.1 Training Process and Adaptive Learning Mechanisms**

In this study, we aim to develop an adaptive framework for OI by designing a training system that facilitates neural reorganization through repeated stimulation input, like training unsupervised machine learning. The training process begins with a benchmarking phase to establish baseline neural activity and optimize stimulation parameters, ensuring effective classification accuracy. This initial step is critical for standardizing experimental conditions and providing a reference for evaluating neural adaptations. Following the benchmarking phase, we expose the naive organoid to repeated sensory stimulation with bipolar electrical pulses over 2 days, with each training epoch occurring every 12 hours. During this process, neural responses are captured as spatiotemporal activity patterns, including raster plots and spike firing rates. These patterns are then analyzed using a decoding model to classify directional movements (left or right). To evaluate the organoid's learning progress, performance metrics, including accuracy and confusion matrices, are compared before and after training. Improvements in these metrics will indicate neural adaptation, demonstrating the organoid's capacity for dynamic learning. Additionally, functional connectivity changes are continuously monitored throughout the training process to further assess the organoid's efficiency in information processing and validate the observed performance improvements.

#### **4.2.4.2 Integration into a Virtual Gameplay Environment**

To demonstrate the real-time learning capabilities of OI and highlight its functional similarities to artificial intelligence, we employ a virtual Pong game as an interactive framework. In this set up, key game events, such as the ball's position, are converted into spatiotemporal sequences of bipolar electrical pulses that stimulate the organoid, inducing neural activity. The resulting neural responses are then classified and mapped to predefined motor regions, allowing the organoid to control the movement of a virtual paddle. A reinforcement feedback mechanism is implemented to guide learning. When the organoid generates correct paddle movements, it receives consistent and predictable stimulation, reinforcing the desired behavior. Conversely, incorrect responses result in unpredictable or absent feedback, prompting adaptive refinement of the organoid. Through iterative reinforcement, the organoid will refine its decision-making processes and improve paddle control performance over time.

#### **4.2.4 Neuromorphic Computation**

##### **4.2.4.1 Spike Sorting**

Spike sorting is essential in neuromorphic computing as it enables the identification and categorization of neuron-like events, or "spikes," from extracellular recordings collected across multiple channels. This process aims to attribute each detected spike to a specific neuron or a single neuronal unit by clustering similar spike waveforms. For this project, the Python-based framework SpikeInterface was selected as it integrates multiple algorithms and tools into a unified approach, enhancing consistency and accuracy in neural data analysis. Unlike using standalone clustering algorithms such as K-means, PCA, and Gaussian mixture models (GMMs), SpikeInterface standardizes preprocessing, parameter optimization, and evaluation, reducing compatibility issues and enhancing reproducibility—making it ideal for direct and accurate comparisons and benchmarking across datasets.

Initially, raw extracellular voltage data from the MEAs system is converted to HDF5 format. Using MATLAB's MEAs ToolBox software, a bandpass filter is applied to the data, followed by spike detection. The baseline noise level in the signal is determined by analyzing "spike-free" periods and fitting Gaussian distributions to 50-ms windows of data. Instead of relying on strict standard deviation thresholds, MEA-ToolBox uses the median noise level across channels, establishing a detection threshold at five times the RMS noise level.

With SpikeInterface, multichannel data undergoes preprocessing steps, including noise removal and frequency filtering (typically between 300 Hz and 3 kHz) to enhance relevant neural signals. SpikeInterface's SpikeToolkit package provides built-in functions for filtering and normalizing neural data, creating a reliable foundation for further analysis. After preprocessing, various spike sorting algorithms, such as Kilosort, Spyking Circus, and HDSort inside SpikeSorters package are used to help categorize spikes into neuron-specific groups based on waveform similarities. This classification process is crucial for identifying neuron-specific patterns in SNNs. The framework also includes post-processing capabilities, using the SpikeWidgets package for data curation, visualization, and validation of sorted spikes, ensuring high quality in spike identification. Finally, the SpikeComparison package allows for standardization and benchmarking of results, enhancing reproducibility and facilitating comparisons across

studies. SpikeInterface thus serves as an efficient and reliable tool for building robust spike sorting pipelines, essential for advancing neuromorphic computing applications.

#### 4.2.4.2 Spatiotemporal Mapping

Spatiotemporal mapping involves encoding and interpreting data in a manner that reflects the timing and spatial location of neural spikes, which is essential for understanding and visualizing network dynamics in real-time. By translating raw neural data into interpretable patterns, this mapping enables neuromorphic systems to understand complex spatial and temporal relationships between neurons. In practice, spatiotemporal mapping is achieved by pairing spike events with specific neuron coordinates derived from electrode positions and timestamps of each spike. This data is then organized into a multidimensional map, where each neuron is represented in its relative spatial position, and each spike is marked by its temporal occurrence. Neuromorphic hardware then uses this map to replicate neural-like connectivity by forming synaptic connections between neurons that are both spatially and temporally correlated. Such mappings are particularly important in SNNs where neurons are connected based on the likelihood of co-activation within a certain spatial and temporal window, closely mimicking biological neural networks.

#### 4.2.4.3 Spike Time Latency Distribution

Spike time latency distribution is used to model the delays between an external stimulus and the subsequent action potentials (spikes) generated by neurons. These latencies are determined by the unique response characteristics of each neuron and the dynamics of synaptic interactions within the network. To visualize this distribution using MATLAB, spike times are recorded in response to a stimulus using MEAs. The latency for each spike is calculated by measuring the time difference between the stimulus onset and the spike occurrence. For repeated stimuli, latency data from each trial are calculated independently, capturing variations across trials. The combined dataset provides a comprehensive view of response timing and plotting it as a histogram reveals neural response consistency and timing dynamics.

By examining the distribution of these latencies, insights into the timing relationships between pairs of neurons can be revealed, which is essential for understanding functional connectivity and the direction of information flow within the

network. To validate the latency distribution of signals from brain organoids, certain characteristics should be evident in the latency patterns. These include:

1. In brain organoid networks with spontaneous activity, short latency values, typically around 5 ms, are expected. These brief latencies reflect rapid signaling between neurons, a hallmark of active neural connections.
2. Due to the diversity of neuron types and synaptic strengths in organoids, a broad distribution of spike time latencies often exists. As an organoid matures, the latency distribution may become more refined, reflecting increasingly synchronized activity patterns. This can suggest the development of more organized functional networks.
3. A unimodal latency distribution, where most latencies cluster around a single peak, can indicate consistency in neural responses to a specific stimulus. This consistency is critical for reliable information processing and transmission, as it suggests that spikes are primarily the result of genuine neural responses rather than random or noisy events.

#### 4.2.4.4 Pairwise Spike Time Correlation Mapping

Pairwise spike time correlation mapping is a technique used to examine the synchronicity and timing correlation between pairs of neurons, which is essential for simulating neural synchrony in SNNs. By analyzing the temporal relationships between neuronal spikes, this method enables neuromorphic systems to detect patterns that resemble biological neural activity, which is crucial for adaptive processing. In this approach, the STTC is selected as the primary metric for quantifying the degree of correlation between neural spike trains. Unlike traditional measures, STTC offers specific benefits such as symmetry, independence from firing rates, robustness to data amount, and insensitivity to minor timing variations, making it suitable for analyzing neural synchrony across different conditions. To create a functional connectivity map using STTC, spike trains are analyzed within a designated time window (e.g.,  $\Delta t = 20$  ms) to calculate connectivity strengths between neuron pairs. A MATLAB script calculates STTC scores following the STTC formula as shown in equation (17).

$$STTC = \frac{1}{2} \left( \frac{P_A - T_B}{1 - P_A T_B} + \frac{P_B - T_A}{1 - P_B T_A} \right) \quad (17)$$

Where  $T_A$ ,  $T_B$  = The proportion of the total recording time within  $\Delta t$  of any spike from a given A and B train, respectively.  $P_A$ ,  $P_B$  = The proportion of spikes A and B that fall within  $\Delta t$  of a spike in another train.

Further filtering is applied based on spike time latency distributions to retain only meaningful connections. For instance, electrode pairs with multimodal latency distributions or excessive latency widths are excluded to reduce noise. A threshold, derived by computing STTC scores from randomized spike trains, is then applied to filter out weak connections, ensuring that only significant synchrony is represented. The final set of STTC values between neuron pairs is organized into a weighted adjacency matrix, serving as the connectivity data prepared for network connectivity visualization steps.

For visualization, nodes represent neurons or regions of interest, and edges indicate STTC-based connectivity strength. Weak connections and self-loops are removed, highlighting only significant connections in the network plot. Node sizes are scaled based on their degree (number of connections) to help identify hub-like nodes with significant influence within the network. Edge thickness and color intensity correspond to connection strength, with thicker and darker edges indicating stronger connections. To emphasize key structural links, the layout is arranged on an 8x8 grid that simulates the configuration of a MEAs. This setup helps visualize prominent functional connections among neurons, while legends for edge weights and node degrees facilitate interpretation of the network's connectivity structure.

Further analysis of the connectivity map provides insights into network structure by evaluating metrics like the sizes of the largest connected components, which reveals global connectivity patterns. Directionality can be added by examining spike time latencies, identifying nodes as "senders," "receivers," or "brokers" based on their in-degree and out-degree connections. Statistical validation is performed by comparing the connectivity metrics against randomized networks, while additional network properties, such as node strength distribution and edge density, provide further insights into the connectivity structure. A histogram and cumulative distribution plot of edge weights illustrate the distribution of connection strengths across the network, highlighting the prevalence of various connection intensities.

### **4.3 Concept Reduction**

Although OI offers an intriguing paradigm for biocomputing, it presents unresolved ethical, technical, and scalability challenges. The complexity of sustaining viable organoid systems for long-term, large-scale computation, coupled with limitations in reproducibility, bioelectronic interfacing, and ethical concerns surrounding tissue origin and potential consciousness, significantly hinders their practical application. In contrast, neuromorphic computation provides a more feasible and ethically sound alternative by emulating brain-like processing using artificial SNNs. This approach allows for precise, controllable modeling of neural dynamics without the complications of living tissue. Therefore, this study strategically eliminates the use of organoids as computational hardware and utilizes them as biological data sources to inform and refine neuromorphic architectures. This direction preserves the value of biological insight while enabling scalable, efficient, and ethically viable brain-inspired computing.

## CHAPTER V

### ANALYSIS AND EVALUATION OF DESIGN PROCESS

#### **5.1 Brain Organoid Generation and Characterization**

##### **5.1.1 Human Induced Pluripotent Stem Cells Culture**

In this study, hiPSCs were provided and cultured by Ramathibodi Hospital using the BYS0113 cell line, an ATCC commercial strain reprogrammed from bone marrow CD34+ cells of a 45-year-old Asian male. The culture was maintained under feeder-free conditions using mTeSR™ medium. The cells were routinely monitored to maintain a confluence of 70–80%, an optimal range for promoting proliferation while minimizing spontaneous differentiation. Morphological evaluation ensured the presence of healthy, compact colonies with a high nuclear-to-cytoplasmic ratio, and the differentiation levels were kept below 10%.



*Figure 27 hiPSCs for Brain Organoid Culture*

##### **5.1.2 Brain Organoid Culture**

Cerebral organoids were generated from hiPSCs using a modified version of the protocol of Lancaster & Knoblich and Lancaster et al (2013; 2014; 2017), in combination with the STEMdiff™ Cerebral Organoid Kit (STEMCELL Technologies). This unguided differentiation method recapitulates key stages of human cortical development, beginning with embryoid body formation, followed by neural induction and long-term maturation in a three-dimensional suspension culture. The protocol is optimized to support the self-organization of neuroepithelial tissues and the emergence of region-specific brain-like structures. All steps were performed

under sterile conditions, and organoid development was carefully monitored to ensure reproducibility and viability for subsequent electrophysiological and immunohistochemical analyses.

#### **5.1.2.1 Organoid Formation (Day 0–5)**

1. hiPSCs were cultured to 70–80% confluence with <10% spontaneous differentiation.
2. Colonies were dissociated using 0.5 mM EDTA diluted in 1x PBS and centrifuged at  $300 \times g$  for 5 minutes.
3. Cells were resuspended in Organoid Formation Medium containing 10  $\mu\text{M}$  Y-27632 and counted.

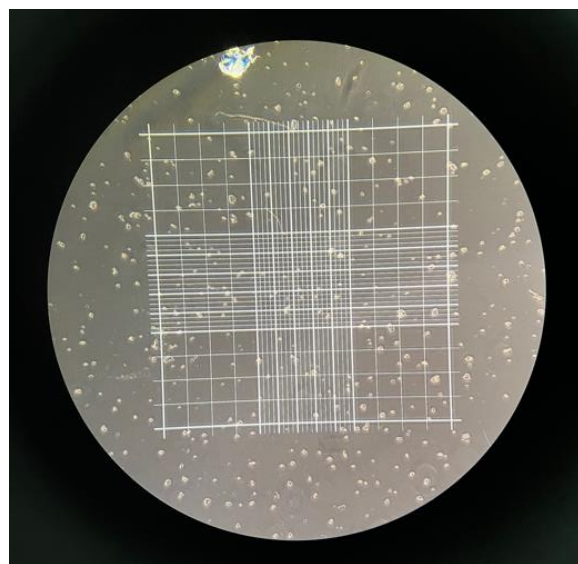


*Figure 28 Dissociated hiPSCs under a hemocytometer*

4. 9,000 cells were seeded per well in a 96-well round-bottom ultra-low attachment plate (Corning).
5. Plates were incubated at 37°C and left undisturbed for 24 hours.
6. On Days 2 and 4, 100  $\mu\text{L}$  of fresh Organoid Formation Medium was added to each well.
7. By Day 5, organoids reached 400–600  $\mu\text{m}$  diameter and were transferred to induction phase.



Figure 29 Embryoid Body

#### 5.1.2.2 Induction (Day 5–7)

1. Organoids were transferred to 24-well ultra-low attachment plates containing 0.5 mL Induction Medium per well.
2. Incubated at 37°C for 48 hours with regular monitoring.
3. Organoids developed smooth and translucent edges, indicating neuroepithelial initiation.



Figure 30 Brain Organoid Post-Induction

#### 5.1.2.3 Expansion (Day 7–10)

1. Matrigel was thawed on ice and kept chilled throughout embedding.

2. Organoids were transferred onto the Organoid Embedding Sheet and embedded with 15 µL Matrigel per organoid.



*Figure 31 Organoids Embedded using Matrigel*

3. Embedded organoids were polymerized at 37°C for 30 minutes.
4. Using Expansion Medium, organoids were washed into a 6-well ultra-low attachment plate and incubated for 3 days.

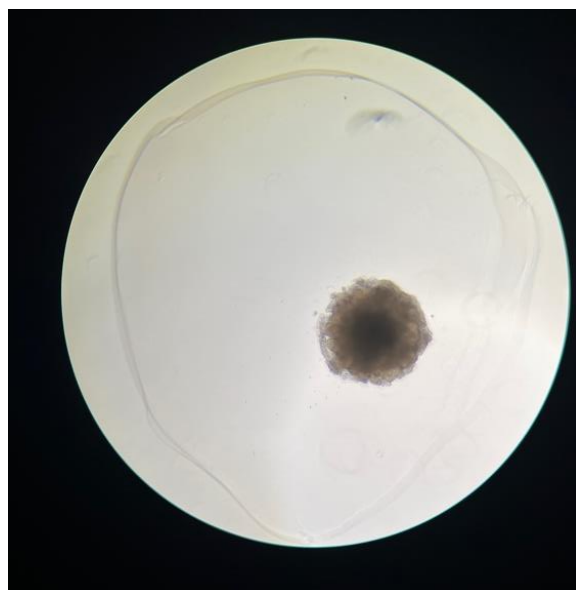


*Figure 32 Brain Organoid Post-Expansion*

#### **5.1.2.4 Maturation (Day 10–40+)**

1. Organoids were cultured in Maturation Medium on an orbital shaker at 80 RPM at 37°C.
2. Medium was changed every 1-2 days.

3. By Day 40, organoids showed neuroepithelial expansion and cortical-like structures and were ready for downstream applications such as immunohistochemistry and electrophysiology.

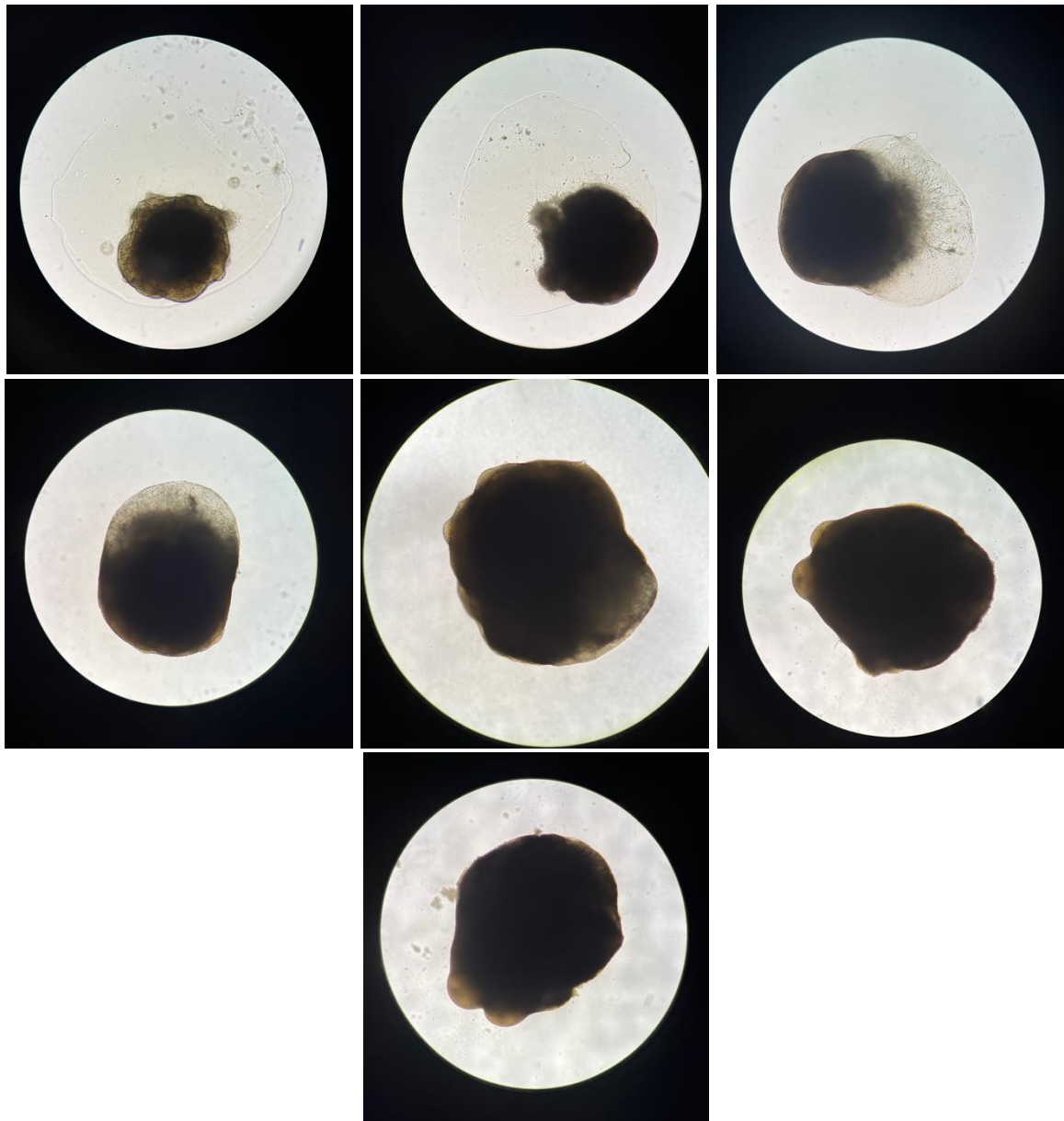


Figure 33 Day 18, 20, 25, 30, 35, 40, 42 Brain Organoid Respectively

### 5.1.3 Immunohistochemical Staining

Immunohistochemical staining was performed on cryosectioned cerebral organoids at Day 35 and Day 42 to evaluate neurogenesis and synaptogenesis during organoid maturation. The following steps were performed:

1. Cryosectioned tissue slices (10 µm thickness), stored at -80 °C, were allowed to air dry for 30 minutes at room temperature on a clean paper towel.
2. A hydrophobic barrier was created around each tissue section to contain reagents.



*Figure 34 Hydrophobic barrier surrounds tissue sections*

3. Tissue sections were rehydrated with 1x PBS. Care was taken to avoid dropping reagents directly onto the tissue to preserve morphology.
4. Sections were dried and permeabilized with 0.3% Triton X-100 in PBS for 10 minutes.
5. After gentle washing with PBS, the tissue was dried and blocked with 2% bovine serum albumin (BSA) in PBS for 60 minutes at room temperature.
6. Following blocking, primary antibodies diluted 1:200 in blocking solution were applied to each section. The antibody panel included:
  - **PAX6** (neuroprogenitor marker)
  - **MAP2** (neuronal dendritic marker)
  - **Synaptophysin (SYP)** (presynaptic marker)
  - **PSD95** (postsynaptic marker)

Sections were incubated with primary antibodies for 60 minutes at room temperature.

7. After rinsing, secondary antibodies diluted 1:400 in blocking solution were applied:
  - **Rb555** (binds rabbit host antibodies for PAX6 and PSD95)
  - **M488** (binds mouse host antibodies for MAP2 and SYN)

Incubation was performed for 60 minutes at room temperature.

8. Finally, the tissue was counterstained with antifade mounting medium containing DAPI and mounted with coverslips. Stained slides were imaged using a Zeiss LSM 900 confocal microscope equipped with Airyscan 2.

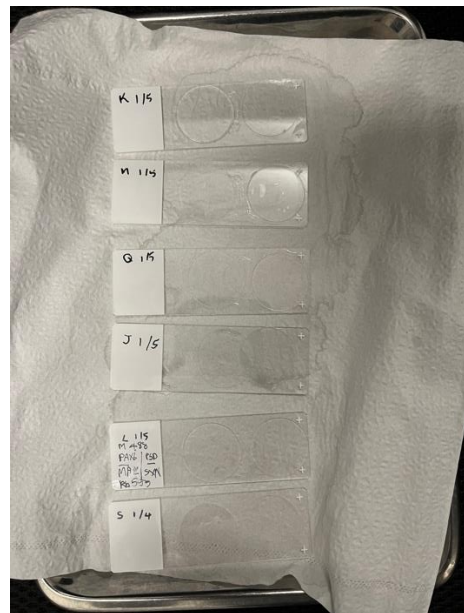


Figure 35 Mounted IHC samples

Fluorescence imaging revealed a progressive increase in the expression of both neuronal and synaptic markers over time. At Day 35, organoids exhibited moderate expression of PAX6, indicating the presence of neural progenitor cells, while MAP2 staining showed early neuronal differentiation, primarily localized in the outer regions of the tissue. The outward differentiation morphology confirms that the brain organoid resembles a fetal human brain.

By Day 42, there was a notable upregulation of MAP2 and PAX6, suggesting ongoing neuronal differentiation and progenitor proliferation. In addition, expression of synaptophysin (SYP) and PSD95, markers of pre- and post-synaptic structures, respectively, show colocalization supporting the formation of functional synaptic networks. Overall, the staining results confirm that the cerebral organoids underwent progressive maturation, with increasing neuronal complexity and synaptic development from Day 35 to Day 42. These findings support the electrophysiological data indicating functional neural connectivity at later stages.

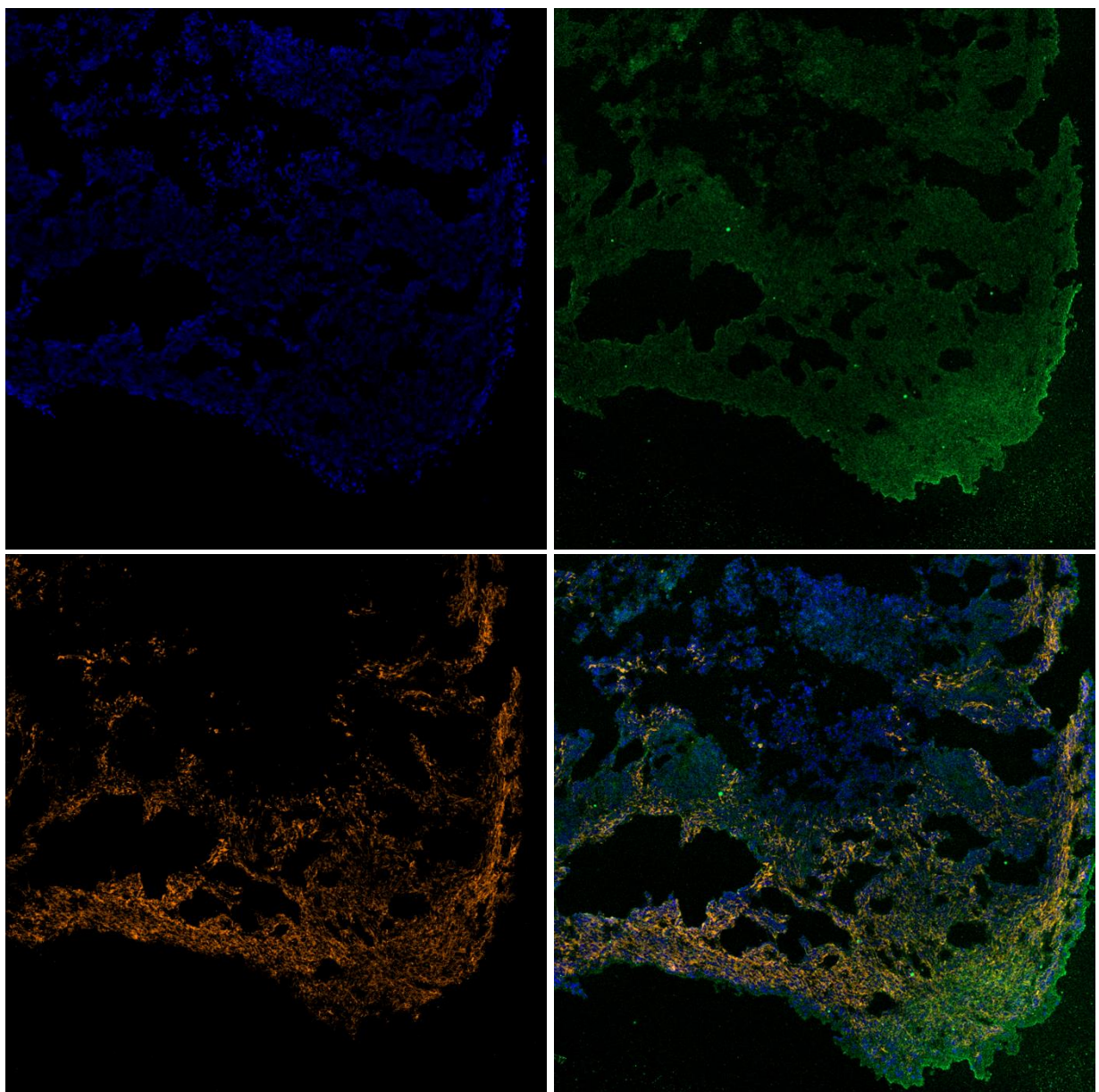


Figure 36 DAPI (Top Left), PAX6 (Top right), MAP2 (Bottom left), and Merged (Bottom right) Immunostaining of Day 35 Brain Organoid

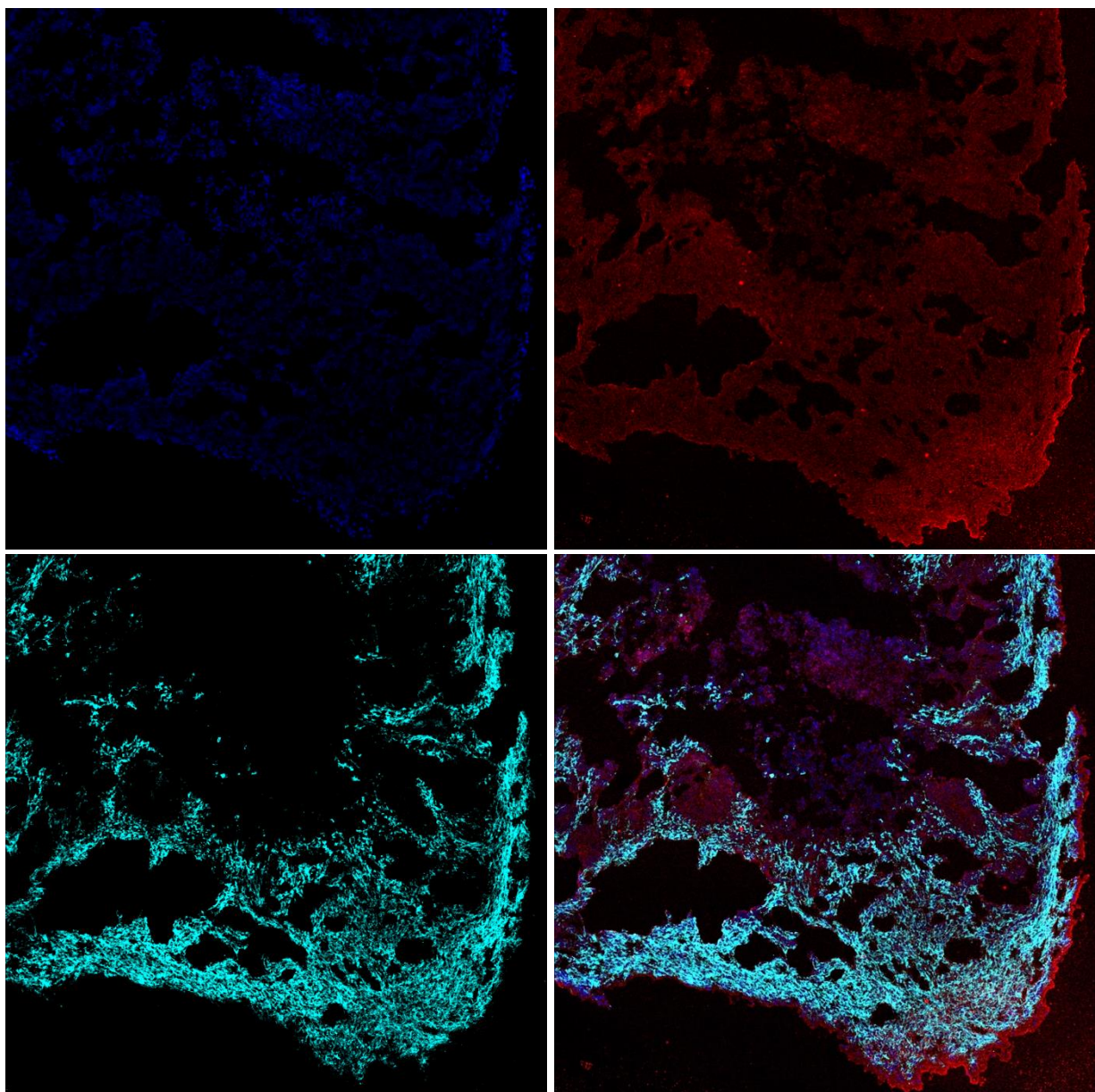


Figure 37 DAPI (Top Left), PSD95 (Top right), SYN (Bottom left), and Merged (Bottom right) Immunostaining of Day 35 Brain Organoid

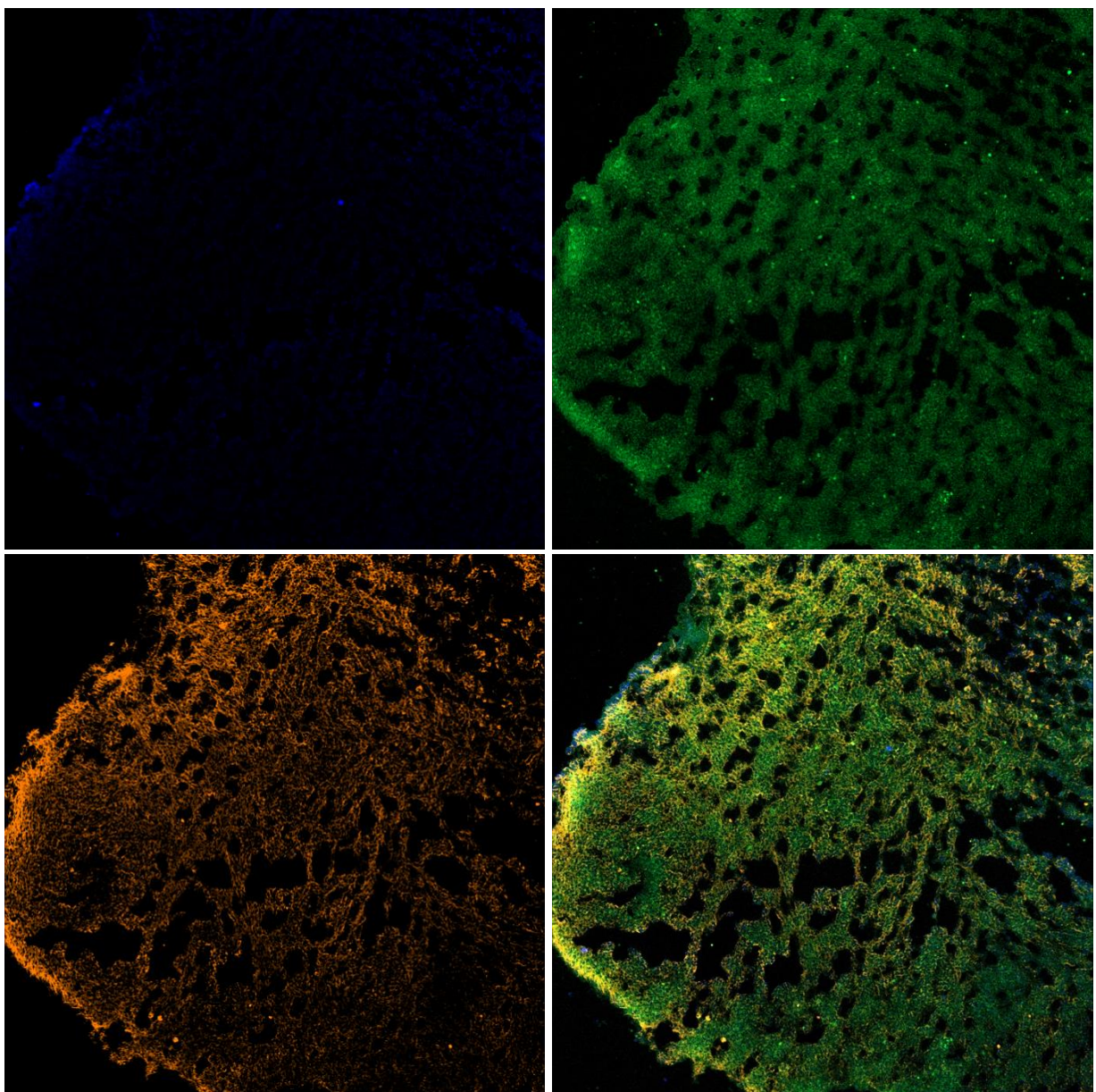


Figure 38 DAPI (Top Left), PAX6 (Top right), MAP2 (Bottom left), and Merged (Bottom right) Immunostaining of Day 42 Brain Organoid

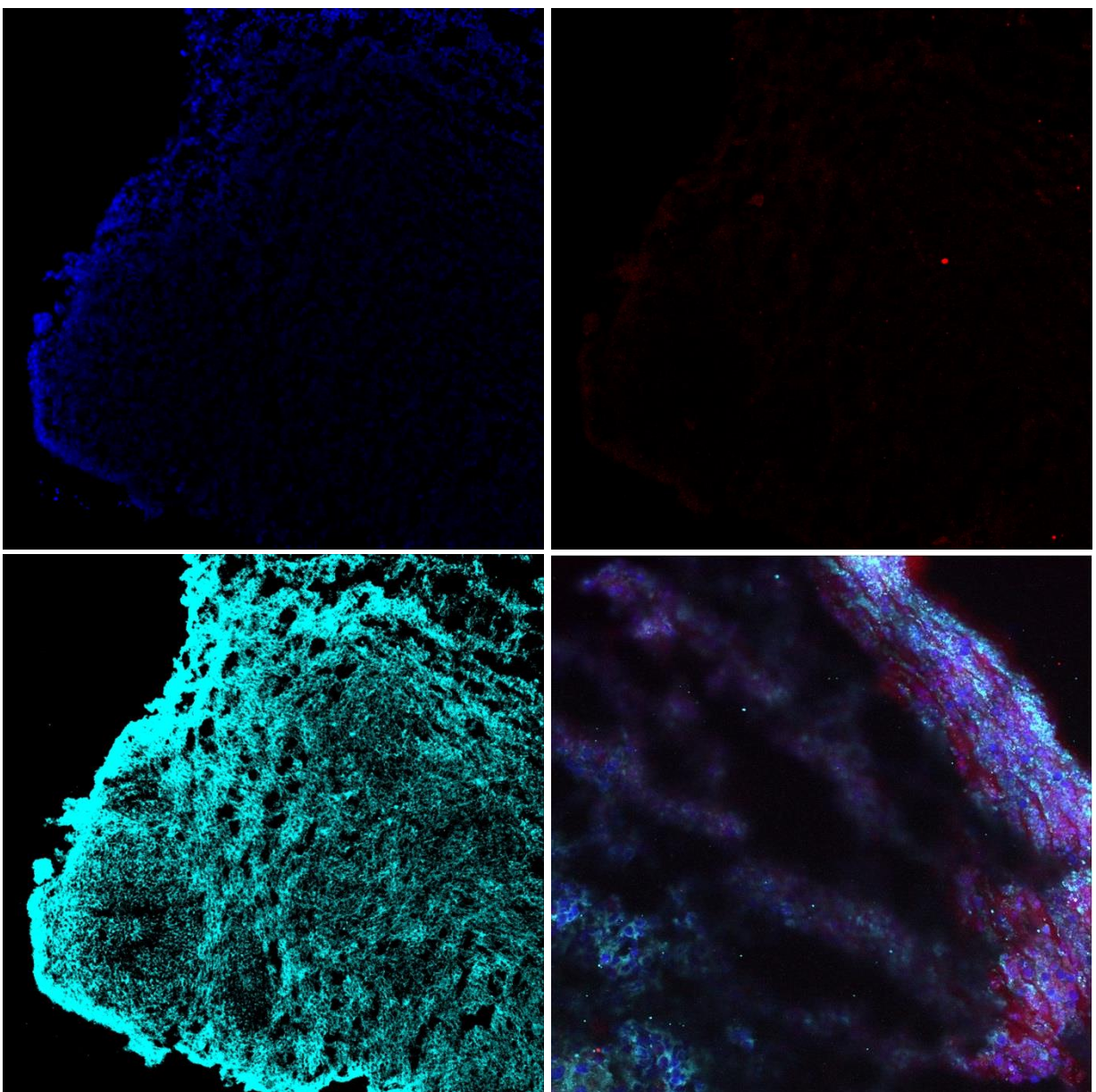


Figure 39 DAPI (Top Left), PSD95 (Top right), SYN (Bottom left), and 20x Merged (Bottom right) Immunostaining of Day 42 Brain Organoid

## 5.2 Microelectrode Array System

The MEAs System is employed for investigating the electrophysiological activity of the brain organoid, where the core of the system revolves around three components, including a custom-designed MEAs PCB serving as an interface between the brain organoid and the signal acquisition system. It houses a grid of microelectrodes designed to non-invasively detect changes in voltage. The signal acquisition system consists of the Brain Organoid SiP platform, an integrated system that includes a BCI Lab's SiP as main component, responsible for the analog front end to receive and digitize raw electrical signals and the Python-based Data Processing System for data handling, visualization, filtering, and storage. This integrated approach aims to provide a comprehensive tool for characterizing the electrophysiological landscape of the brain organoid.

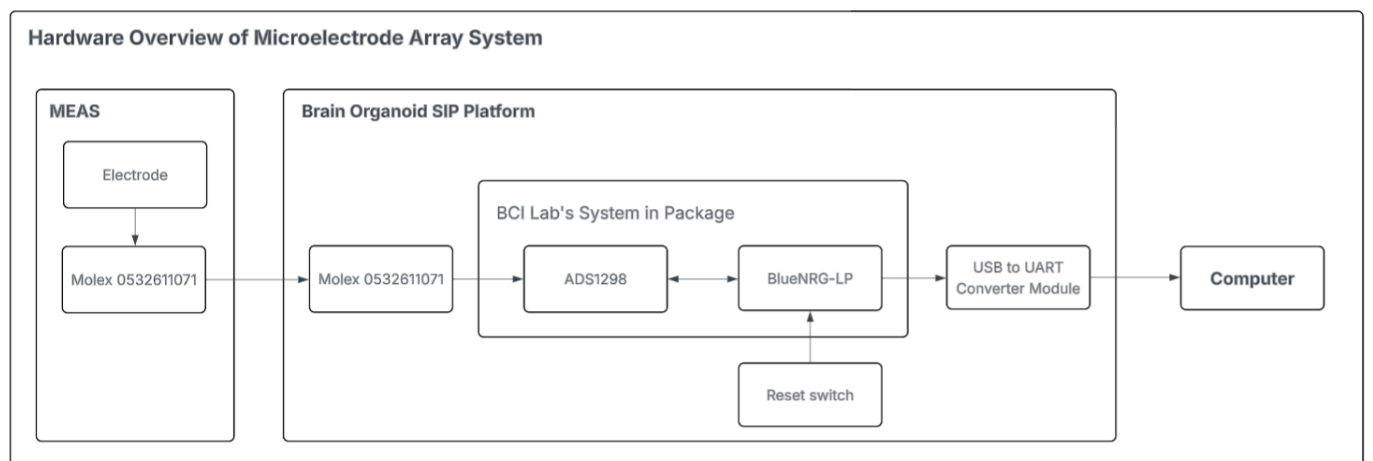


Figure 40 Hardware overview of Microelectrode Array System

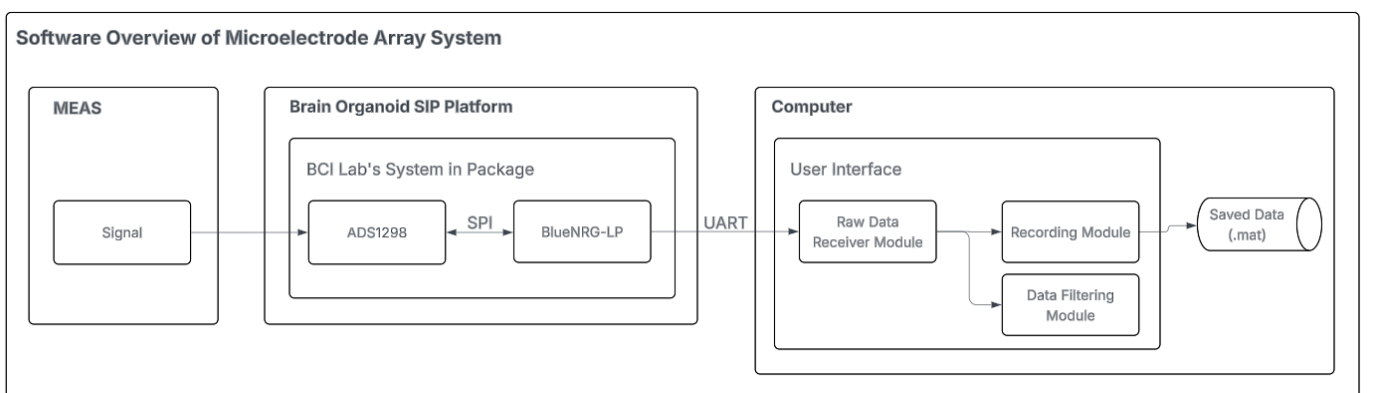


Figure 41 Software overview of Microelectrode Array System

### **5.2.1 Microelectrode Array PCB**

The MEAs PCB serves as the physical interface for recording electrophysiological signals from the brain organoids. The design adheres to the constraints imposed by the Brain Organoid SiP Platform with its 8 input channels and PCB fabrications limitation.

The electrode array has a total of 8 recording electrodes serving as a positive electrode input, matching the 8 input channels of the Brain Organoid SiP Platform. The electrodes are arranged in a 3 x 3 grid configuration with the center position left empty resulting in the required 8 electrodes surrounding a central area where the brain organoid will be positioned. Each individual recording electrode has a circular shape with a diameter of 0.25 mm. This size is chosen to provide sufficient surface area for detecting extracellular voltage fluctuations while maintaining a responsible spatial resolution. The center-to-center distance between adjacent electrodes in the grid is 0.75 mm. These spacing aims to balance spatial sampling of the organoid's activity and the limitation of the PCB production process. The overall dimensions of the 3x3 electrode grid are therefore approximately 1.5 mm x 1.5 mm (considering the centers of the outermost electrodes). The recording electrodes are covered with an ENIG surface finish. ENIG provides excellent corrosion resistance, great electrical conductivity, and biocompatibility, ensuring reliable signal transduction and minimizing potential harm to the organoid. The reference electrode is positioned nearby. This electrode is located near the inside edge of the borosilicate ring. This placement aims to provide a stable reference potential, minimizing common-mode noise and improving signal quality. The material and surface finish of the reference electrode is also ENIG surface finish similar to the recording electrode. The borosilicate ring is a cylindrical well made of borosilicate glass used to contain the brain organoid and the culture medium chosen for its biocompatibility and inertness. The borosilicate ring has an outer diameter of 25.4 mm. It is securely attached to the MEAs PCB using a biocompatible acrylic glue. This adhesive will create a leak-proof seal. To facilitate accurate placement of the borosilicate well onto the PCB, a circular silkscreen guide with a diameter of 25.4 mm matching the outer diameter of the well is printed on the PCB surface. After the electrode design, the electrical interface between MEAs PCB and Brain Organoid SiP Platform is connected by using the Molex 0532611071 connector. The connector provides a total of 10 pins, accommodating the 8 recording channels, 1 reference electrode, and 1 common ground connection. The pinout of the connector on the PCB will be designed to match the input configuration of the Brain Organoid SiP Platform. The grounding of the PCB is implemented by a dedicated ground plane. The continuous ground plane serves to minimize electromagnetic interference and provide stable

ground reference for electrical signals. The additional PCB features include electrode layout labeling guide which is done by a white silkscreen label indicating the channel number for the electrode array printed near the array aiding in the identification of the electrode channel arrangement. In the similar design, the pinout of the Molex connector also be clearly labeled on the PCB adjacent to the connector footprint to facilitate the easy and accurate connection to the SiP platform. The PCB also has drilled holes in each corner of the PCB for potential future integration with the mechanical base or stabilization platform. The overall dimensions of the MEAs PCB is approximately 100 mm by 100 mm. This size accommodates all the described features while remaining manageable for laboratory handling.

The final design has been changed from the initial prototype due to the fPCB does not providing a flat connection between the PCB and the connector board. The design is also changed to give more space around the electrode to make more practical usability on embedding process.

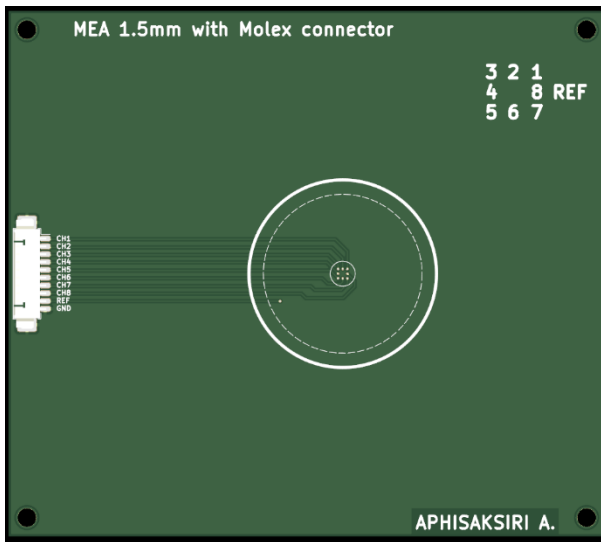


*Figure 42 Microelectrode Arrays*

The initial verification steps are required on the fabricated MEAs PCB before its use with brain organoids. The aim is to ensure the integrity of the electrical connections, assess electrode impedance, and verify the signal transduction capabilities of the PCB. The verification of an electrical connection between each electrode pad on the MEAs PCB and its corresponding pin on the Molex connector and check for any breaks or damage in the conductive traces on the PCB is executed by setting the multimeter to continuity testing mode and placing one probe of the multimeter on the electrode pad on the MEAs PCB, the other probe placed on the corresponding pin of the Molex connector, repeat for every pair. The result of the connectivity test should

confirm the unbroken electrical path indicating continuity of every electrode. Next is the impedance measurement, Similar to the connectivity, this tests for the impedance between the electrode pad to its corresponding pin on the Molex connector. The impedance analyzer is used to measure the impedance. The expected result of the test is the impedance value should not have significant deviations between the electrodes or excessively high/low impedance values may indicate fabrication issues. Lastly, to verify the MEAs PCB's ability to transduce and transmit electrical signals by introducing known waveforms and observing the output at the Molex connector. In order to create a simulated signal, we use a Netech MiniSim EEG signal simulator device. By connecting the output of Netech MiniSim to a representative set of electrodes on the MEAs PCB, we can measure the electrical voltage at the Molex connector to see the transmitting capability of the MEAs PCB. The configuration of the Netech MiniSim can be set to generate small spikes, sin wave, triangle wave, square wave at different amplitude and frequency. For each generated waveform, it is connected to the microelectrode array system to observe the signal. The generated waveform should be clearly discernible; the amplitude and frequency should correspond to the settings on the Netech MiniSim.



*Figure 43 Verification of MEA by microscope*

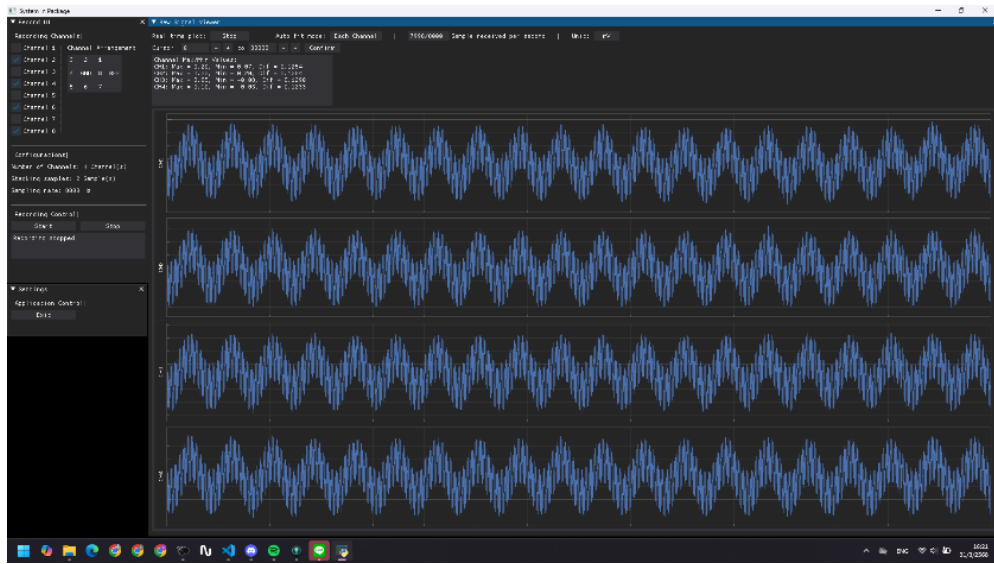


Figure 44 External signal test by Netech MiniSim. The sin wave is generated at  $50 \mu\text{V}$  at  $5 \text{ Hz}$ .

### 5.2.2 BCI Lab's System in Package

In the brain organoid SiP platform, the BCI Lab's SiP is a core component which serves as a central controller in the data acquisition system. As the electrophysiological signals of brain organoids from MEAs typically have a frequency band up to 3,000 Hz at an amplitude around  $50 \mu\text{V}$ , the SiP is set to capture 4-channel data at 8,000 samples per second from 8 channels without amplification, which is sufficient to obtain spikes, avoid system saturation of the system and prevent aliasing. Within SiP, there are two core components that involve constructing a data acquisition system, including the ADS1298 function as the analog front end to detect the signal and then digitize it into 24-bit data. The BlueNRG-LP, which is the MCU, is responsible for stacking the data into a package before transmitting it to the recording application on the computer.



Figure 45 brain organoid SiP platform

### 5.2.2.1 Firmware of System in Package

The firmware for BlueNRG-LP, which is used to control the ADS1298 and data packing process, is written in the C language by using ArmKeil µVision5 as a software development tool. In addition, the RF Flasher utility is used to upload code. In the internal configuration, the system first initializes the GPIOs and environment for the serial peripheral interface (SPI) and UART communication protocol. Next, the SPI is utilized with direct memory access (DMA) for high-speed data transmission between ADS1298 and BlueNRG-LP, minimizing central processing unit (CPU) involvement and processing time. In the SPI communication protocol, the data transfer by prioritizing the Most Significant Bit (MSB) and an SPI clock is implemented at a speed of 4 MHz. After the Chip Select (CS) pin is activated via a low logic level signal, the commands and op-codes for ADS1298 configuration are sent via the Master Out Slave In (MOSI) pin. With the successful configuration, the ADS1298 will be able to receive the signal from 8 channels of MEAs in format of hexadecimal number and send it to BlueNRG-LP through the Master In Slave Out (MISO) pin. In the data packing system, the four-channel data from the eight channels will be selected and then stacked twice. The stack will finally be packed into a package by adding a one-byte header and a one-byte terminal, which are 0xAA and 0xFF, respectively.



Figure 46 Data package architecture

The package, which consists of 26 bytes, results in data transmission at 832,000 bits per second. This package will be transferred out to the computer by implementing the UART communication protocol. UART is also used with DMA, which prioritizes the Least Significant Bit (LSB). The baud rate for UART is optimally set to 1,250,000 bits per second, which covers all data transmission in a system in one second.

Our firmware is verified through the prototype hardware, which consists of a preliminary connection between ADS1298 and BlueNRG-LP, simulating the BCI Lab's SiP as illustrated in Figure 47

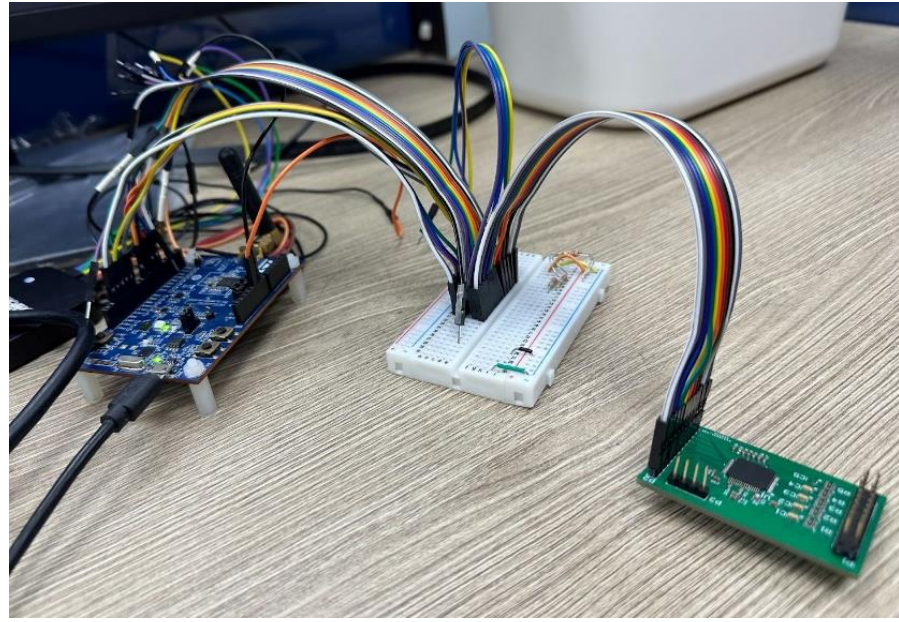


Figure 47 The initial prototype of brain organoid SiP platform

The SPI communication is successfully constructed by confirming on the Saleae Logic Pro 8, or logic analyzer. On the logic analyzer application, the CS line should be low to start communication. Then, the SPI clock line generates a signal at 4 MHz. Simultaneously, the data on the MOSI or MISO line will be transmitted as shown in Figure 48.

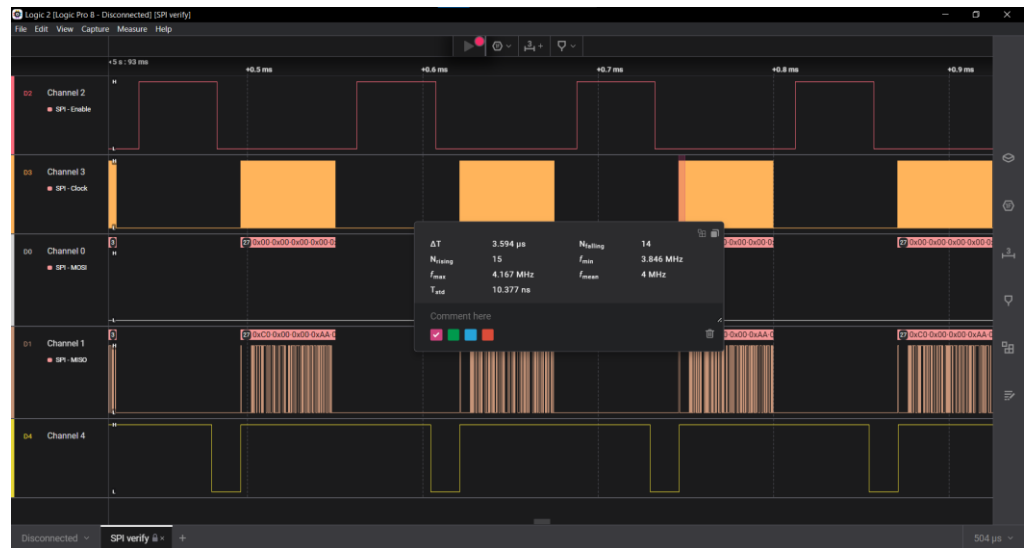


Figure 48 Verification of SPI communication protocol where line 1 is CS, line 2 is SPI clock, line 3 is MOSI, line 4 is MISO and line 5 is DRDY.

Moreover, the same hexadecimal number in both MOSI and MISO lines, and the data ready (DRDY) line at 8000 Hz indicate the accomplishment of ADS1298 configuration.

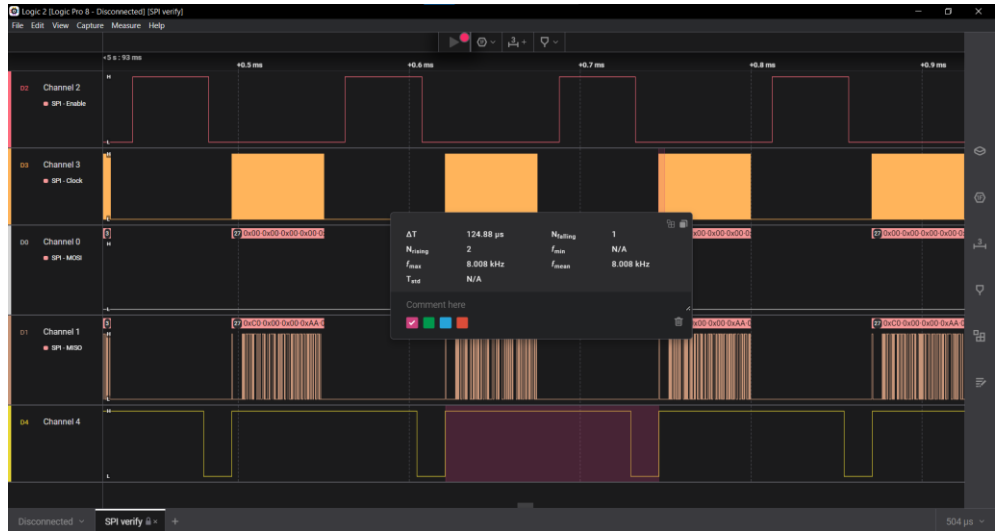


Figure 49 Verification of ADS1298 configuration where line 1 is CS, line 2 is SPI clock, line 3 is MOSI, line 4 is MISO and line 5 is DRDY.

In the verification process of data packing, the known data, such as numbers 1 to 101, is generated and stacked as the package. It is also checked through the logic analyzer in the async serial line that the total byte must be equal to 26 bytes, which start with 0xAA and end with 0xFF.



*Figure 50 Verification of data packaging process*

Next, UART communication is verified by realterm, logic analyzer, and plotting using Python code. The realterm is used to confirm that UART communication with DMA is appropriately constructed by sending the known data, which is 0x00, 0x01, 0x02, 0x03, 0x04, and 0x05.

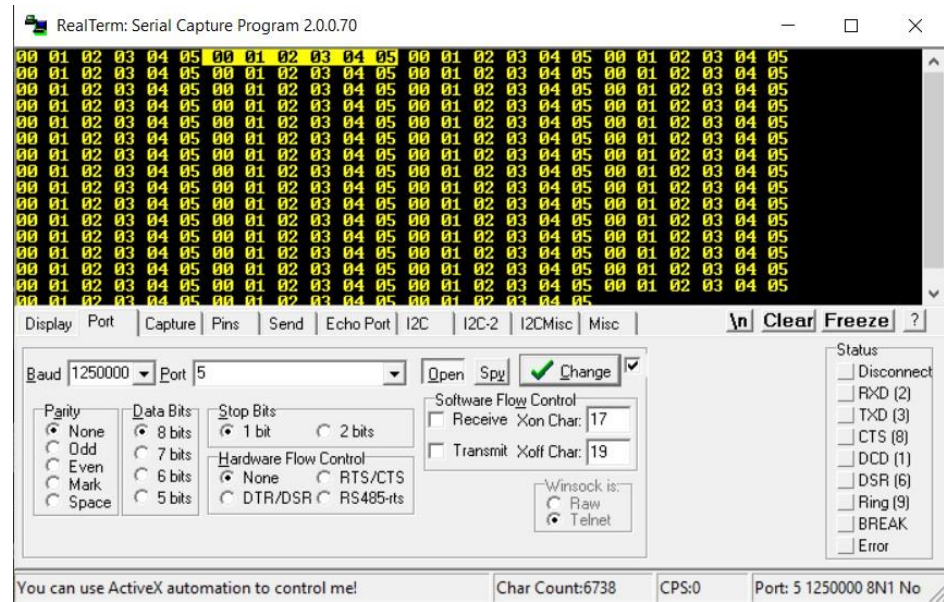


*Figure 51 preliminary verification of UART communication protocol*

Next, a logic analyzer is used to find the most suitable channel number, baud rate, and data stacking number, aiming to achieve the fastest transmission with the most data and prevent data loss. After several trials and errors on baud rate, we can get the maximum value of the system, reaching up to 1,250,000 bits per second. Based on the maximum baud rate, the applicable values of channels and stacking numbers are 4 and 2, respectively. These values have ultimately utilized the full performance of BCL Lab's SiP. Lastly, the plot by Python code is used to confirm that all data has been completely transferred to the computer without data loss, as shown 1-101.

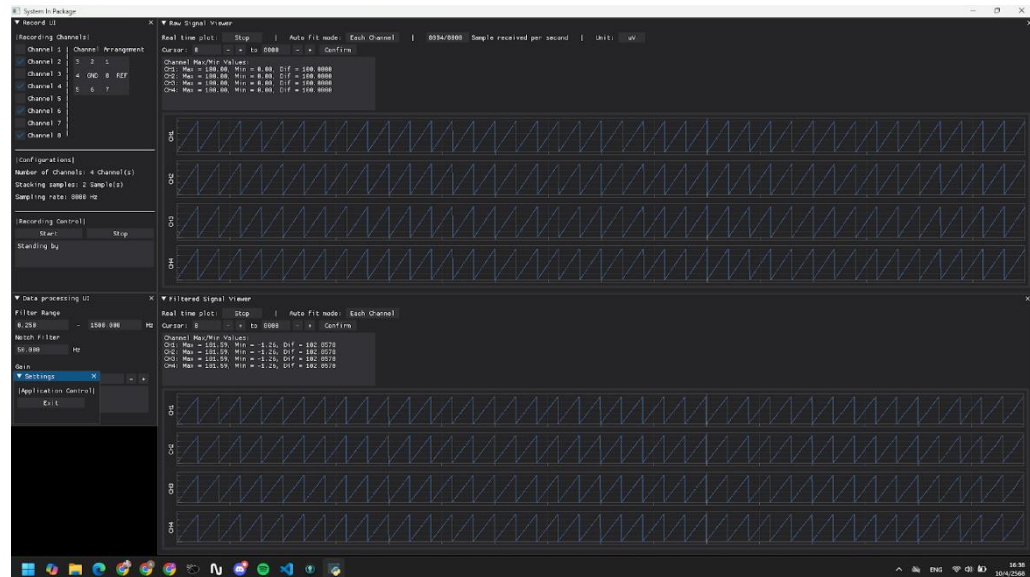


*Figure 52 Sawtooth wave test (1-101)*

Upon completion of the verification process on communication protocols, the firmware is continuously verified with the internal and external signal test. First, the internal signal test is done by configuring ADS1298 to generate the signal by itself internally. The internal signal will be in the form of a square wave with an amplitude of 24mV at a frequency of 2 Hz as shown in Figure 53 . The success of the internal signal test will indicate that the configuration of the BCI lab's SiP is correct and works properly.

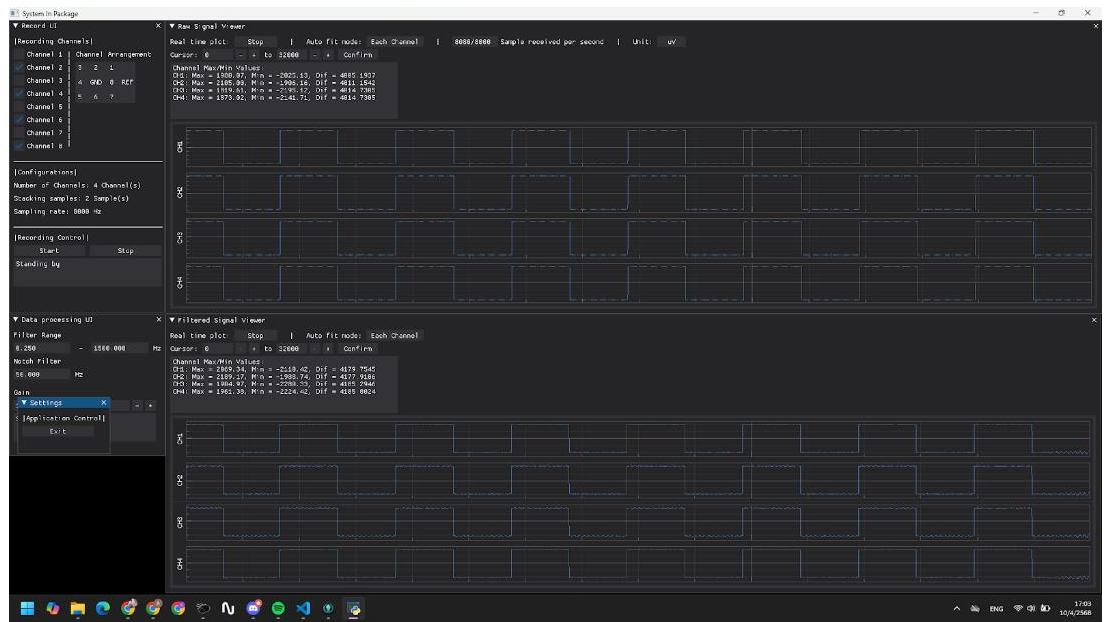


Figure 53 Internal signal test by ADS 1298

Next, the external signal test will be conducted by the Netech MiniSim which will generate the known signal at  $\mu$ V scale at various frequencies, starting from 100  $\mu$ V to 10  $\mu$ V. This test is used to verify the ability of ADS1298 to sense the microvolt input and observe the response of a micro scale voltage compared to the noise background of the system. All of the results are plotted on the user interface which are illustrated in Figure 44, Figure 54, Figure 55.

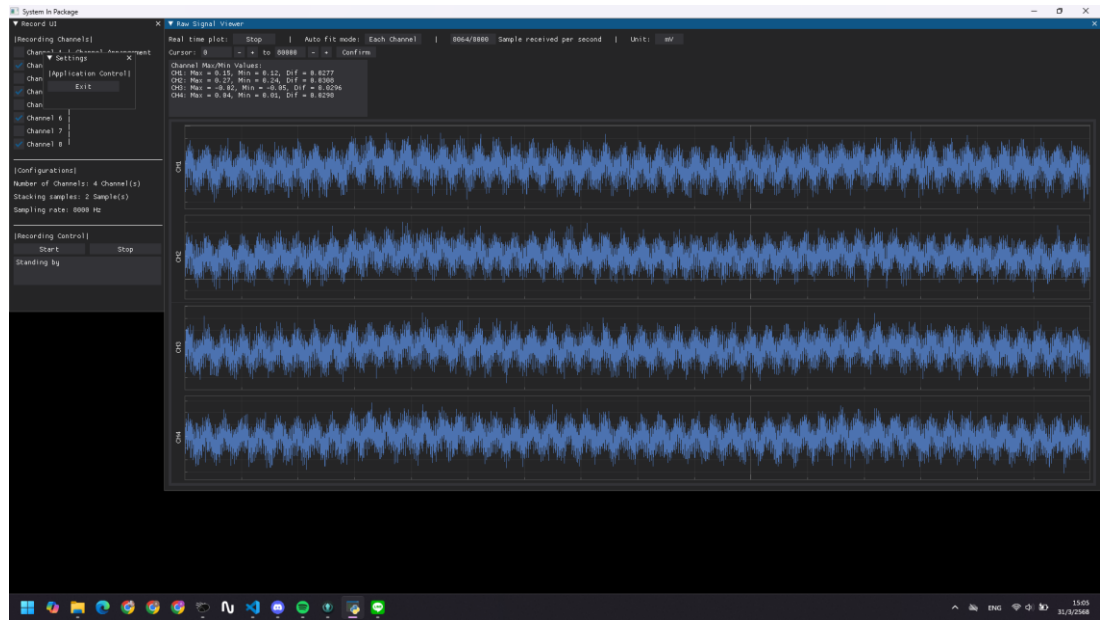


Figure 54 External signal test by Netech MiniSim. The sin wave is generated at  $10 \mu\text{V}$  at 5 Hz.

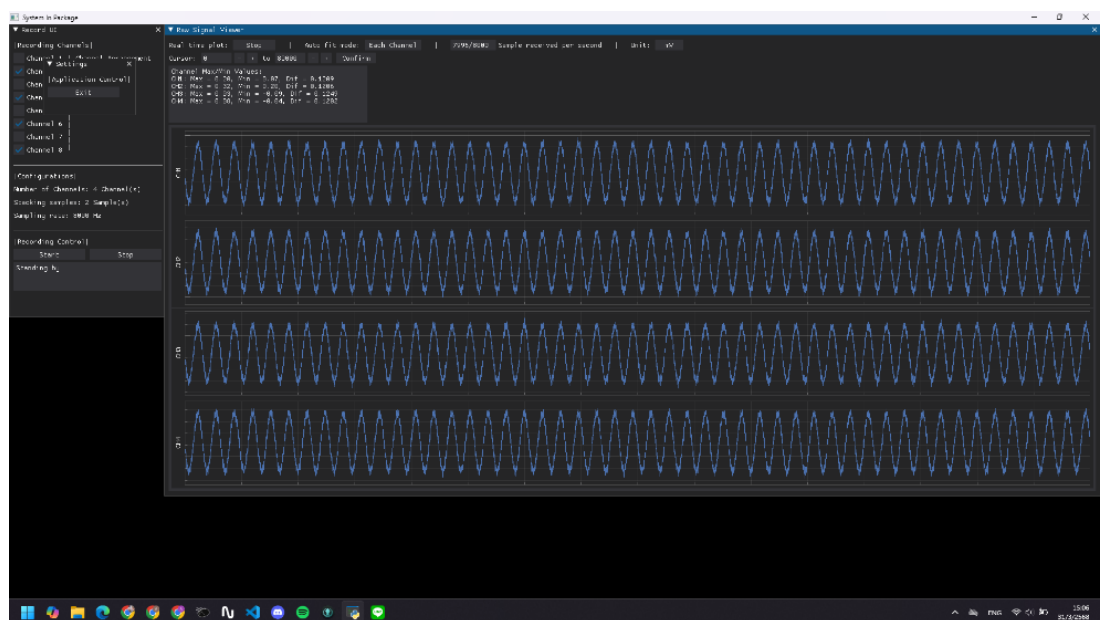
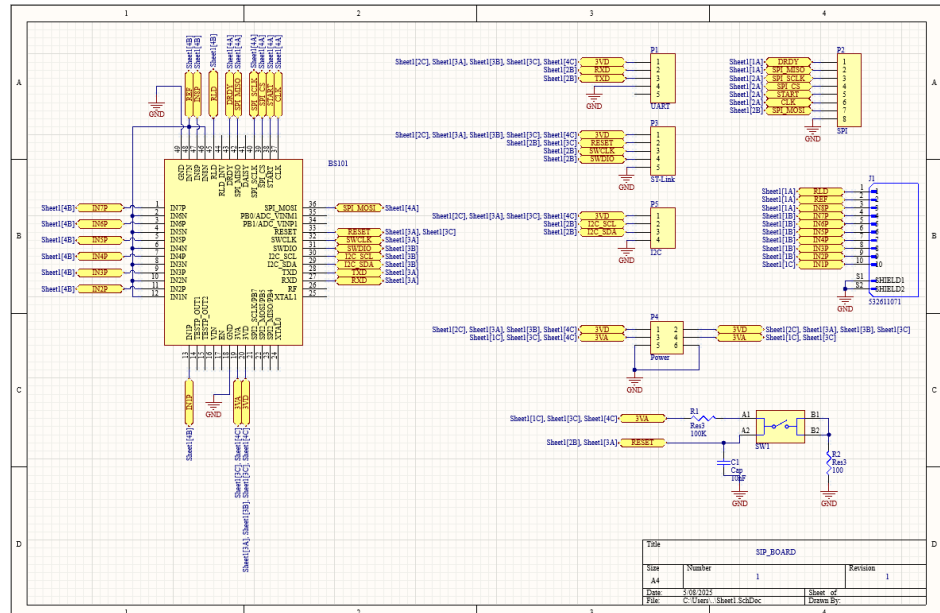


Figure 55 External signal test by Netech MiniSim. The sin wave is generated at  $100 \mu\text{V}$  at 5 Hz.

### 5.2.2.2 System in Package Printed Circuit Board

The initial prototype of hardware which is shown Figure 47 The initial prototype of brain organoid SiP platform simulates the functions of the BCI Lab's SiP to study operation and develop our firmware. The final design of our acquisition hardware is in the form of a single PCB layout, which has dimensions of 6.5 cm in width and 5 cm in length, designed in Altium Designer software. The SiP is implemented at the center of

the PCB and all negative input channels are directly connected, making the unipolar measurement. Furthermore, there are connectors and a reset along the side of the PCB. The Molex Connector 0532611071, which is similar connector on our MEAs, is selected to connect between the SiP PCB and MEAs for receiving the electrophysiological signal from 8 channels of MEAs. This connector is a cost-effective component that provides connection of reference in electrode and ground in both PCB. On the other hand, the UART to Universal Serial Bus (USB) Converter Module serves as the output connector to send out data via UART. The reset switch is constructed using resistors, a capacitor, and a push-button to reset the entire system. Additionally, open pins are provided for system debugging, including access to SPI, UART, and code uploading. In the component placement, the components that handle analog and digital signals are separately placed and carefully routed to reduce interference between the analog and digital sections. Moreover, ground planes are placed on both sides of the PCB, which serve as a common reference ground to minimize noise, while a 3.3V supply powers the entire system. In addition, The SiP PCB also has drilled holes in each corner of the PCB which is similar to MEAs.



*Figure 56 Schematic diagram of SiP PCB*

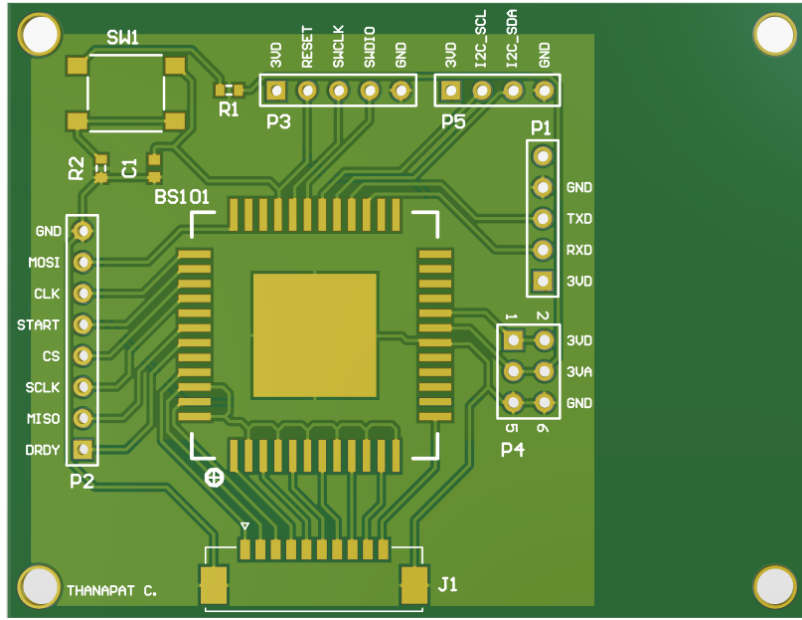


Figure 57 Top view of SiP PCB layout

The initial prototype was verified through simple transmission by SPI and UART communication protocols. Moreover, the connection was also checked with a multimeter in continuity testing mode, which compares to the schematics from their datasheets. In the Altium Designer software, the SiP PCB is first confirmed by the design rule check, which meets all specifications and has no technical problems. After the PCB is fabricated and all components are soldered, the connections and short circuits are checked by using a multimeter and microscope. The SiP PCB verification will be performed by uploading the verified firmware and repeating the same tests as the firmware, including internal signal test and external signal test. The results on the user interface must match those of the first prototype.



Figure 58 Verification of SiP PCB by microscope

### **5.2.3 Data Processing Application**

The Python-based Data Processing Application serves as a central hub for handling the electrophysiological data, responsible for receiving, processing, visualizing, and recording of the electrical signal acquired from the brain organoid via the Brain Organoid SiP Platform. The application is built using a modular approach within our custom Python library named [brainorganoid](#). The system is designed around several core modules that communicate with each other through a shared buffer. This modular design promotes separation of concerns and facilitates independent development and testing. The Data Processing system comprises of interconnected modules including

#### **5.2.3.1 Base Modules**

Base module of the library provides a foundational functionality that is essential for the overall application. These utility files are essential because they encapsulate common functionality that can be reused across multiple modules, promoting reusability. Their modular structure helps maintain an organized codebase by clearly separating foundational logic from higher-level application logic. Additionally, they enhance maintainability, as updates to utility functions or configurations can be made in a single location, minimizing the risk of errors and inconsistencies.

#### **Abstractthread**

Threading or in the application is called Abstractthread class serves as a base class for every module in this library, it provides a framework for creating and managing periodic threads in Python. The class handles thread creation, periodic execution, and thread-safe stopping. The key features are: periodic execution, which runs the user-defined method (update method) at a defined frequency or period. Another feature is thread management, which provides methods to start and stop threads safely. Furthermore, the thread frequency is customizable, allowing the setting of a thread's execution period. This is useful for threads that do not require constant updates, like a user interface, which can be run at lower frames per second.

#### **Buffer**

Acting as fixed-size intermediate storage, the Buffer class is essential for our real-time processing system, which demands chunk-based data handling. It provides a structured approach to managing incoming and outgoing data streams

within a fixed-size array, overwriting older data when full. This ensures efficient storage and retrieval for processing. To guarantee thread-safe updates, a Data Updated Flag signals the availability of new data. Leveraging NumPy, the Buffer class achieves efficient data management without continuous memory reallocation, minimizing CPU workload. Furthermore, it incorporates mechanisms for data synchronization between sender and receiver, including checks for buffer fullness and data update status, thus controlling data flow. Designed for versatility, the buffer accommodates the addition of single data points, multiple data points, or entire data batches, making it adaptable to various application needs.

### User Interface Render

The user interface (UI) render provides a utility function for initialization and rendering of the graphical user interface using a Dear PyGui library. It acts as a centralized module to set up and manage the application's viewport. The UI render main function is to initialize the Dear PyGui context and configure the application by loading preconfigured settings from the previous session to manage each modules' window size, title, position, and other properties. After the initialization of the UI render, each module can add its window to show on the viewport. This essentially creates a single place to initialize and render the UI, ensuring consistency across the application and simplifies the process of setting up the Dear PyGui context and viewport, making it easier to integrate UI components.

#### 5.2.3.2 Raw Data Receiver Module

Raw Data Receiver module is designed to handle data acquisition from the serial communication interface. It is responsible for reading raw data from the serial port, processing it into a usable format, and sending it to buffers for further processing or recording. The class extends the Abstractthread class, enabling it to run as a periodic thread.

The data receiver establishes communication with the Brain Organoid SiP platform and continuously listens for incoming data packets. It expects to receive 26 bytes of data every 1/4000th of a second (corresponding to 8kHz sampling rate, with 2 data

samples stacked per time step). The module ensures data integrity by checking the correct bytes of header and terminator and checking the length of the packet. It then extracts the 24-bit data after removing the header and terminator bytes. The 3-byte representation for each sample in each channel is then converted into a floating-point (double) voltage within the range of -2.4 to 2.4 V. The decoded voltage for all channels is then added to the Raw Data Buffer. Simultaneously, the decoded voltage values are also added to the Record Buffer for the recording module.

The design of the Raw Data Receiver Module is based on multiple considerations such as a modular structure by separating the serial connection, data reading, conversion, and processing makes the class easier to maintain and extend. The module also has an error handling on the serial connection by retrying the connection and validating the data packages to ensure data integrity. Real-time processing is one of the most important requirements for this module as it needs to receive the data in real-time and send it to buffers for further processing and also support down-sampling to reduce data size to lower the computational power. The module supports flexibility in the usage by having configurable parameters like unit multiplier, down-sampling factor, buffer assignment, and other Brain Organoid SiP Platform constants which can be adapted to different configurations and data formats.

### 5.2.3.3 Data Filtering Module

The Data Filtering Module is designed to handle real-time signal processing by applying high-pass, low-pass, and notch filters to incoming data. It extends the Abstractthread class, enabling it to run as a periodic thread for continuous data processing. The class is modular, configurable and supports saving filter coefficients for reproducibility and verification. The module is implemented because the electrophysiological signal from the brain organoid is minuscule, a subtle noise could ruin a data set. One of the most important filters is the notch filter at 50 Hz. It is designed to attenuate noise originating from power line interference, which is a common artifact in the recording

The module features multiple key components including a filter design which implements methods to design high-pass, low-pass, and notch filter using the SciPy Signal library which supports configurable filter parameters such as cutoff frequency, filter order, and quality factor which can be configured. After the designing, the filters

are used for real-time processing by reading the raw data from the inlet buffer which is Raw Data Buffer and writing the filtered data into an outlet buffer, Filtered Data Buffer. In every filter design, the filter coefficients are saved into a .json file. In the final design, the filter order of high-pass and low-pass is 4 with the notch filter denying 50 Hz noises.

Similar to Raw Data Receiving Module, the design consideration of the module includes a modular structure where it separates methods for filter design, data processing, and configuration management making the module easy to maintain and extend. It features flexibility by supporting dynamic adjustment of filter parameters and also able to adapt to different sampling rates and filter requirements with the raise of warning when filter parameters are not possible in sampling rate range, to illustrate, the low-pass filter cutoff frequency cannot be set to more than 4,000 Hz at the 8,000 Hz sampling rate or High-pass filter cannot be set below 0 Hz.

#### **5.2.3.4 Recording Module**

The recording module is designed to handle real-time data recording for further analysis, written with the same structure as the Raw Data Receiving module. The module extends the Abstractthread class to enable periodic execution.

The recording module consists of data acquisition where it will monitor the Record Buffer for new data, when new data is detected, the module retrieves it from the Record Buffer. It then appends the data into a .mat file, the Record Buffer is then cleared to prevent the risk of obtaining the repeating data points. At the same time the module also gets crucial metadata which includes Sampling rate, Recording Channels, and number of samples, these metadata are embedded in the same file. The MATLAB dataset file is automatically generated with the file name based on the current date and time to label the data session and also dynamically resize the dataset size to accommodate the incoming data over the period of recording session

#### **5.2.3.5 User Interface**

The user interface (UI) of the application is designed to provide a comprehensive and interactive environment for managing data acquisition, processing, visualization, and recording. The UI is implemented using the Dear PyGui library and consists of several components, each tailored to specific functionalities including Raw Data Receiver UI, Data Filter UI, Recording UI and settings UI. Each component is implemented as a class

that inherits from the `Abstractthread` base class, enabling periodic updates and real-time interaction.

The integration of the user interface is done by initialization, the backend of UI components is initialized and assigned to the appropriate modules and buffers. To illustrate, the Raw Data Receiver UI is assigned to the Raw Data Receiver Module and Raw Data Buffer for it to function properly. Next, the User Interface Render base module is initialized to create a viewport, and each UI component is rendered in its window.

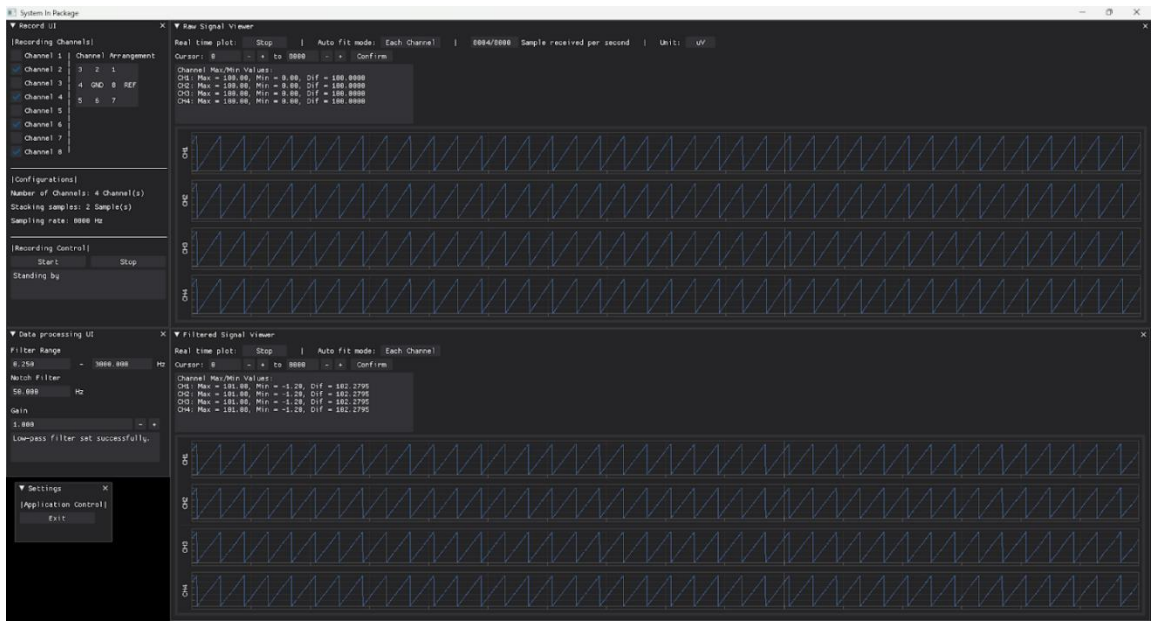


Figure 59 Application User Interface

## Raw Data Receiver User Interface

This window visualizes raw signal acquired from the data acquisition system in real-time featuring: a real-time plotting, displaying raw signals for all channels; cursor control, allowing users to set cursors to analyze specific ranges of the signal; graph auto-fit mode which adjust the y-axis of the graph to each channel or all channel for better visualization; unit toggle, switching between microvolts and millivolts. The elements of the UI include a button to start/stop the real-time plot, a cursor range values including minimum, maximum, and difference of the voltage level in each channel and most importantly the subplots for each channel with real-time updates.

### **Data Filter User Interface**

This component is divided into 2 windows, first section is the filtered data graph to visualize the filtered signals in real-time after applying a filters featuring similar capabilities as the Raw Data Receiver UI including Real-time plotting, Cursor, Auto-fit Mode where it excludes the unit toggle button as the unit is the same as the Raw Data. The second window of the Data Filter UI is the Data Processing UI, it allows users to configure and control the signal processing pipeline, including the filter settings and gain adjustment. The filter configuration includes setting cutoff frequency of high-pass and low-pass filter and setting the notch frequency of the notch filter, adjusting the gain applied to the signal, and also the feedback display to show success or error message for user actions as mentioned above in the Data Filtering Module.

### **Recording User Interface**

The recording UI manages the recording of the data to files in real-time. It features channel selection, allowing users to select specific channels for labeling which channels are being recorded using checkboxes, recording control which includes Start and Stop button for recording and display the current recording status. It also displays the configuration of the current session including Number of Channels, Sampling rate, and shows the Channel arrangement of the MEA.

### **Settings User Interface**

The settings UI provides application-level controls. In the current version, the feature that it has is exiting the application to handle thread safe operations to prevent errors where the exit button will be a button that allows users to safely terminate the application.

#### **5.2.3.6 Additional files**

The architecture and functionality of the application, which encompasses several critical modules including base modules, data pipeline modules, and user interface. Beyond these core features, the application's design prioritizes ease of development and

maintenance through the inclusion of supplementary files such as configuration file and a build script, streamlining debugging, upkeep, and setup processes

### **Configuration file**

The config serves as the central configuration module for the application. It defines various parameters and constants that control the behavior of the system including data acquisition, plotting, filtering, and recording. By centralizing these settings, the file ensures consistency, flexibility, and ease of maintenance across the application. The configuration is imported into various modules across the application to access configuration variables and constants. For example, Raw Data Receiver module utilizes Sampling rate, Number of Channels, and Com port. In the variable part, it features multiple variables that can be configured for each recording session and the constants are for the default value for all of the settings that can be made, to illustrate, in the Raw Data Receiver module the Header value is always 0xAA is stored in the constant.

### **Build script**

The build script is a critical utility for preparing the application for distribution. By automating code obfuscation and executable packaging, it ensures that the application is secure, easy to deploy, and ready for end-users. The final product of the application is the standalone executable file (.exe file). The build script serves two primary purposes, it protects the source code by obfuscating it using PyArmor, making it harder to reverse-engineer and it packages the obfuscated code into a standalone executable using PyInstaller, allowing the application to run without requiring a Python environment, which means the executable file can be run on another machine without any preparation.

The Data Processing Application is authenticated by a verification protocol which ensures its correct functionality in receiving, processing, visualizing, and recording electrophysiological signals. The verification will be conducted in order starting with internal signal generation tests, external signal simulation and functionality tests using electrodes with a conductive solution.

The separated modules are verified first using a built-in python unit test including an Abstractthread and buffer. The purpose of Abstractthread class verification revolves around

verifying thread start/stop behavior to ensure that the thread can start to execute periodic update methods and stop correctly and validate the frequency and period settings to confirm that the thread executes the update method at the specified frequency or period. The test is done by setting the thread period to 0.1 seconds and letting the thread run for 0.5 second. Inside the thread update method, the counter will add 1 to itself every time the thread executes. The test will check if the counter is equal to 5 or not. The results of the test come out positive when the test is executed.

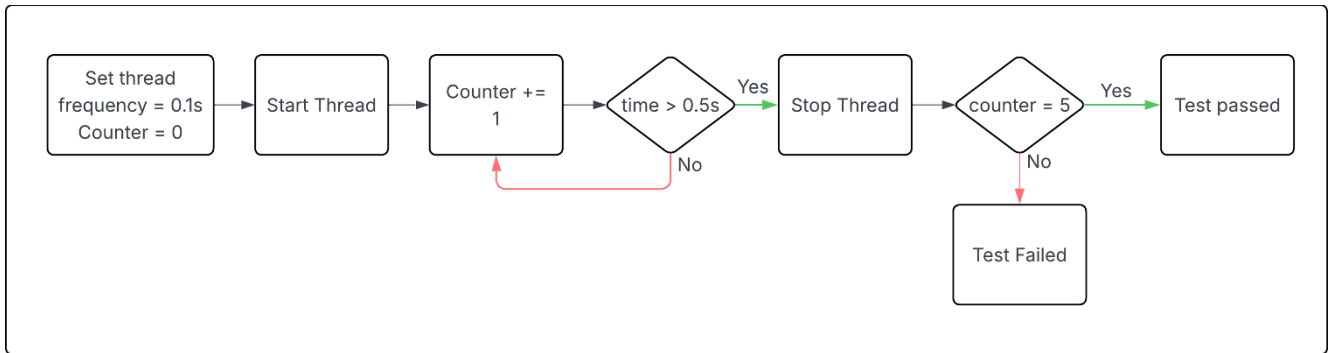


Figure 60 Verification flow of Threading

Another base module that is verified is the buffer. It is verified by the Python Unit test. The tests consist of 3 parts, add data, get data, and flags. The tests are done by creating a buffer with 2 channels and 3 samples length and add a single data point to all channels then verify if the data is added successfully and correctly also check whether the data updated flag is set to True or not, during the test the Flags are tested between steps where the Data Updated Flag should be True when new data is added and should be False when the data is sent to the receiver. The other method of adding data, including multiple data points and batches data, is tested in the same approach but with a different number of samples.

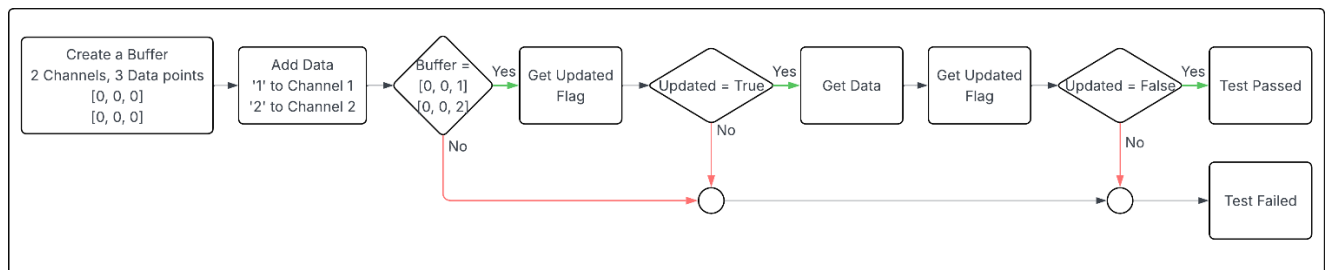


Figure 61 Verification flow of Buffer

After we have verified the internal functions of the application, we need to verify the communication pathway between the microcontroller BlueNRG-LP and Data Processing Application. The procedure of the test includes programming the BlueNRG-LP to generate the sawtooth wave which has the value of 0 to 100 when data is transmitted. The SiP platform then connected to the Data Processing Application to observe the incoming data on the Raw Data User Interface. This verifies the correctness of data by observing the waveform shape, amplitude of each data point that should be 0 to 100 in value before the conversion. This test also verifies the Recording Module by recording the incoming data and uses MATLAB script to read the recorded data and plot it in the MATLAB.

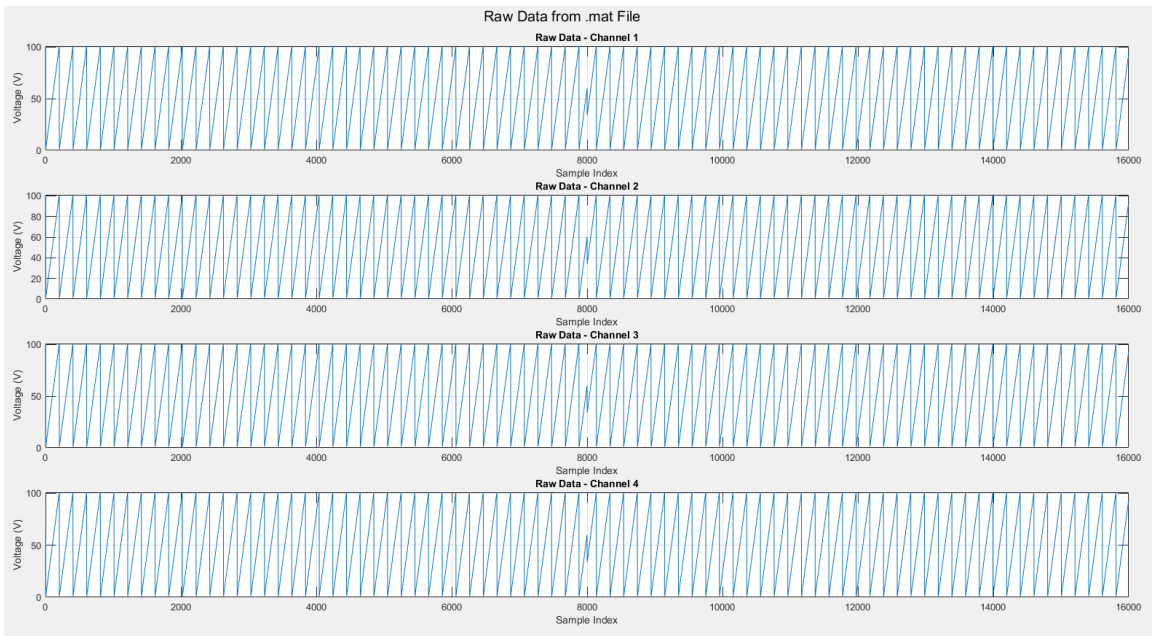


Figure 62 Sawtooth Recorded signal

Then we will verify the communication of the ADS1298 by configuring the ADS1298 to generate and send an internal test signal similar to the verification of the Brain Organoid SiP Platform verification. After we have verified the internal system, the Netech MiniSim EEG signal simulator is used for external signal simulation. The test is conducted to comprehensively test the entire pipeline excluding the electrodes by controlled EEG-like signals at the input of the system. This will assess the accuracy and limitation of the system across a range of signal amplitudes and frequencies. The test is done by connecting the output of Netech MiniSim to the input header pins of the SiP platform and configuring the Netech MiniSim to generate various waveforms at different frequencies and amplitudes. For each generated signal configuration, the raw data should be observed on the Raw Data UI and Filtered Data UI to verify the received

waveforms on the UI to match the shape and frequency of the signal generated by MiniSim, the amplitude of the displayed signals should match the configuration of the MiniSim. The filtering performance is observed to see the effect of 50 Hz notch filter on the lower amplitude signals and identify the limitation of the system in accurately acquiring and displaying signals at the extremes amplitude and frequency ranges. The last test to be performed is the sodium chloride (NaCl) solution test with electrodes. This test is conducted to perform a basic functional test of the complete system, including MEAs PCB, using a conductive solution. The test is done by connecting the electrodes to the SiP platform then connecting the Application to make a complete system. Then fill the borosilicate well on the MEAs PCB with NaCl solutions of varying concentrations ensuring that all of the electrodes are submerged then observe the signals on the Raw Data User Interface. The result should show a baseline voltage fluctuation including low-amplitude noise. The amplitude of the observed signal across different NaCl concentrations should be in trend where higher concentrations of NaCl should generally lead to lower impedance at the electrode-solution interface, resulting in lower amplitude voltage fluctuations.

#### **5.2.4 Experimental Setup for Electrophysiology Recording**

Microelectrode arrays were first coated with Corning Matrigel Matrix (Catalog No. 354230), diluted 1:100 in maturation medium, and incubated at 37 °C for 60 minutes. After removing the medium, a layer of pure Matrigel was applied directly to the electrode surface to enhance organoid adhesion. Brain organoids were carefully positioned onto the coated arrays using wide-bore pipette tips and incubated for an additional 30 minutes at 37 °C to ensure stable attachment. Following adhesion, artificial cerebrospinal fluid (Ringer's solution) was added to maintain physiological ionic conditions during recording. Electrophysiological signals were then recorded using the Intan RHS Stim/Recording System as a gold standard in comparison to our SiP system. To evaluate network responsiveness, N-methyl-D-aspartate (NMDA) was also introduced into the Ringer's solution at a final concentration of 1 mM to stimulate excitatory synaptic activity and assess changes in neural dynamics.

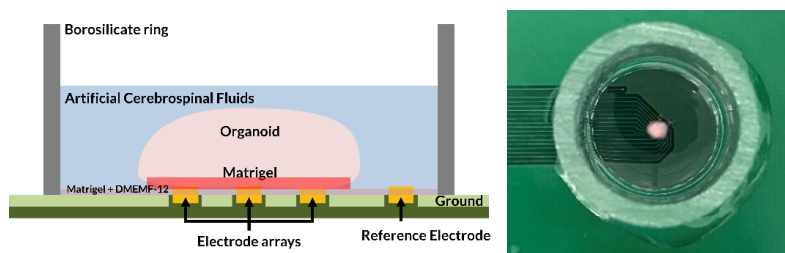


*Figure 63 Experimental setup sideview (left), top view (right)*

### 5.2.5 Electrophysiological signal from brain organoid

After the electrophysiological measurements by our MEAs system, the raw electrophysiological data is stored in the MATLAB data format (.mat), serve as the foundation for further analysis. To prepare the data for meaningful interpretation, we employ a preprocessing stage implemented within the MATLAB environment.

The preprocessing is specifically designed to enhance the signal quality by attenuating unwanted noise components that can obscure the underlying neural activity. To isolate the extracellular spike waveforms, which typically reside within a specific frequency range, we apply a bandpass filter. This filter is configured with a lower cutoff frequency of 300 Hz and an upper cutoff frequency of 3000 Hz. By selectively allowing frequencies within this range to pass while attenuating those outside, we effectively suppress both low-frequency drift and high-frequency artifacts, thereby focusing on the relevant electrophysiological signals. It is designed using the third order Infinite Impulse Response (IIR) butterworth filter.

Furthermore, to remove interference from powerline noise, which occurs at 50 Hz and its harmonic frequencies, we implement a comb filter. This type of filter is specifically engineered to target and remove these discrete frequency components without significantly affecting the broader neural signal spectrum. The application of both the bandpass and comb filters results in a refined dataset where the signal of interest is more prominent and less contaminated by extraneous noise.

This meticulous preprocessing procedure consistently applied to all collected datasets, including control recordings designated as 'baseline noise' and recordings obtained from brain organoids at day 35 and day 42 of their development. This uniform processing ensures that all datasets are subjected to the same noise reduction protocols, facilitating a fair and direct comparison.

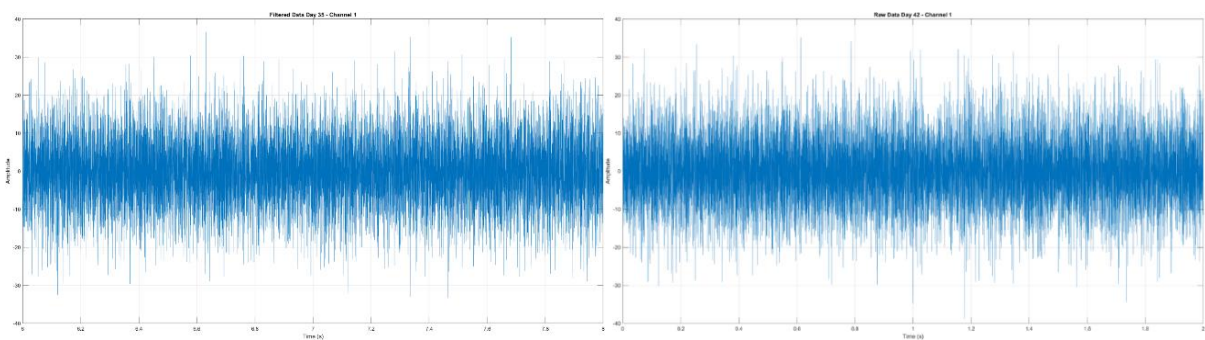


Figure 64 Filtered electrophysiological signal from brain organoid day 35 (left) and day 42 (right).

### 5.2.6 Electrophysiological signal of brain organoid analysis

Following the preprocessing stage, the electrophysiological data analysis is conducted by comparing between the pre-neurostimulation and post-neurostimulation which should result in higher firing rate of the spikes in post-neurostimulation. However, the signal from brain organoid in both day 35 and 42 shows no change in both time-domain and frequency-domain as illustrated in Figure 65.

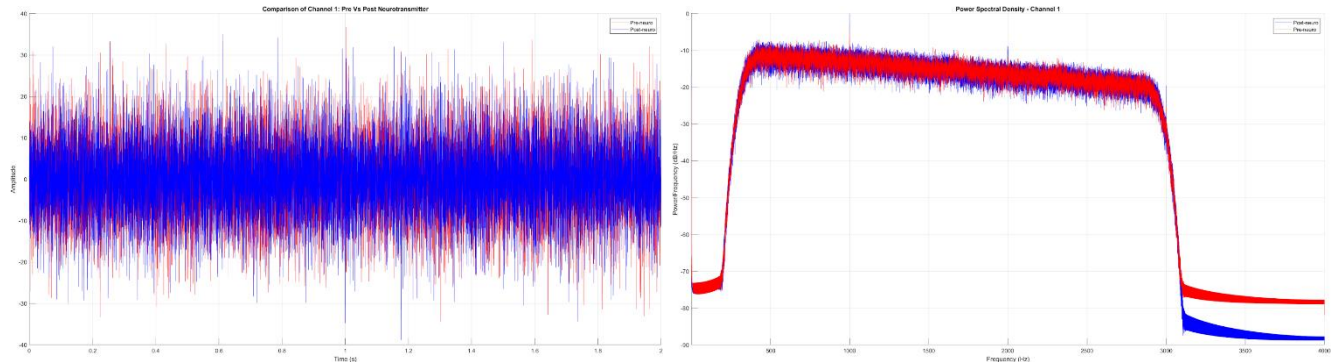


Figure 65 Data ~~from~~ of brain organoid pre-neurostimulation and post-neurostimulation

Next, we chose a set of quantitative metrics, calculated and organized within MATLAB, to characterize and compare the electrophysiological signals across the different experimental conditions including

1. **Rectified mean:** This metric involves taking the absolute value of each data point in the filtered signal and then calculating the average of these rectified values. The rectified mean provides a measure of the overall signal amplitude, irrespective of its polarity. By comparing the rectified means across the noise control and the organoid recordings at different time points, we aim to discern any baseline differences in overall electrical activity and the spiking of the organoid.
2. **Mean Peak-to-Peak Voltage:** To capture the dynamic range of the electrical fluctuations, we calculate the peak-to-peak voltage for individual events within the filtered signal and then determine the average of these values. The peak-to-peak voltage represents the difference between the maximum and minimum amplitude of a detected event. Comparing this metric across conditions can reveal differences in the magnitude of the electrical events generated.
3. **Peak Count (at a threshold of  $30\mu\text{V}$ ):** To quantify the frequency of potential spiking events, we implement a peak detection algorithm with a predefined threshold of  $30 \mu\text{V}$ . This threshold is chosen to discriminate against potential

action potential from smaller fluctuations. The peak count, expressed as peaks per second, provides a measure of the rate of these events in each recording. Comparing the peak rates across the noise and organoid samples can indicate the presence and developmental changes in the frequency of electrical activity.

4. **SNR:** To objectively assess the quality of the recorded signal relative to the background noise, we calculate the SNR. This value represents the ratio of the power of the desired signal to the power of the background noise, expressed in decibels. A low SNR, such as the one obtained, indicates that the noise power is substantially higher than the signal power, making it challenging to discern genuine biological signals from random fluctuations.

After the calculation of all matrices, we find that the value of each matrix and characteristics in both brain organoid day 35 and 42 are similar to the characteristic of the noise background. In the rectified mean of the noise against brain organoids at day 35 and day 42, the values obtained show very little variation. Similarly, the mean peak-to-peak values and peak counts above 30  $\mu$ V across the different conditions do not exhibit substantial differences that would clearly distinguish neuronal activity.

*Table 3 Comparison of matrices on brain organoid signals and noise*

	<b>Artificial Cerebrospinal Fluid (Noise baseline)</b>	<b>Brain Organoid Day 35</b>	<b>Brain Organoid Day 42</b>
<b>Rectified mean (<math>\mu</math>V)</b>	8.383575	8.444	8.283525
<b>Mean peak to peak (<math>\mu</math>V)</b>	94.64005	92.015925	90.06675
<b>Peak count (Peaks per second)</b>	47.8227	57.2292	48.7309

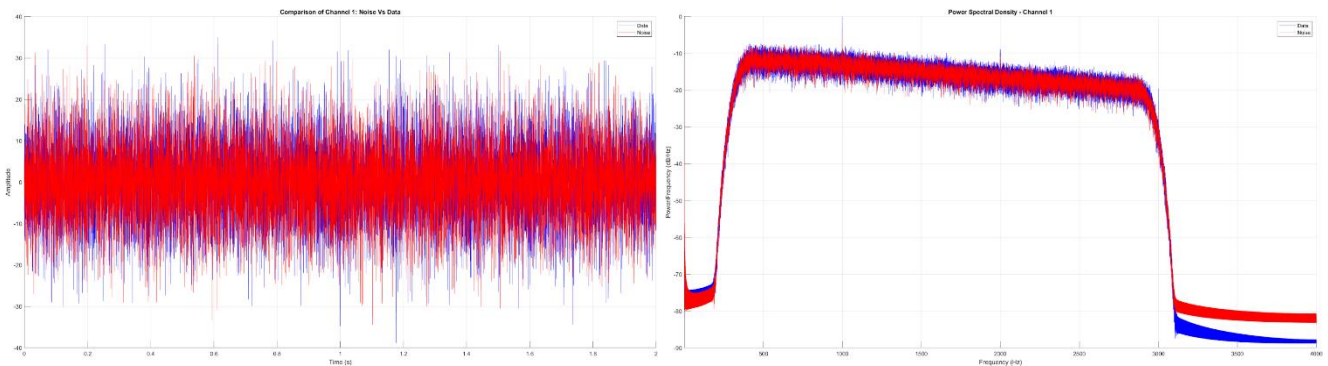


Figure 66 Data of brain organoid and noise

Crucially, the calculated SNR of our MEAs system is exceptionally low at 0.107 dB compared to the SNR of commercial system which reaches 3.320 dB. This indicates that the noise levels in the recorded signal are significantly higher than any potential signal originating from the brain organoid. Consequently, with such a low SNR, it is not possible to confidently conclude that the recorded data reflects genuine electrophysiological activity of the brain organoid. The lack of significant differences across the measured features and the poor signal quality suggests that further optimization of the experimental setup, noise reduction strategies, and potentially the MEAs design itself are necessary to obtain meaningful data on the electrical activity of these organoids.

### 5.2.7 Improvement on Microelectrode Arrays system

In the current SiP platform, the gain is set to 1. In contrast, the Intan RHS Stim/Recording System utilize higher gain settings. Higher gain can amplify the signal, potentially improving the resolution and detectability of small electrophysiological signals from brain organoids. The low gain in the SiP may be insufficient to capture these subtle signals effectively. Therefore, the gain configuration of ADS1298 should be set up to 12 and implement with the analog gain to multiply overall gain up to be higher than 100. Moreover, the current PCB design does not incorporate a rigorous separation of analog and digital signal pathways. This lack of separation can lead to increased noise in the analog recordings, as digital switching noise can couple into the sensitive analog circuitry. Thus, the PCB design could be carefully designed to place analog and digital parts. Furthermore, PCB should be enhanced by the strategic placement of vias in the ground plane. Vias provide a low-impedance path for current to flow to ground, which can help to reduce ground loops and further minimize noise. Last, the choice of connector for interfacing with the MEAs is also a critical consideration. The current connector may not be optimized for

transmitting low-amplitude analog signals, potentially introducing noise or signal loss. Utilizing connectors specifically designed for sensitive analog signal transmission could improve signal integrity.

In addition, the Brain Organoid SiP platform still has several limitations on the number of channels and speed of data transmission that hinder its suitability for advanced brain organoid applications. Most applications require high spatial and temporal resolution to study the brain organoid, so high-speed data transmission and a large number of recording sites are required. The BlueNRG-LP which is responsible for data acquisition and transmission within SiP has drawbacks on data throughput bottleneck. Although the UART protocol has a claimed maximum baud rate of 2 MHz, which should theoretically be sufficient for handling the data from 8 channels sampled at 8 kHz with 24-bit resolution, the experiments revealed a significantly lower achievable baud rate of 1.25 MHz. This discrepancy introduces a bottleneck in the data transmission pathway resulting in the ability to transfer only 4 channels of data. The simultaneous operation of SPI communication with the ADS1298 and UART transmission creates a processing bottleneck, limiting the overall data throughput of the system. This bottleneck can lead to data loss, reduced sampling rates, or the need for data compression, all of which can compromise the quality and integrity of the recorded signals. To mitigate the data throughput limitations, attempts were made to use two microcontrollers, each connected to the same microelectrode array, to handle data transmission separately. While this approach increased the data throughput, it introduced new challenges. Specifically, it resulted in a small time-shift between the data streams from the two microcontrollers. This time-shift, even if small, can complicate data analysis, particularly for studies examining the precise timing of neural events, such as spike timing correlations and functional connectivity. Furthermore, using two microcontrollers increases the computational load on the host computer, potentially requiring more powerful hardware and more complex data processing algorithms.

## 5.3 MEA-NAP : Functional Connectivity Analysis Pipeline

### 5.3.1 Signal Preprocessing

To ensure accurate spike detection, the raw electrophysiological signals from brain organoids were preprocessed to eliminate both low-frequency artifacts and high-frequency noise. Spectral analysis using Fast Fourier Transform (FFT) and Welch's PSD was conducted to assess the frequency content across developmental stages and stimulation conditions. As shown, the Day 35 and pre-stimulation Day 42 signals displayed broad spectral components, with FFT revealing peaks below 500 Hz and around 1–2 kHz, indicative of potential spike activity. The PSD plots showed high power at very low frequencies (<10 Hz), likely due to baseline drift and slow biological fluctuations. After ~300 Hz, the PSD stabilized, supporting the presence of higher-frequency spike activity related to neural events. Following NMDA stimulation , the overall spectral profile shifted. The PSD showed increased power across mid to high frequency bands, and FFT results indicated a redistribution of signal energy, with reduced dominance in low-frequency bands and more balanced spectral energy across 500–3,000 Hz. These changes suggest enhanced network excitability and the emergence of additional spike-related components, further supporting the need for appropriate bandpass filtering during preprocessing.

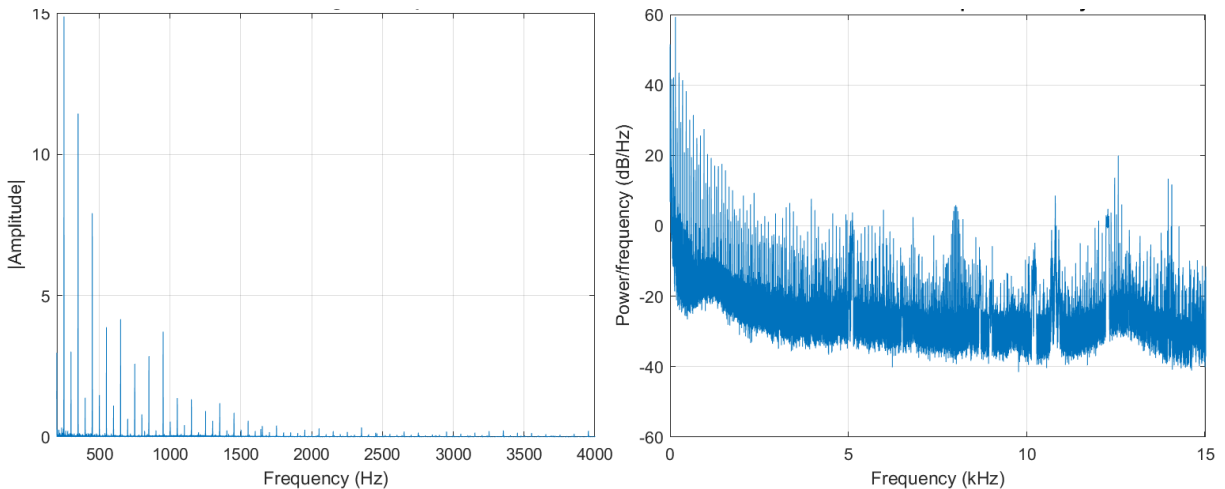


Figure 67 FFT and PSD Plot of the Raw Signal of Day 35 Brain Organoid

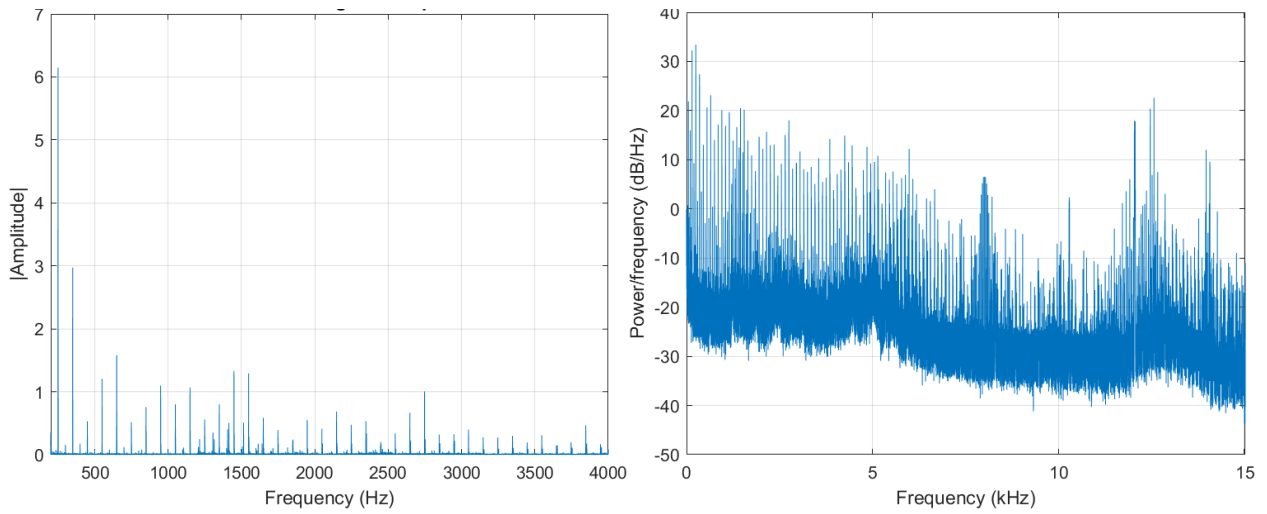


Figure 68 FFT and PSD Plot of the Raw Signal of Day 42 Brain Organoid Before Neurostimulation

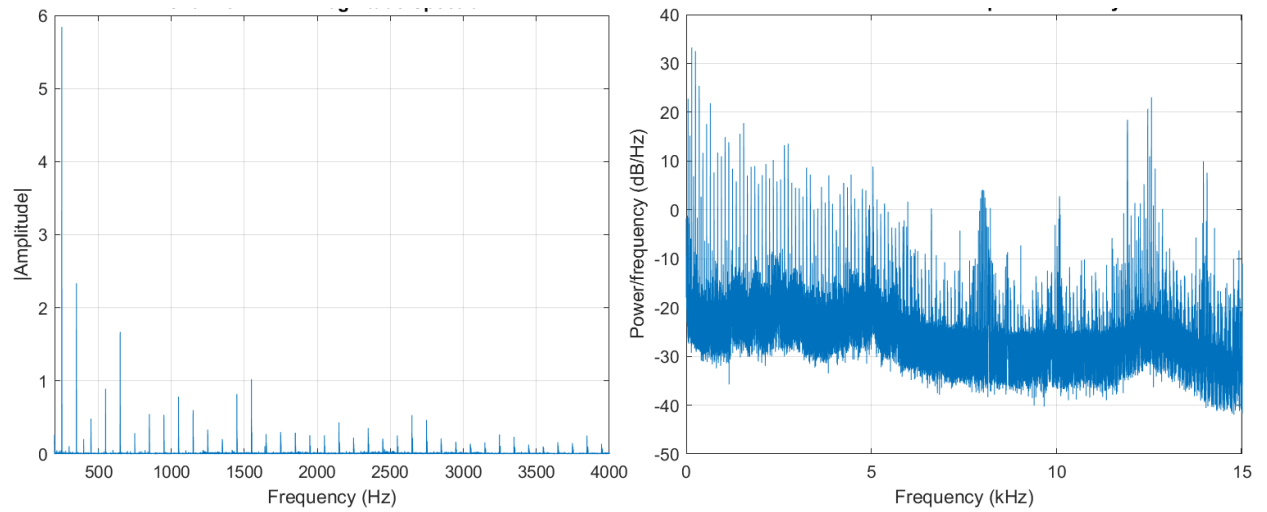
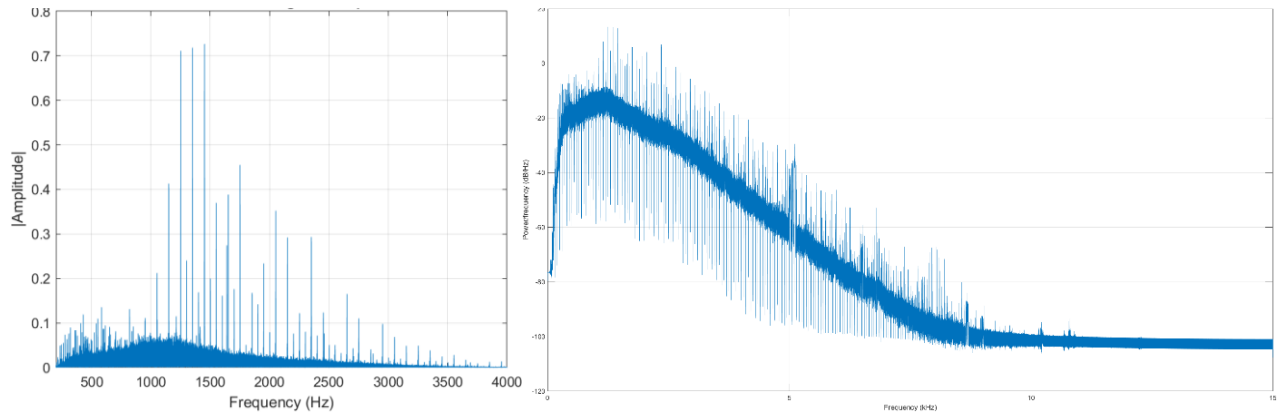


Figure 69 FFT and PSD Plot of the Raw Signal of Day 42 Brain Organoid After Neurostimulation

Based on these observations and standard practices for extracellular recordings, a bandpass filter in the range of 300–3,000 Hz was applied. This frequency range effectively captures the typical spectral characteristics of extracellular spike waveforms while suppressing irrelevant noise. A third-order Butterworth IIR filter was chosen for its computational efficiency. However, because IIR filters can introduce nonlinear phase distortion that may affect spike timing, the filter was applied using the zero-phase `filtfilt` method. This approach ensures the temporal fidelity of spike waveforms is preserved while maintaining the filter's efficiency. For the day 35 brain organoid recordings, an additional comb filter at 50 Hz and its resonance was applied to remove significant noise identified in the raw signal plot. The FFT plot of post-filtering day 35 recording revealed well-defined periodic components consistent with neural firing

patterns, while the PSD plots displayed a flattened noise floor outside the target band. Unlike the Day 35 signal, where filtering removed most unwanted frequencies outside the target range, the Day 42 signals still showed a broad spread of frequency components. This wider spectral profile likely reflects more complex and active neural firing. After NMDA stimulation, signal power increased across mid-to-high frequencies, indicating greater overall network activity. While the filter successfully removed irrelevant noise, the remaining wideband energy highlights the more dynamic and functionally mature state of the Day 42 brain organoid.



*Figure 70 FFT and PSD Plot of the Filtered Signal of Day 35 Brain Organoid*

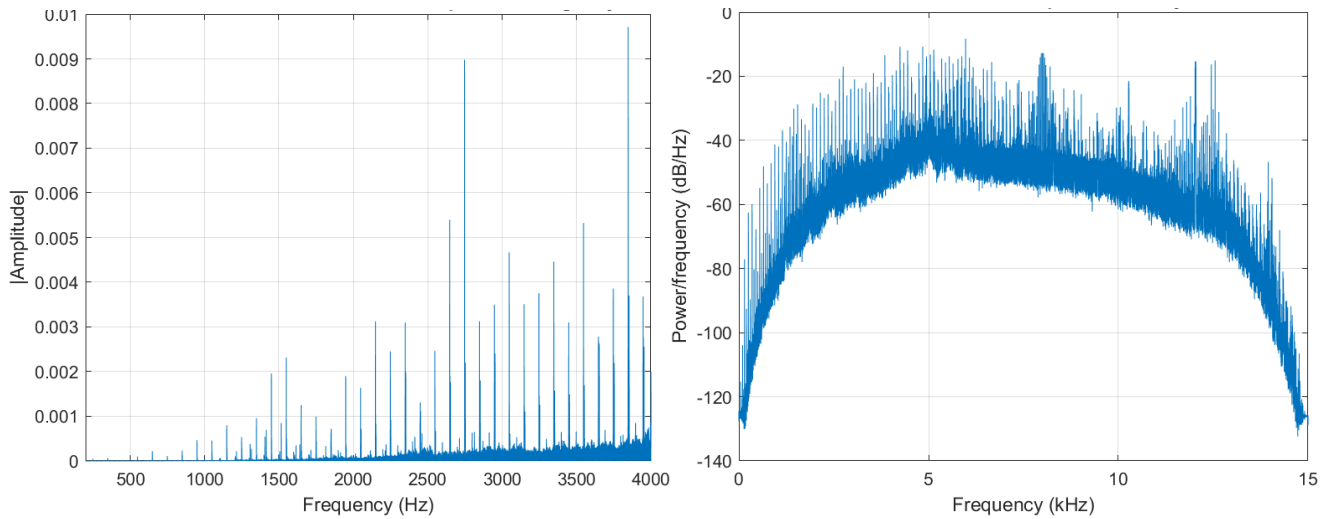


*Figure 71 FFT and PSD Plot of the Filtered Signal of Day 42 Brain Organoid Before Neurostimulation*

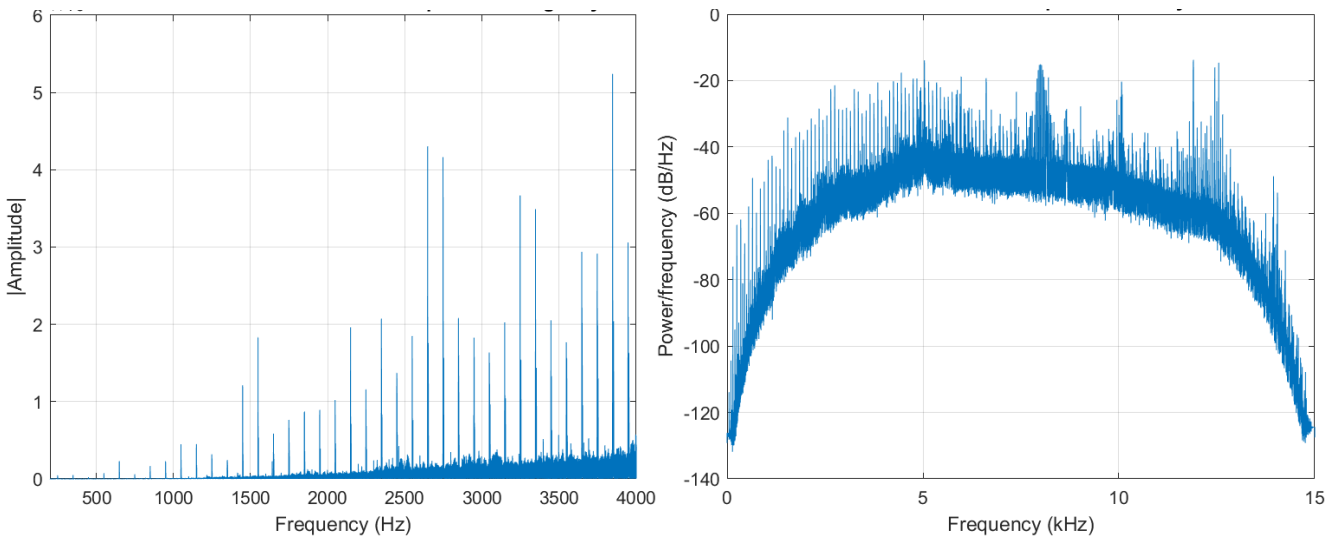


*Figure 72 FFT and PSD Plot of the Filtered Signal of Day 42 Brain Organoid After Neurostimulation*

Additionally, Common Average Referencing (CAR) was implemented for SiP dataset to reduce spatially correlated noise across electrodes and improve signal quality.

### 5.3.2 Multi-Unit Spike Detection

To extract spike events from electrophysiological recordings, two primary methods were implemented: a wavelet-based and a statistical thresholding method. The wavelet-based detection utilized the Continuous Wavelet Transform (CWT) in MATLAB, with biorthogonal Bior1.5 wavelets selected due to their resemblance to biphasic extracellular spike shapes, which are commonly observed in brain organoid recordings. The wavelet width was set between 0.4 and 0.8 milliseconds, aligning with the typical duration of transient spikes recorded by the MEAs system. The signal was then decomposed into multiple levels using dyadic wavelet decomposition, where each level divides the frequency and time resolution by half. At each level, the decomposed frequency bands were calculated using Equation (18)

$$\text{Level } D_j = \left[ \left\{ \frac{f_s}{2^{j+1}} \right\}, \left\{ \frac{f_s}{2^j} \right\} \right] \quad (18)$$

Where  $f_s$  = sampling rate

The number of scales of 6 was chosen to ensure coverage of the 300–3000 Hz bandwidth typically associated with neural spikes, given the 30,000 Hz sampling rate. The decomposition levels and corresponding frequency bands are summarized as follows:

Table 4 Frequency Range of Each Decomposition Level

Decomposition level	Frequency Range (Hz)
d1	7,500 - 15,000
d2	3,750 - 7,500
d3	1,850 – 3,750
d4	937 – 1,875
d5	468 - 937
d6	234 - 468

To enhance detection accuracy, a cost parameter of  $-0.12$  was applied in a Bayesian decision framework. A Bayesian decision threshold is derived using a Bayesian decision rule to determine whether a given wavelet coefficient originates from a spike or noise based on the likelihoods and priors of each class. The coefficient is classified as a spike if the posterior probability of it belonging to the spike class is greater than that of the noise class:

$$P(\text{spike} | c) > P(\text{noise} | c) \quad (19)$$

Applying Bayes' Theorem, this condition becomes:

$$\frac{P(\text{spike})P(c|\text{spike})}{P(c)} > \frac{P(\text{noise})P(c|\text{noise})}{P(c)} \quad (20)$$

$$\frac{P(c|\text{spike})P(\text{spike})}{P(c|\text{noise})P(\text{noise})} > 1 \quad (21)$$

Here  $P(\text{spike})$  and  $P(\text{noise}) = 1 - P(\text{spike})$  denote the prior probabilities of spikes and noise, respectively. To simplify the comparison, a log-likelihood ratio test is applied:

$$\log \frac{P(c|\text{spike})}{P(c|\text{noise})} > \log \frac{P(\text{noise})}{P(\text{spike})} \quad (22)$$

Assuming both spike and noise distributions follow Gaussian distributions with equal variance  $\sigma^2$  and that the noise has a mean of zero while the spike class has a non-zero mean  $\mu_j$ , the probability densities become:

$$P(c | \text{class}) = \frac{1}{\sqrt{2\pi\sigma_j^2}} \exp\left(-\frac{(c-\mu_j)^2}{2\sigma_j^2}\right) \quad (23)$$

The ratio of the likelihoods simplifies to:

$$\frac{P(c|spike)}{P(c|noise)} = \exp\left(\frac{-(c-\mu_j)^2 + c^2}{2\sigma_j^2}\right) = \exp\left(\frac{2c\mu_j - \mu_j^2}{2\sigma_j^2}\right) \quad (24)$$

Taking the logarithm:

$$\log\left(\frac{P(c|spike)}{P(c|noise)}\right) = \frac{c\mu_j}{\sigma_j^2} - \frac{\mu_j^2}{2\sigma_j^2} \quad (25)$$

Thus, the decision rule becomes:

$$\frac{c\mu_j}{\sigma_j^2} - \frac{\mu_j^2}{2\sigma_j^2} > \log\left(\frac{P(noise)}{P(spike)}\right) \quad (26)$$

The Bayesian decision threshold is given by:

$$c > \frac{\mu_j}{2} + \frac{\sigma_j^2}{\mu_j} \log\left(\frac{P(noise)}{P(spike)}\right) + L \quad (27)$$

This threshold determines whether a coefficient is more likely to originate from a spike or noise based on both statistical properties of the data and prior assumptions.

In the second approach, spike detection was performed using a thresholding method based on the MAD of the recorded signal. A fixed threshold, commonly set at 3, 4, or 5 times the MAD, was applied to identify spike events. Since neuronal spikes typically appear as sharp negative deflections due to their polarity, the algorithm focused on detecting negative-going peaks, which also helped distinguish them from background noise that is generally lower in amplitude and more symmetric. To avoid redundant detections of the same spike, a 1 ms refractory period was imposed, reflecting the minimum inter-spike interval typically observed in spontaneous activity from brain organoids.

For each recording, several visualizations are generated to evaluate the performance of both detection methods. These include:

- Overlays of 50 ms sampled spikes along with averaged spike waveforms for selected electrodes.
- Sample voltage traces from nine electrodes, highlighting detected spikes.

Each MEAs recording is systematically reviewed using these plots to compare the performance of both methods and validate the accuracy of spike detection.

### **5.3.3 Spike Feature Extraction**

Following spike detection, a range of quantitative features was extracted to characterize the spiking activity recorded across electrodes. These included both basic spike metrics and higher-order network-level features, summarized below.

#### **5.3.3.1 Basic Spike Features**

- Spike Frequency: This metric reflects the firing rate of individual electrodes, calculated as the number of detected spikes divided by the total duration of the recording. It provides a direct measure of how frequently neurons fire over time.
- Number of Active Channel: To differentiate between functionally active and inactive electrodes, channels were considered active if their firing rate exceeded a defined threshold. For brain organoid datasets, a threshold of 0.01 Hz was used.
- Mean and Median Firing Rates: These summary statistics were computed for each recording to allow comparison of overall neural activity across experimental conditions or developmental time points.

#### **5.3.3.2 Higher-Order Features: Network Burst Properties**

Network bursts represent periods of synchronized firing across multiple electrodes and were defined as events with at least 5 spikes distributed across a minimum of 2 active channels. The following characteristics were extracted to describe network burst dynamics:

- Burst Rate: Number of network bursts per minute of recording.
- Participating Channels: Average number of electrodes contributing to each burst.
- Burst Duration:
  - ISI: Average time between spikes both within bursts and between separate bursts, measured in milliseconds.
  - Burst Interval Variability: Coefficient of variation in the timing between inter-network bursts.
  - Single-Channel Burst Inclusion: Proportion of bursts detected on individual channels that occurred concurrently with larger network-wide bursts.

All extracted features were automatically visualized through scatterplots, which included group-wise means, standard error of the mean (SEM), and distribution curves for easier comparison.

Additionally, spike frequency patterns were presented using raster plots and MEAs heatmaps as well to provide a clear spatial and temporal overview of neural activity across the network.

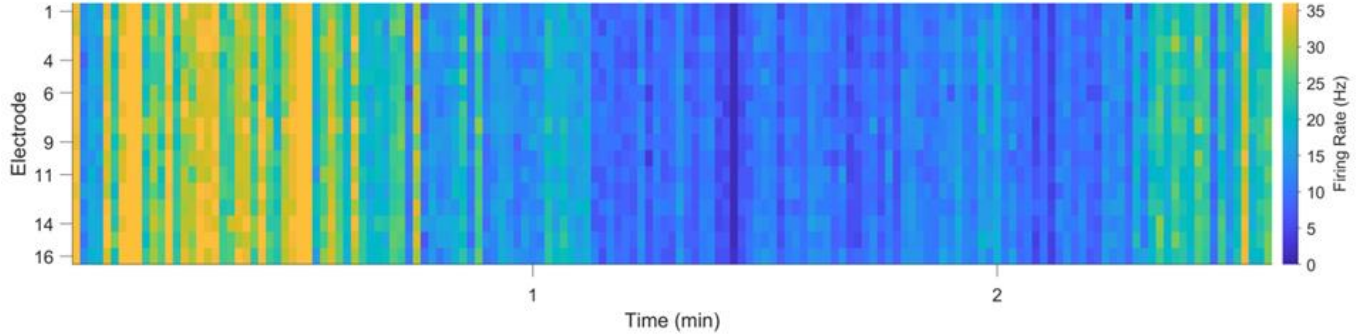


*Figure 73 A Raster Plot of Day 35 Brain Organoid*

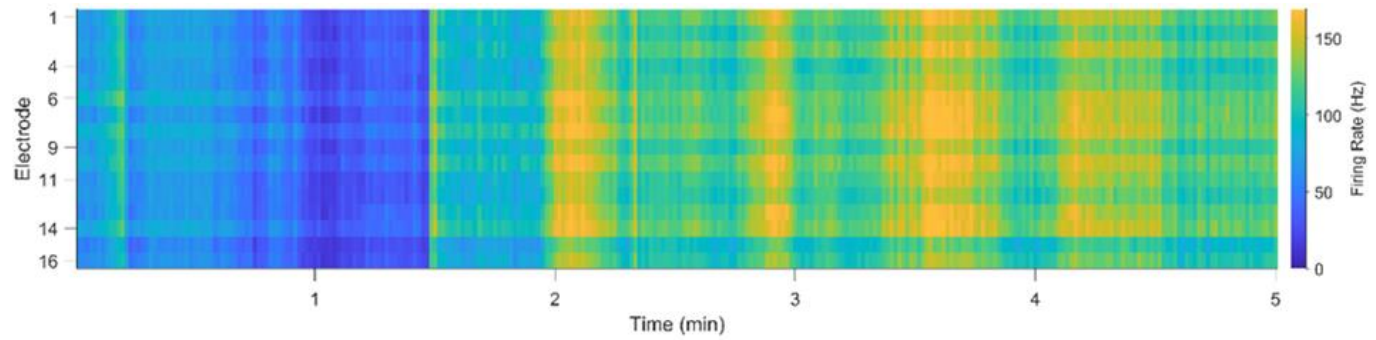


*Figure 74 Raster Plots of Day 42 Brain Organoid Before Neurostimulation*

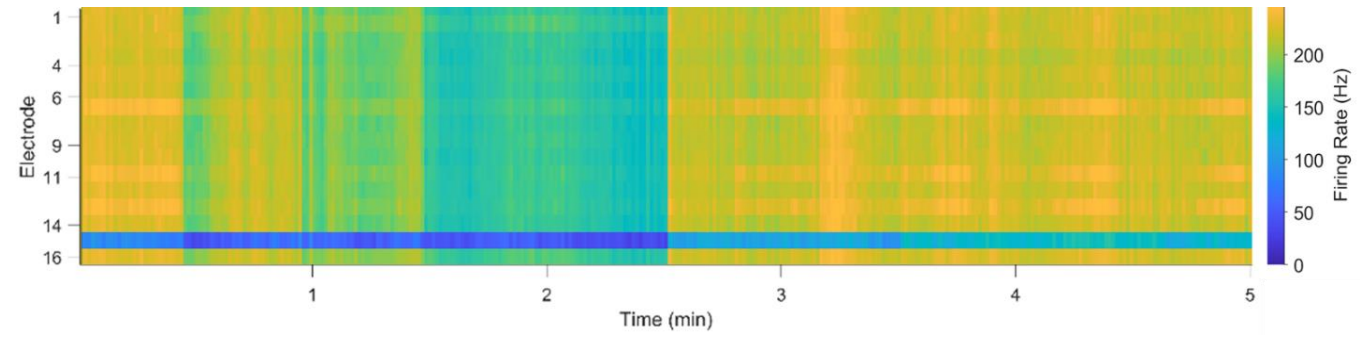


*Figure 75 Raster Plots of Day 42 Brain Organoid After Neurostimulation*

### 5.3.4 Functional Connectivity Inference

To assess functional connectivity between neurons, spike train synchrony was assessed using the STTC, a metric designed to quantify the temporal correlation between two spike trains

across electrode pairs. Analyses were conducted using lag intervals of 10 ms, 25 ms, and 50 ms, to explore the impact of different temporal windows on connectivity detection. For specific datasets from hiPSC-derived organoids and monolayer cultures, a 25 ms lag was selected as it provided optimal sensitivity to their network activity patterns.

To determine the statistical significance of the observed connectivity, a probabilistic thresholding approach was applied. For each electrode pair, one spike train was circularly shifted 200 times, and STTC values were recalculated for each iteration. This generated a distribution of STTC values under the assumption of no temporal structure (null distribution), representing chance-level synchrony. A connection was considered significant if the actual (unshifted) STTC exceeded the 95th percentile of this shuffled distribution, indicating a low probability of the result occurring by chance. The number of circular shifts (set to 200) was adjustable within the MEA-NAP pipeline, offering flexibility based on computational resources or dataset complexity. Following significance testing, only statistically validated connections were retained and stored into a weighted adjacency matrix, which included only the electrode pairs with statistically validated interactions. These matrices were subsequently used for network analysis and computation of topological metrics.

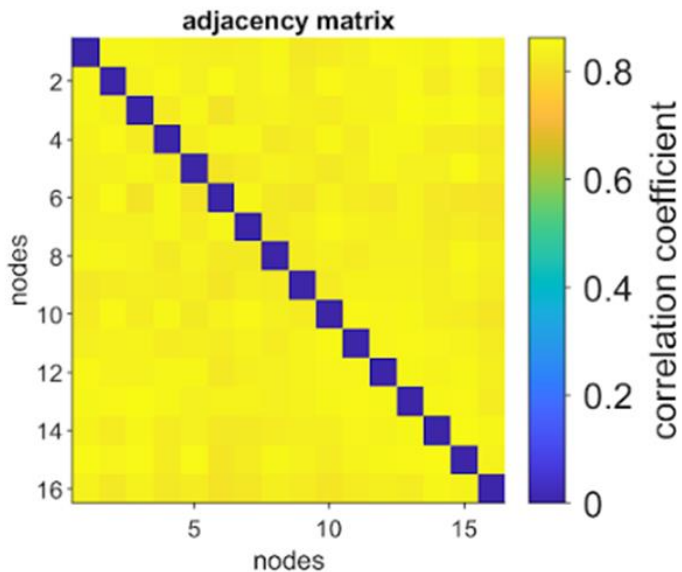


*Figure 76 A Weighted Adjacency Matrix of Day 35 Brain Organoid*

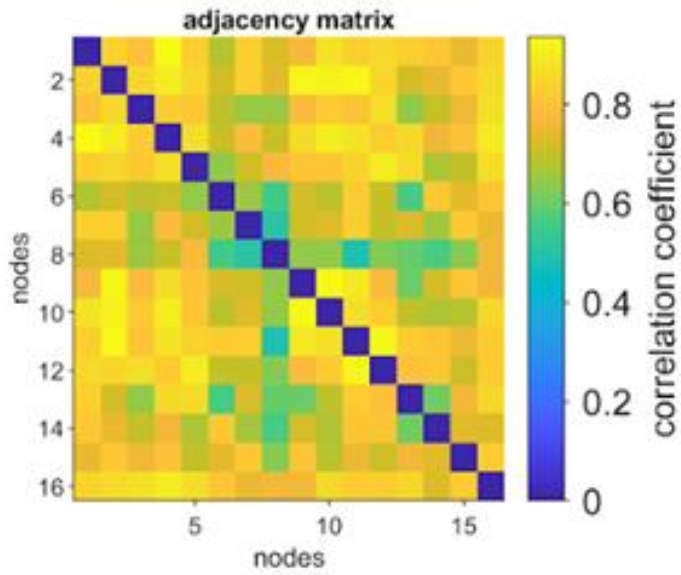


*Figure 77 A Weighted Adjacency Matrix of Day 42 Brain Organoid Before Neurostimulation*

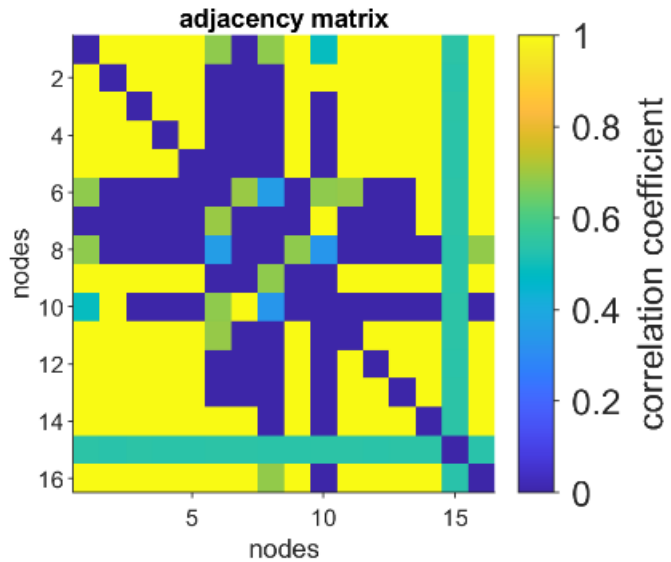


*Figure 78 A Weighted Adjacency Matrix of Day 42 Brain Organoid After Neurostimulation*

To visually inspect the effectiveness of the selected lag interval, histograms of sorted STTC values were generated. These plots showed that peak correlations flattened with increasing lag, while mean values remained below the maximum, confirming the appropriateness of the chosen temporal window for detecting functionally relevant synchrony.

### 5.3.5 Network Structure and Node Role Characterization

#### 5.3.5.1 Graph-Theoretical Analysis of Functional Connectivity

After identifying significant functional connections between electrodes, the structure and organization of the neuronal network were examined using graph-theoretical approaches. First, functional connectivity graphs were generated by treating each electrode as a node and representing significant connections between pairs of electrodes as weighted edges, where edge weights were based on the corresponding STTC values.

The resulting weighted graphs were analyzed using the Brain Connectivity Toolbox (BCT) in MATLAB, a standard toolkit in the field of network neuroscience, with the aim to quantify both local and global properties of neuronal communication within the system. The local metrics were evaluated to assess communication efficiency within small neighborhoods of the network while the global features were calculated to characterize overall information flow and integration across the entire network. A list of all metrics and a description for each network metric is provided in Table 3. All normalization procedures used null models that preserved the original network's degree distribution. This ensured accurate comparisons and preserved essential structural properties.

*Table 5 Network Metric Definitions [45]*

Basic Network Metrics	
Node Degree	The total number of connections linked to each node.
Edge Weight	The strength of connectivity derived from the STTC value.
Node Strength	The sum of all edge weights connected to a node.
Network Size	The number of active nodes (electrodes with activity).
Network Density	The ratio of actual connections to all possible connections in the network.

Local Network Properties	
Local Efficiency	The efficiency of information transfer within a node's neighborhood (at the level of individual nodes). Prior to calculation, all edge weights were normalized to a range of 0–1 using the weight_conversion function in BCT.
Modularity	The presence of subnetworks or communities. First, modular decomposition was performed using the Louvain algorithm, followed by consensus clustering to stabilize community detection.
<ul style="list-style-type: none"> <li>• Modularity Scores</li> </ul>	A measure of how well the network divides into modules.
<ul style="list-style-type: none"> <li>• Number of Modules</li> </ul>	The total number of distinct communities or subnetworks within the network.
<ul style="list-style-type: none"> <li>• Within-Module Z-Score</li> </ul>	A measure of how strongly a node is connected to others within its own module, calculated using the module_degree_zscore function.
<ul style="list-style-type: none"> <li>• Affiliation Vector</li> </ul>	A vector containing the number of the module membership of each node.
Global network properties	
Global Efficiency	The average efficiency of information exchange between all pairs of nodes in the network.
Betweenness Centrality	Number of times a node lies on the shortest path between other nodes, identifying key hub-like elements. This metric was normalized using the formula: $BC_{norm} = \frac{BC}{(N-1)(N-2)}$ where N is the total number of nodes.
Participation Coefficient	A measure of how evenly a node connects to different modules. To compute this, participation scores were

	normalized by comparing against 100 randomized null models with preserved degree distribution.
Clustering Coefficient	A probability Indicates how densely connected nodes are and how easily information travels across the network. It was normalized using a lattice-based null model that generated over 10,000 iterations.
Characteristic Path Length	The minimum number of edges required for the shortest path between all pairs of nodes. This was normalized using 5,000 null models preserving the degree distribution.
Small-World Metrics	The resulting values ranged from $-1$ (purely lattice-like) to $+1$ (completely random), with values near zero indicating a small-world structure—typically associated with efficient information processing in biological networks.
<ul style="list-style-type: none"> <li>• s-coefficient</li> </ul>	Ratio of the normalized clustering coefficient to normalized path length.
<ul style="list-style-type: none"> <li>• u-coefficient</li> </ul>	Difference between normalized path length and normalized clustering coefficient.

The participation coefficient was computed using a method that compares each network to 100 randomly generated null models with the same degree distribution, allowing normalization of participation scores. Similarly, the clustering coefficient was normalized using a lattice-based null model over 10,000 iterations to maintain degree distribution. The characteristic path length was normalized against 5,000 randomly generated null models with preserved degree distribution.

For day 35 brain organoid recording, network metrics could not be plotted, likely due to an insufficient number of significant events or inadequate network connectivity in the recorded data. This may suggest the need for further parameter adjustments or alternative analytical methods that better capture the network dynamics at this stage.

However, day 42 brain organoid recording exhibited high node degrees ( $\approx 15$ ) and elevated edge weights, reflecting strong functional coupling. Node strength remained

high, while high local efficiency and participation coefficients indicated efficient information flow and distributed intermodular communication, suggesting a well-integrated and synchronized neural population. Notably, betweenness centrality and within-module z-scores were low across all replicates, implying decentralized communication without dominant hubs. Following neurotransmitter stimulation, changes in the network metrics were also analyzed and compared.

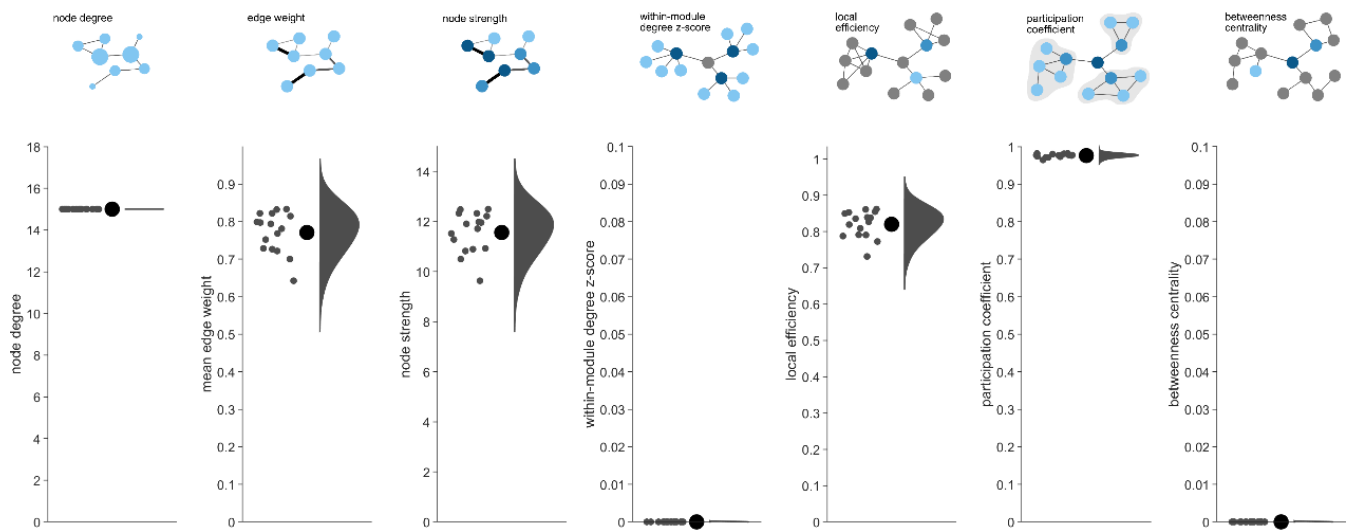


*Figure 79 Network Metrics of Day 42 Brain Organoid Networks Before Neurostimulation*

Following NMDA stimulation, graph-theoretical analysis revealed notable changes in multiple network metrics. The average node degree, edge weight, and node strength further varied, consistent with a remained high local efficiency and participation coefficients. Additionally, there was a significant increase in within-module Z-score, indicating stronger intra-modular connectivity and the emergence of more central nodes within each community. Betweenness centrality also increased slightly, implying that a small number of nodes began to serve as bridges between modules. These shifts point toward a network that becomes more structured and functionally integrated, enhancing both local specialization and broader intermodular signaling.

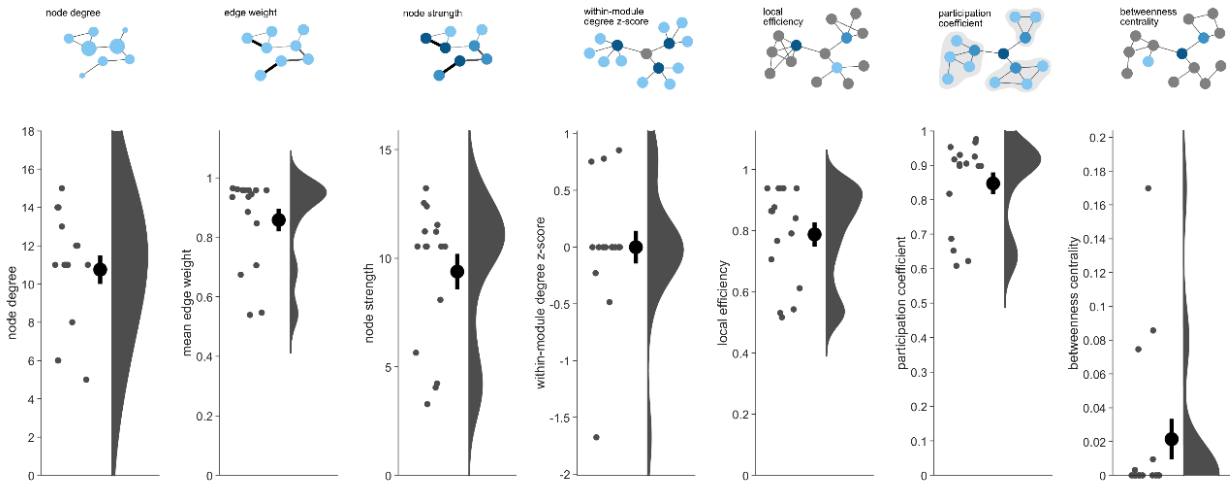
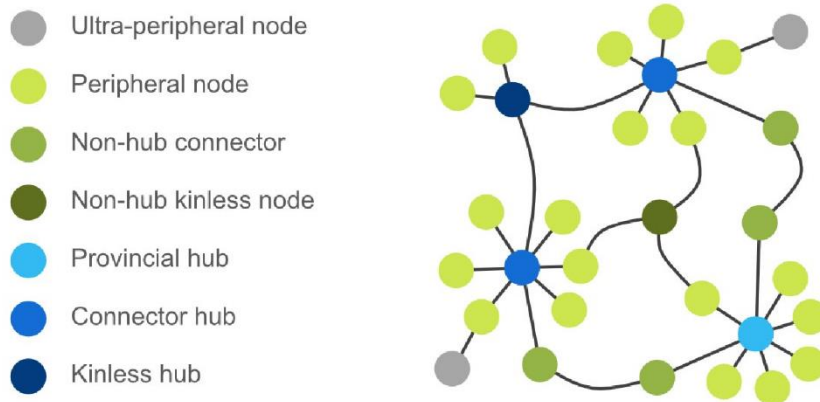


Figure 80 Network Metrics of Day 42 Brain Organoid Networks After Neurostimulation.

### 5.3.5.2 Node Role Classification Using Node Cartography

To identify and characterize the functional roles of individual nodes (electrodes) within the inferred functional connectivity networks, a node cartography framework was implemented. This method evaluates the network roles of each node based on two metrics: the participation coefficient, which quantifies how a node connects across different modules (inter-module connectivity), and the within-module Z-score, which reflects the node's centrality within its own module (intra-module connectivity). These two features were computed for all nodes in the dataset and visualized as a density-based reference landscape. Node role classification was performed using a threshold-based clustering approach. Initially, nodes were divided into hub and non-hub groups based on their within-module Z-scores, using a Z-threshold to separate central and non-central nodes. Within each group, k-means clustering was then applied to the participation coefficient values to further classify nodes into finer categories. Specifically, non-hubs were classified as peripheral, non-hub connectors, or non-hub kinless nodes, while hubs were divided into provincial hubs, connector hubs, and kinless hubs, depending on their participation across modules. The clustering used minimum, maximum, and midpoint values of Participation Coefficient within each Z-based category to guide separation boundaries. Based on this landscape, nodes in each recording were classified into predefined categories: ultra-peripheral nodes, peripheral nodes, non-hub connectors, non-hub kinless nodes, provincial hubs, connector hubs, or kinless hubs. These classifications were made according to the functional role of each node within the network, as shown in

the provided Table 6. Each class represented a distinct functional role, with specific contributions to both local and global network organization.



*Figure 81 Schematic Representation of Node Role Classifications in Functional Connectivity Network [45]*

*Table 6 Functional Role Definitions Based on Node Classifications [45]*

Node Classifications	Functional Roles
Non-Hub Peripheral	Local connectors within their respective modules
Non-Hub Connector	Non-central nodes linking across a few modules
Non-Hub Kinless	Nodes with connections across many modules but not central to the network.
Provincial Hub	Local connectors with strong influence within their respective modules
Connector Hub	Central nodes linking across a few modules
Kinless Hub	Central nodes with connections across many modules

The node classifications for each recording were then compared across experimental conditions, including different developmental stages and STTC lag parameters, to investigate changes in network architecture and connectivity roles over time. Prior to stimulation, the density landscape of the Day 42 brain organoid reveals that most nodes fall within the non-hub kinless category. This suggests widespread but non-centralized intermodular connectivity, where nodes are distributed across several modules without exerting strong local or global influence. Following NMDA stimulation, its density landscape showed a clear shift in node distribution and functional roles. Unlike the pre-stimulation state, which was dominated by non-hub kinless nodes, the post-

stimulation network exhibited a broader range of node types. Several nodes transitioned into peripheral, non-hub connector, and even hub categories, including the appearance of provincial and kinless hubs. The emergence of hubs indicates the formation of structurally influential nodes, contributing to improved information routing and functional integration across the organoid.

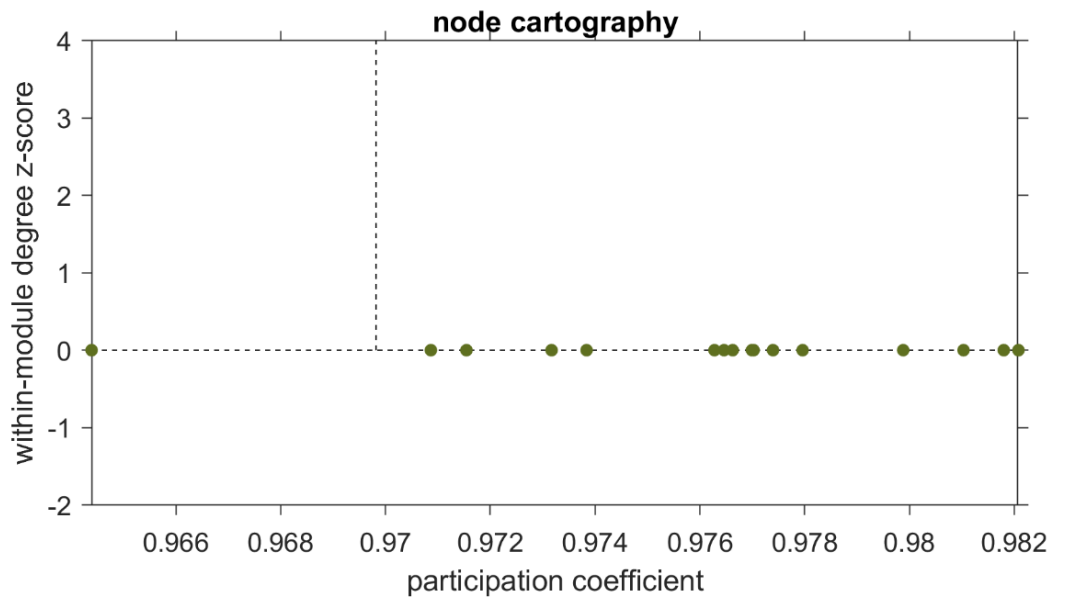


*Figure 82 A Density Landscape of Day 42 Brain Organoid Networks Before Neurostimulation*

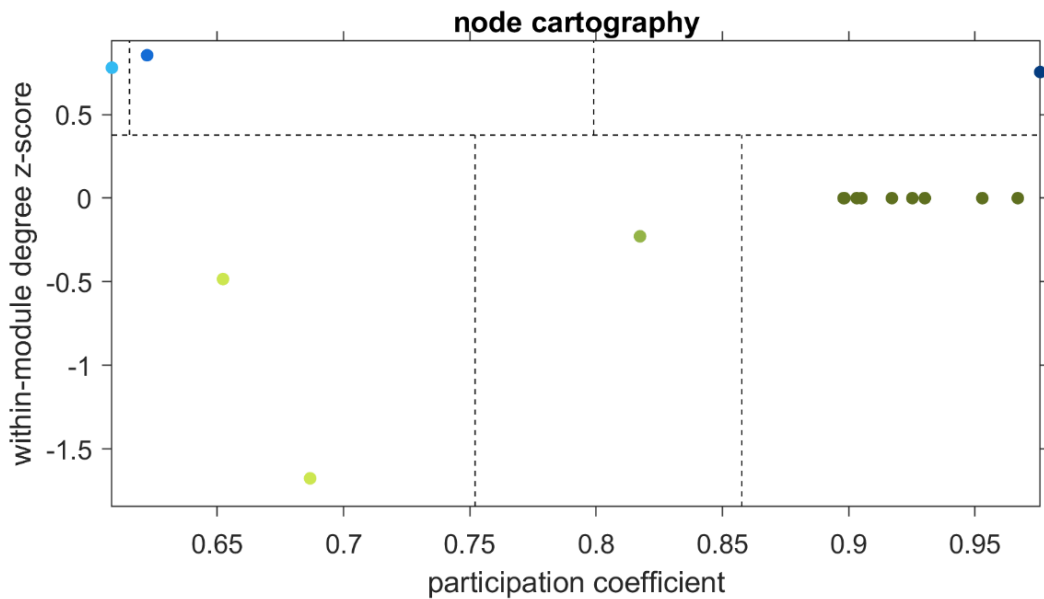


*Figure 83 A Density Landscape of Day 42 Brain Organoid Networks After Neurostimulation*

### 5.3.6 Validation of the Pipeline with Real Experimental Data

In addition to the synthetic datasets with artificially rewired network versions used for benchmarking in the literature review, the MEA-NAP pipeline was further validated using a real experimental dataset. This dataset, consisting of brain organoid data from day 7 to day 35, is available online. The pipeline was tested on this dataset, and its performance in detecting meaningful network changes successfully aligned with the ground truth, demonstrating its effectiveness in analyzing real-world experimental data.

### 5.3.7 Analysis of Functional Maturation and Network Reorganization in Brain Organoids Across Development and Neurostimulation

#### 5.3.7.1 Developmental Differences in Neuronal Activity and Connectivity Between Day 35 and Day 42 Brain Organoids

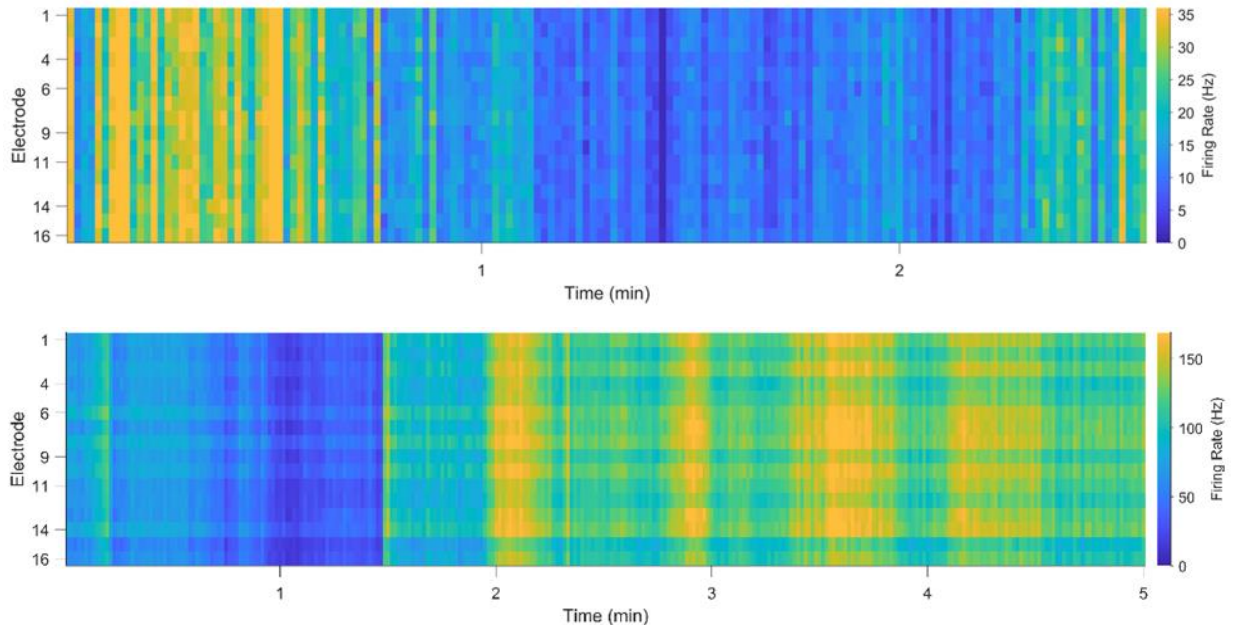


Figure 84 Raster plots of Day 35 and Day 42 Brain Organoid

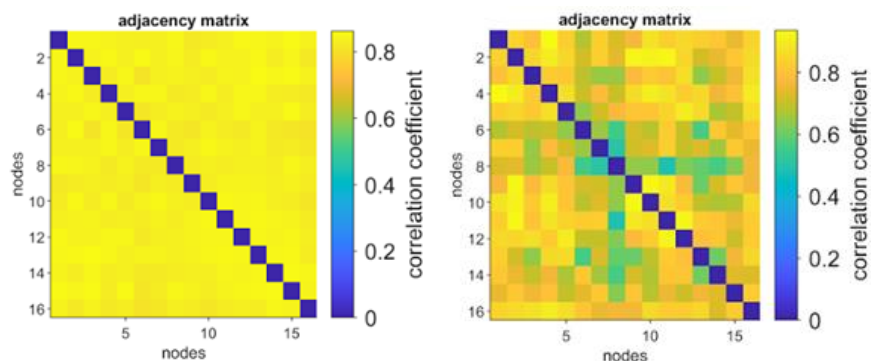


Figure 85 Weighted Adjacency Matrices of Day 35 (Left) and Day 42 (Right) Brain Organoid

A comparative analysis of firing rate heatmaps and adjacency matrices reveals distinct patterns of neuronal activity and network connectivity between Day 35 and Day 42 brain organoids. As shown in the raster plot for Day 35, the overall firing activity remains relatively sparse, with low-frequency spikes distributed across electrodes. Correspondingly, the adjacency matrix indicates uniformly high correlation values across most electrode pairs, but with limited variability, suggesting a relatively homogeneous and possibly immature network structure with less differentiated functional connections.

In contrast, the Day 42 raster plot displays a significantly higher firing rate across multiple electrodes, particularly between 2–5 minutes, indicating a substantial increase in spontaneous neural activity. The corresponding STTC-based adjacency matrix shows greater heterogeneity in pairwise correlations, reflecting the occurrence of more complex and diverse connectivity patterns. These changes are indicative of network maturation over time.

One plausible explanation for this developmental progression is the increased expression of synaptic and neuronal maturation markers, such as PSD95, MAP2, Synaptophysin, and potentially NeuN, reported at later stages of organoid development. The upregulation of these proteins at Day 42 is consistent with enhanced synaptogenesis and dendritic arborization, which likely contribute to the observed increase in spike activity and more differentiated functional connectivity. This supports the interpretation that the electrophysiological profile of Day 42 organoids reflects a more mature and active neural network compared to Day 35.

### 5.3.7.2. Changes in Neuronal Activity and Network Connectivity in Day 42 Brain Organoids Following NMDA Stimulation

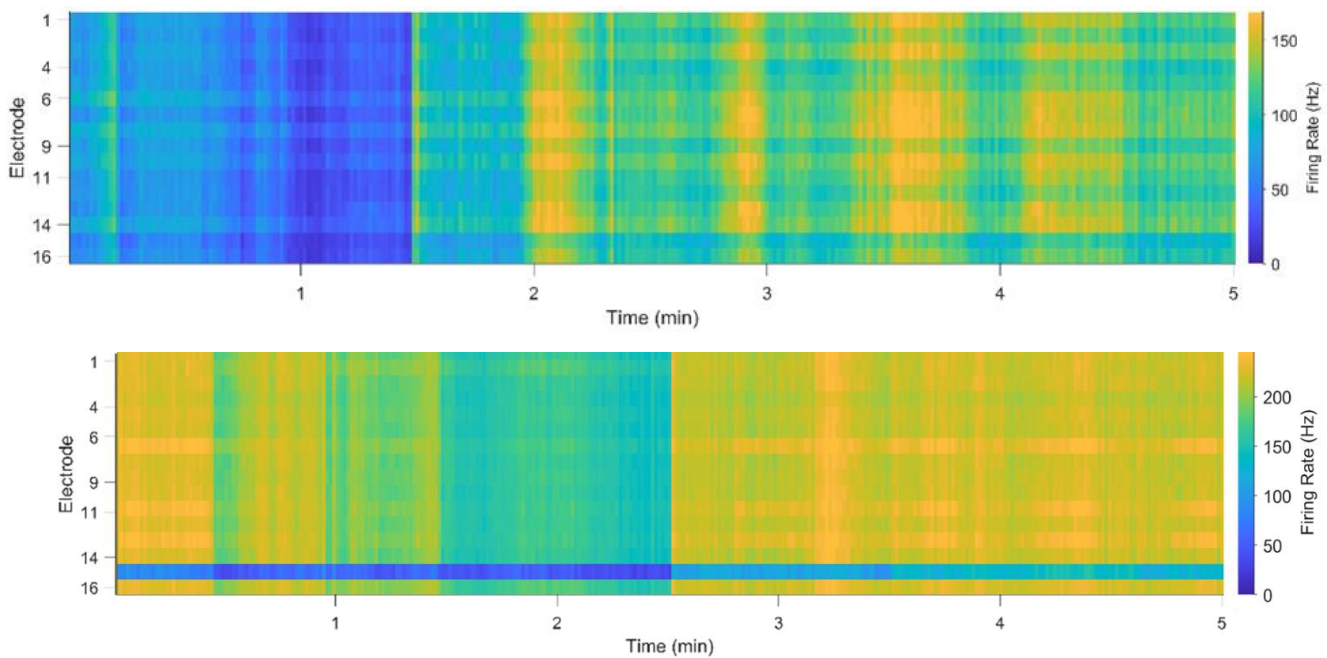


Figure 86 Raster plots of Day 42 Brain Organoid Before (Left) and After (Right) Neurostimulation

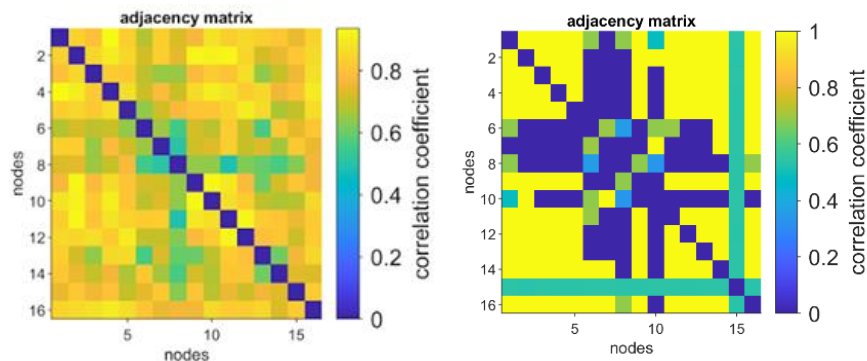


Figure 87 Weighted Adjacency Matrices of Day 42 Brain Organoid Before (Left) and After (Right) Neurostimulation

Following NMDA stimulation, the firing activity of Day 42 brain organoids showed significant increase in intensity and temporal organization. As illustrated in the raster plots, the post-stimulation condition exhibited more consistent and widespread activation across electrodes compared to the pre-stimulation state, which showed sparser and irregular firing patterns. This enhancement in spiking behavior suggests increased excitability and network responsiveness induced by NMDA. Correspondingly, the weighted adjacency matrices revealed clear changes in the network's connectivity pattern

after NMDA stimulation. Before stimulation, the connections between electrodes were uneven and loosely organized, reflecting a less structured network. After stimulation, the matrix showed clearer modular separation and stronger connections between nodes, indicating the formation of more organized functional groups. This suggests that NMDA stimulation promotes not only higher neuronal activity but also greater functional integration across the network, reflecting a more cohesive and globally connected state.

### 5.3.7.3 NMDA Stimulation Induces Distributed Functional Connectivity Across Brain Organoid Networks

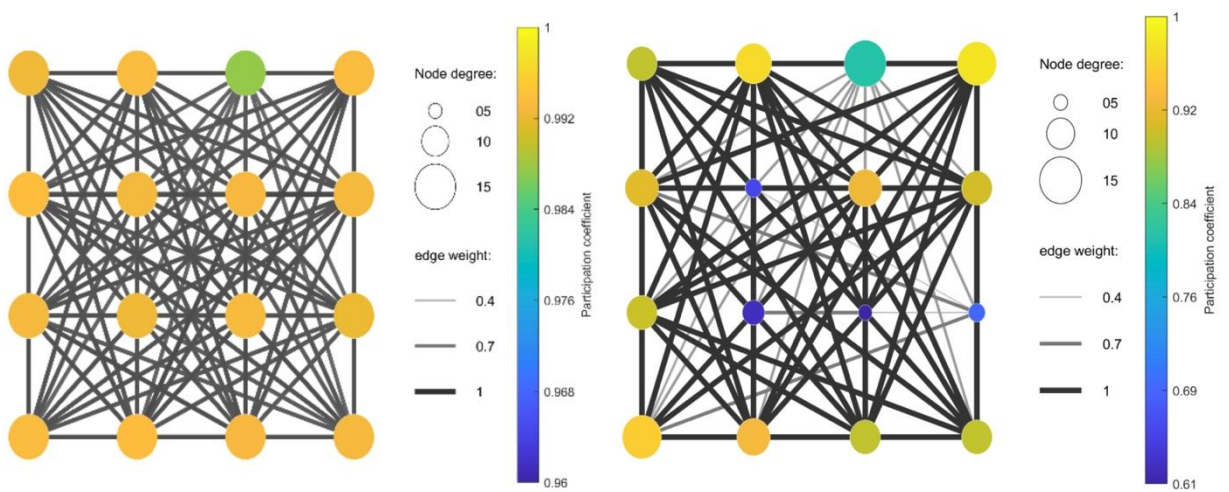


Figure 88 Changes in Functional Connectivity of Day 42 Brain Organoid Networks Before (Left) and After (Right) Neurostimulation.

The effect of neurostimulation on the functional connectivity of brain organoid networks was assessed by comparing the network structure before and after stimulation. Prior to neurostimulation, the connectivity within the brain organoid was dense and uniform across all replicates (left panel), as evidenced by the consistent distribution of node degrees and the strong, even connections between nodes. The yellow-colored nodes demonstrated nearly identical participation coefficients, which indicated a well-balanced integration of network activity throughout the entire network.

Following neurostimulation, the connectivity pattern of the network became less uniform (right panel). There was a noticeable shift in the distribution of node degrees, with certain nodes exhibiting higher participation coefficients, suggesting a more differentiated network structure. The edges between nodes also became more varied. The

observed shift from a dense and uniform to a less uniform connectivity pattern suggests that neurostimulation may induce a process of selective functional reorganization within the network. This reorganization could be attributed to changes in synaptic plasticity, where the stimulation selectively enhances certain neural pathways while potentially inhibiting others, leading to a more modular and specialized network. These findings highlight the ability of neurostimulation to influence the topological organization of neural networks, potentially enhancing the functional integration and specificity of brain organoid systems.

#### 5.3.7.4 Impact of Neurostimulation on Directional Connectivity and Node Cartography of in Brain Organoids

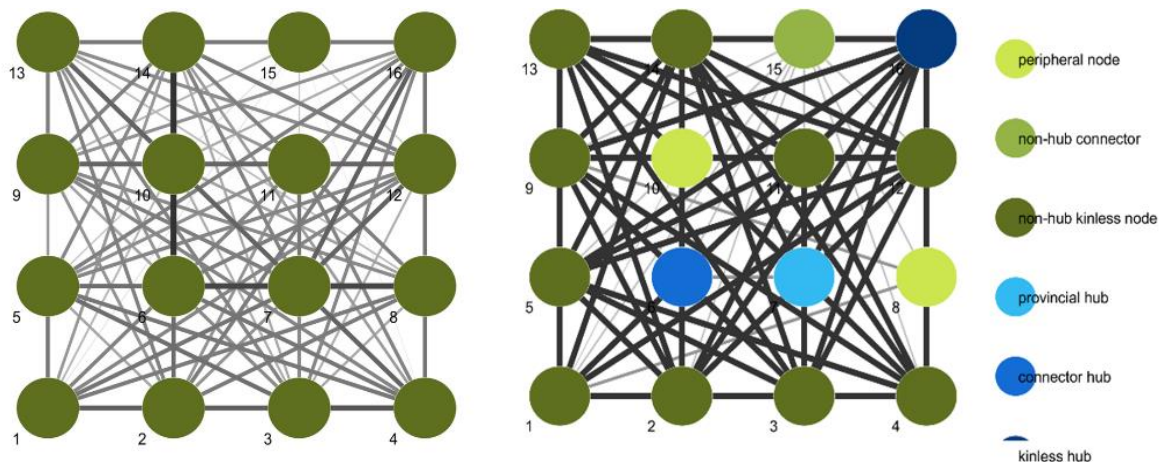


Figure 89 Node Cartography of Day 42 Brain Organoid Networks Before (Left) and After (Right) Neurostimulation

In the pre-neurostimulation network (left panel), all nodes were classified as non-hub kinless nodes, which had few or no connections to central hubs. These nodes were distributed across various regions of the network, contributing minimal influence on the overall connectivity. As a result, the network exhibited a relatively low centrality, with weak local connections and limited integration between nodes. This configuration suggests a decentralized structure, resembling early-stage neural development with sparse and selective communication pathways.

In contrast, the post-neurostimulation network (Figure 89 right panel) showed a more structured and interconnected organization, with the formation of central nodes, including provincial hubs, connector hubs, and kinless hubs. These central hubs played a

more significant role in connecting multiple distinct modules, enhancing the overall connectivity and functional integration of the brain organoid. This reorganization from a network dominated by non-hub kinless nodes to one with more central hubs suggests that neurostimulation enhanced the functional connectivity of the network by strengthening key pathways and fostering the development of dominant central nodes. Overall, these results indicate that neurostimulation can induce a transformation from a less integrated to a more organized network, resembling the progressive stages of neural network development.

## **CHAPTER VI**

### **CONCLUSION**

In this study, we successfully generated cerebral organoids from human induced pluripotent stem cells with a 100% success rate ( $n = 8$ ), approximately 40% higher than standard protocols. Morphologically, the organoids exhibited key features of early human brain development, including a bubbling surface, optically translucent edges, and a dense necrotic core, indicative of neuroepithelial expansion and internal compartmentalization. Immunohistochemical staining further confirmed progressive neural maturation, as indicated by the increased expression of neuronal and synaptic markers, including PAX6, MAP2, SYN, and PSD95, between Day 35 and Day 42. These combined morphological and molecular characteristics support the suitability of the organoids as a physiologically relevant *in vitro* model for electrophysiological studies of human brain-like networks.

In parallel, efforts were made to utilize the Brain-Computer Interface Laboratory's System in Package for electrophysiological recording, however, the system exhibited poor data acquisition performance due to a significantly low signal-to-noise ratio of 0.107 dB, indicating that background noise overwhelmed the neural signals. In contrast, the custom-fabricated 16-channel microelectrode arrays demonstrated reliable signal detection when paired with the Intan RHS Stim/Recording System, a gold standard for miniature electrophysiology. Consequently, the Intan system was adopted as the primary platform and successfully enabled non-invasive and real-time acquisition of spontaneous neural activity from the cerebral organoids.

Electrophysiological recordings obtained using the Intan system were further analyzed through the Microelectrode Array Network Analysis Pipeline to assess the functional organization of neural activity within the cerebral organoids. On Day 35, minimal spiking and burst activity were detected. By Day 42, organoids exhibited increased overall activity; however, distinct functional microcircuits and node-specific roles only emerged following stimulation with neurotransmitter, NMDA. Post-stimulation analysis revealed enhanced burst frequency, greater variability in participation coefficients, and directional functional connectivity as shown by node cartography.

These findings support the feasibility of using cerebral organoids as a living neural platform for studying dynamic network behaviors relevant to brain-inspired computational systems.

## REFERENCES

- [1] R. Raman, D. Pattnaik, L. Hughes and P. Nedungadi, "Unveiling the dynamics of AI applications: A review of reviews using scientometrics and BERTopic modeling," *Journal of Innovation & Knowledge*, vol. 9, no. 3, p. 100517, Jul. 2024.
- [2] C. D. Schuman et al., "Opportunities for neuromorphic computing algorithms and applications," *Nature Computational Science*, vol. 2, no. 1, pp. 10-19, Jan. 2022.
- [3] J. Kim, M. Ricci and T. Serre, "Not-So-CLEVR: learning same-different relations strains feedforward neural networks," *Interface focus*, vol. 8, no. 4, Aug. 2018.
- [4] "Healthy diet," World Health Organization, 2020 April 29. [Online]. Available: <https://www.who.int/news-room/fact-sheets/detail/healthy-diet>. [Accessed 29 September 2024].
- [5] M. E. Raichle and D. A. Gusnard, "Appraising the brain's energy budget," *Proceedings of the National Academy of Sciences*, vol. 99, no. 16, pp. 10237-10239, Aug. 2002.
- [6] G. C. Team, "Hewlett Packard Enterprise ushers in new era with world's first and fastest exascale supercomputer "Frontier" for the U.S. Department of Energy's Oak Ridge National Laboratory," Hewlett Packard Enterprise, 30 May 2022. [Online]. Available: <https://www.hpe.com/us/en/newsroom/press-release/2022/05/hewlett-packard-enterprise-ushers-in-new-era-with-worlds-first-and-fastest-exascale-supercomputer-frontier-for-the-us-department-of-energy-oak-ridge-national-laboratory.html>. [Accessed 29 September 2024].
- [7] H. Vora, P. Kathiria, S. Agrawal and U. Patel, "Neuromorphic computing: review of architecture, issues, applications and research opportunities," *Recent Innovations in Computing: Proceedings of ICRIC 2021*, vol. 2, pp. 371-383, Apr. 2022.
- [8] I. Chiaradia and M. A. Lancaster, "Brain organoids for the study of human neurobiology at the interface of in vitro and in vivo," *Nature Neuroscience*, vol. 23, no. 12, pp. 1496-1508, Dec. 2020.
- [9] S. Velasco et al., "Individual brain organoids reproducibly form cell diversity of the human cerebral cortex," *Natur*, vol. 570, no. 7762, pp. 523-527, Jun. 2019.
- [10] J. Zhao, "APOE4 exacerbates synapse loss and neurodegeneration in Alzheimer's disease patient iPSC-derived cerebral organoids," *Nature communications*, vol. 11, no. 1, p. 5540, Nov. 2020.
- [11] Park, J. C. et al., "A logical network-based drug-screening platform for Alzheimer's disease representing pathological features of human brain organoids," *Nature Communications*, vol. 12, no. 1, p. 280, Jan. 2021.

- [12] W. Gerstner, "2.2 Hodgkin-Huxley model," *Neuronal Dynamics* online book, [Online]. Available: <https://neuronaldynamics.epfl.ch/online/Ch2.S2.html>.
- [13] K. Yamazaki, V.-K. Vo-Ho, D. Bulsara and N. Le, "Spiking neural networks and their applications: A Review," *Brain Sciences*, vol. 12, no. 7, p. 863, Jun. 2022.
- [14] "The history of Spiking Neural Network," Spectra, [Online]. Available: <https://spectra.mathpix.com/article/2022.09.00085/the-history-of-spiking-neural-network>. [Accessed 2025].
- [15] J. Wang, "A review of spiking neural networks," *SHS Web of Conferences*, vol. 144, p. 03004, 2022.
- [16] T. Sharf et al., "Functional neuronal circuitry and oscillatory dynamics in human brain organoids," *Nature communications*, vol. 13, no. 1, p. 4403, Jul. 2022.
- [17] F. M. Benes and S. Berretta, "GABAergic interneurons: implications for understanding schizophrenia and bipolar disorder," *Neuropsychopharmacology*, vol. 25, no. 1, pp. 1-27, Jul 2001.
- [18] R. P. S. S. B. G. & P. J. C. Kang, "Electrophysiological insights with brain organoid models: a brief review," *BMB reports*, vol. 57, no. 7, p. 311, Jul 2024.
- [19] F. Puppo and A. R. Muotri, "Network and microcircuitry development in human brain organoids," *Biological Psychiatry*, vol. 93, no. 7, p. 590–593, Apr 2023.
- [20] C. A. Trujillo et al., "Complex oscillatory waves emerging from cortical organoids model early human brain network development," *Cell stem cell*, vol. 25, no. 4, pp. 558-569, Oct. 2019.
- [21] A. P. Passaro and S. L. Stice, " Electrophysiological analysis of brain organoids: current approaches and advancements," *Frontiers in Neuroscience*, vol. 14, p. 622137, Jan. 2021.
- [22] van der Molen et al., "Protosequences in human cortical organoids model intrinsic states in the developing cortex," *bioRxiv*, Dec. 2023.
- [23] Q. Huang et al., "Shell microelectrode arrays (MEAs) for brain organoids," *Science advances*, vol. 8, no. 33, Aug. 2022.
- [24] K. Tasnim and J. Liu, "Emerging bioelectronics for brain organoid electrophysiology," *Journal of molecular biology*, vol. 434, no. 3, p. 167165, Feb. 2022.
- [25] M. A. F. A. M. & H. O. Hassan, "Approximate Computing-Based Processing of MEA Signals on FPGA," *Electronics*, vol. 12, no. 4, p. 848, Feb. 2023.

- [26] L. D. Garma, L. Matino, G. Melle, F. Moia, F. De Angelis, F. Santoro and M. Dipalo, "Cost-effective and multifunctional acquisition system for in vitro electrophysiological investigations with multi-electrode arrays," *PloS One*, vol. 14, no. 3, Mar. 2019.
- [27] T. L. Li et al., "Stretchable mesh microelectronics for the biointegration and stimulation of human neural organoids," *Biomaterials*, vol. 290, p. 121825, Nov. 2022.
- [28] "ADS1294, ADS1294R, ADS1296, ADS1296R, ADS1298, ADS1298R," Texas Instruments, August 2015. [Online]. Available: <https://www.ti.com/lit/ds/symlink/ads1296r.pdf>. [Accessed 29 Sep. 2024].
- [29] "BlueNRG-LP," STMicroelectronics, March 2023. [Online]. Available: <https://www.st.com/resource/en/datasheet/bluenrg-lp.pdf>. [Accessed 29 September 2024].
- [30] G. P. Seu, G. N. Angotzi, F. Boi, L. Raffo, L. Berdondini and P. Meloni, "Exploiting all programmable SoCs in neural signal analysis: A closed-loop control for large-scale CMOS multielectrode arrays," *IEEE Transactions on Biomedical Circuits and Systems*, vol. 12, no. 4, pp. 839-850, May. 2018.
- [31] M. R. Mukati, S. Kocatürk, M. Kocatürk and T. Baykaş, "A microcontroller-based wireless multichannel neural data transmission system," *In 2017 21st National Biomedical Engineering Meeting (BIYOMUT)*, pp. i-iv, Nov. 2017.
- [32] A. Erofeev et al., "An Open-Source Wireless Electrophysiology System for In Vivo Neuronal Activity Recording in the Rodent Brain: 2.0.," *Sensors*, vol. 23, no. 24, p. 9735, Dec. 2023.
- [33] A. M. Shultz et al., "Robot-embodied neuronal networks as an interactive model of learning.," *The Open Neurology Journal* 11, p. 39, Sep 2017.
- [34] L. Smirnova and T. Hartung, "The promise and potential of brain organoids," *Advanced Healthcare Materials*, vol. 13, no. 21, Mar 2024.
- [35] L. Smirnova et al, "Organoid intelligence (OI): the new frontier in biocomputing and intelligence-in-a-dish," *Frontiers in Science*, vol. 1, p. 1017235, Feb. 2023.
- [36] J. S. Fleck et al., "Inferring and perturbing cell fate regulomes in human brain organoids.," *Nature*, vol. 621, no. 7978, pp. 365-372, Sep 2023.
- [37] N. Qiao et al., "A reconfigurable on-line learning spiking neuromorphic processor comprising 256 neurons and 128K synapses.," *Frontiers in neuroscience*, p. 141, Apr. 2015.
- [38] H. Cai et al., "Brain organoid reservoir computing for artificial intelligence," *Nature Electronics*, vol. 6, no. 12, pp. 1032-1039, Dec. 2023.

- [39] N. Rathi, I. Chakraborty, A. Kosta, A. Sengupta, A. Ankit, P. Panda and K. Roy, "Exploring neuromorphic computing based on spiking neural networks: Algorithms to hardware," *ACM Computing Surveys*, vol. 55, no. 12, pp. 1-49, Mar. 2023.
- [40] A. Javanshir, T. T. Nguyen, M. P. Mahmud and A. Z. Kouzani, "Advancements in algorithms and neuromorphic hardware for spiking neural networks," *Neural Computation*, vol. 34, no. 6, pp. 1289-1328, May. 2022.
- [41] M. Rizk and P. D. Wolf, "Optimizing the automatic selection of spike detection thresholds using a multiple of the noise level," *Medical & biological engineering & computing*, vol. 47, pp. 955-966, Sep 2009.
- [42] R. Q. Quiroga, Z. Nadasdy and Y. Ben-Shaul, "Unsupervised spike detection and sorting with wavelets and superparamagnetic clustering," *Neural computation*, vol. 16, no. 8, pp. 1661-1687, Aug 2004.
- [43] Z. Nenadic and B. J. W, "Spike detection using the continuous wavelet transform," *IEEE transactions on Biomedical Engineering*, vol. 52, no. 1, pp. 74-87, Dec 2004.
- [44] C. Gold, D. A. Henze, C. Koch and G. Buzsáki, "On the origin of the extracellular action potential waveform: A modeling study," *Journal of Neurophysiology*, vol. 95, no. 5, pp. 3113-3128, MAY 2006.
- [45] T. P. H. Sit et al., "Mea-NAP: A flexible network analysis pipeline for neuronal 2D and 3D organoid Multielectrode Recordings," *Cell Reports Methods*, vol. 4, no. 11, p. 100901, Nov 2024.
- [46] M. Tambaro, M. Bisio, M. Maschietto, A. Leparulo and S. Vassanelli, "FPGA design integration of a 32-microelectrodes low-latency spike detector in a commercial system for intracortical recordings," *Digital*, vol. 1, no. 1, pp. 34-53, Jan. 2021.
- [47] F. Lieb, H.-G. Stark and C. Thielemann, "A stationary wavelet transform and a time-frequency based spike detection algorithm for extracellular recorded data," *Journal of Neural Engineering*, vol. 14, no. 3, p. 036013, Mar. 2017.
- [48] M. Salmasi, U. Büttner and S. Glasauer, "Fractal dimension analysis for spike detection in low SNR extracellular signals," *Journal of Neural Engineering*, vol. 13, no. 3, p. 036004, Apr. 2016.
- [49] R. B. Bod et al., "From end to end: Gaining, sorting, and employing high-density neural single unit recordings," *Frontiers in Neuroinformatics*, vol. 16, Jun. 2022.
- [50] C. Acha et al., "Neuromodulation in neural organoids with Shell Meas," *bioRxiv, preprint*, Feb. 2025.

- [51] P. Virtanen et al., "SciPy 1.0: Fundamental algorithms for scientific computing in python," *Nature Methods*, vol. 17, no. 3, p. 261–272, Feb. 2020.
- [52] J. Negri, V. Menon and T. L. Young-Pearse, "Assessment of spontaneous neuronal activity in vitro using multi-well multi-electrode arrays: implications for assay development," *ENeuro*, vol. 7, no. 1, Jan. 2020.
- [53] C. S. Cutts and S. J. Eglen, "Detecting pairwise correlations in spike trains: an objective comparison of methods and application to the study of retinal waves," *Journal of Neuroscience*, vol. 34, no. 43, pp. 14288-14303, Oct. 2014.
- [54] E. L. K. Huang and B. Sun, "Understanding a Measure for Synchrony: Spike Time Tiling Coefficient Method".
- [55] A. P. Buccino et al., "Spikeinterface, a unified framework for Spike sorting," *eLife*, vol. 9, Nov. 2020.
- [56] J. P. Newman et al., "Closed-loop, multichannel experimentation using the open-source NeuroRighter Electrophysiology Platform," *Frontiers in Neural Circuits*, vol. 6, 2013.
- [57] STEMCELL Technologies, [Online]. Available: <https://www.stemcell.com/products/healthy-control-human-ipsc-line-male-scti004-a.html>. [Accessed 28 Nov. 2024].
- [58] T. E. Ludwig, V. Bergendahl, M. E. Levenstein, J. Yu, M. D. Probasco and J. A. Thomson, "Ludwig, T. E., Bergendahl, V., Levenstein, M. E., Yu, J., Probasco, M. D., & Thomson, J. A. (2006). Feeder-independent culture of human embryonic stem cells. *Nature methods*, 3(8), 637-646.," *Nature methods*, vol. 3, no. 8, pp. 637-646, 2006.
- [59] STEMCELL Technologies, [Online]. Available: <https://www.stemcell.com/products/mtesr-plus.html>. [Accessed 28 Nov. 2024].
- [60] L. Gao et al., "Post-passage rock inhibition induces cytoskeletal aberrations and apoptosis in human embryonic stem cells," *Stem cell research* 41, vol. 41, p. 101641, Dec. 2019.
- [61] STEMCELL Technologies, [Online]. Available: <https://www.stemcell.com/products/y-27632.html>. [Accessed 28 Nov. 2024].
- [62] STEMCELL Technologies, [Online]. Available: <https://www.stemcell.com/products/dulbeccos-phosphate-buffered-saline-with-2-fetal-bovine-serum.html>. [Accessed 28 Nov. 2024].
- [63] STEMCELL Technologies, [Online]. Available: <https://www.stemcell.com/products/relesr.html>. [Accessed 28 Nov. 2024].

- [64] STEMCELL Technologies, [Online]. Available: <https://www.stemcell.com/products/dmem-f-12-with-15-mm-hepes.html>. [Accessed 28 Nov. 2024].
- [65] STEMCELL Technologies, [Online]. Available: <https://www.stemcell.com/products/cryostorcs10.html>. [Accessed 28 Nov. 2024].
- [66] M. A. Lancaster and J. A. Knoblich, "Generation of cerebral organoids from human pluripotent stem cells," *Nature protocols*, vol. 9, no. 10, pp. 2329-2340, Oct. 2014.
- [67] S. L. Giandomenico, M. Sutcliffe and M. A. Lancaster, "Generation and long-term culture of advanced cerebral organoids for studying later stages of neural development," *Nature protocols*, vol. 16, no. 2, pp. 579-602, Feb. 2021.
- [68] N. Hattori, "Cerebral organoids model human brain development and microcephaly," *Movement Disorders*, vol. 2, no. 29, p. 185, Feb. 2014.
- [69] STEMCELL Technologies, [Online]. Available: <https://www.stemcell.com/products/stemdiff-cerebral-organoid-kit.html>. [Accessed 28 Nov. 2024].
- [70] STEMCELL Technologies, [Online]. Available: <https://www.stemcell.com/products/aggrewell-rinsing-solution.html>. [Accessed 28 Nov. 2024].
- [71] STEMCELL Technologies, [Online]. Available: <https://www.stemcell.com/products/organoid-embedding-sheet.html>. [Accessed 28 Nov. 2024].
- [72] STEMCELL Technologies, [Online]. Available: <https://www.stemcell.com/products/ultra-low-adherent-plate-for-suspension-culture.html>. [Accessed 28 Nov. 2024].
- [73] "Stemcell Technologies," [Online]. Available: <https://www.stemcell.com/media/files/infographic/DI033PSCinfographicpassage.pdf>. [Accessed 28 Nov. 2024].
- [74] STEMCELL Technologies, [Online]. Available: <https://www.stemcell.com/products/gentle-cell-dissociation-reagent.html>. [Accessed 28 Nov. 2024].
- [75] "Corning® Matrigel® Hesc-qualified matrix, LDEV-free, 5 ML," Corning, [Online]. Available: <https://ecatalog.corning.com/life-sciences/b2c/US/en/Surfaces/Extracellular-Matrices-ECMs/Corning%C2%AE-Matrigel%C2%AE-Matrix/p/354277>. [Accessed 28 Nov. 2024].
- [76] A. P. Passaro and S. L. Stice, "Electrophysiological analysis of brain organoids: current approaches and advancements," *Frontiers in Neuroscience*, vol. 14, p. 622137, Jan. 2021.
- [77] S. Ballav, A. Ranjan, S. Sur and S. Basu, "Organoid Intelligence: Bridging Artificial Intelligence for Biological Computing and Neurological Insights.,," 2024.

- [78] A. Lavazza and M. Massimini, "Cerebral organoids: ethical issues and consciousness assessment," *Journal of Medical Ethics*, vol. 44, no. 9, pp. 606-610, Sep. 2018.
- [79] S. Y. A. Chow, H. Hu, T. Osaki, T. Levi and Y. Ikeuchi, "Advances in construction and modeling of functional neural circuits in vitro," *Neurochemical Research*, vol. 47, no. 9, pp. 2529-2544, Sep. 2022.
- [80] J. M. Walz, M. Pedersen, A. Omidvarnia, M. Semmelroch and G. D. Jackson, "Spatiotemporal mapping of epileptic spikes using simultaneous EEG-functional MRI," *Brain*, vol. 140, no. 4, pp. 998-1010, Apr. 2017.
- [81] J. Bian, Z. Cao and P. Zhou, "Neuromorphic computing: Devices, hardware, and system application facilitated by two-dimensional materials," *Applied Physics Reviews*, vol. 8, no. 4, Oct. 2021.
- [82] A. Lavazza and M. Massimini, "Cerebral organoids: ethical issues and consciousness assessment," *Journal of Medical Ethics*, vol. 44, no. 9, pp. 606-610, Sep. 2018.
- [83] S. Zhang, Z. Wan and R. D. Kamm, "Vascularized organoids on a chip: strategies for engineering organoids with functional vasculature," *Lab on a Chip*, vol. 21, no. 3, pp. 473-488, 2021.
- [84] STEMCELL Technologies, [Online]. Available: <https://www.stemcell.com/products/gentle-cell-dissociation-reagent.html>. [Accessed 28 Nov. 2024].
- [85] STEMCELL Technologies, [Online]. Available: <https://www.stemcell.com/products/healthy-control-human-ipsc-line-male-scti004-a.html>. [Accessed 28 Nov. 2024].
- [86] R. Kang, S. Park, S. Shin, G. Bak and J. C. P., "Electrophysiological insights with brain organoid models: a brief review," *BMB reports*, vol. 57, no. 7, p. 311, Jul 2024.